UNIVERSIDADE FEDERAL DE ITAJUBÁ

Pró-Reitoria de Pesquisa e Pós-Graduação – PRPPG

Programa de Doutorado Acadêmico em Engenharia Elétrica

Wireless Power Transfer System for Charging Lithium-Ion Batteries in Small Electric Vehicles

Aluno: Juan Pablo Ochoa-Avilés
Orientador: Prof. Dr. Ênio Roberto Ribeiro - UNIFEI
Coorientador: Prof. Dr. Fernando Lessa Tofoli - UFSJ

Área de Concentração: Automação e Sistemas Elétricos Industriais
Linha de Pesquisa: Controle e Automação de Processos

Itajubá, novembro de 2025

SUMMARY

LIST OF FIGURES

LIST OF TABLES

NOMENCLATURE

AC	ALTERNATING CURRENT.
ACM	ASYMMETRICAL CLAMPED-MODE.
ADALINE	ADAPTIVE LINEAR ELEMENT.
ADC	ANALOG TO DIGITAL CONVERTERS.
ASDC	ASYMMETRICAL DUTY-CYCLE.
ARX	AUTOREGRESSIVE LINEAR REGRESSION WITH AN AUTOREGRESSIVE EXOGENOUS INPUT.
CC	CONSTANT CURRENT.
CCS	CONSTANT CURRENT SOURCE.
CPS	CONSTANT POWER SOURCE.
CPT	CAPACITIVE POWER TRANSFER.
CRES	RESONANT CAPACITOR.
CSA	CHARGING STATION ASSEMBLIES.
CV	CONSTANT VOLTAGE.
CVS	CONSTANT VOLTAGE SOURCE.
CWPT	CAPACITIVE WIRELESS POWER TRANSFER.
DC	DIRECT CURRENT.
DCFC	DIRECT CURRENT FAST CHARGE.
DSP	DIGITAL SIGNAL PROCESSING.
EMI	ELECTROMAGNETIC INTERFERENCE.
EVS	ELECTRIC VEHICLES.
FBAR	FULL-BRIDGE ACTIVE RECTIFIER.
FFT	FAST FOURIER TRANSFORM.
GPIO	GENERAL-PURPOSE INPUT/OUTPUT.
ICEVS	INTERNAL COMBUSTION ENGINE VEHICLES.
IEC	INTERNATIONAL ELECTROTECHNICAL COMMISSION.
IEEE	INSTITUTE OF ELECTRICAL AND ELECTRONIC ENGINEERS.
IPT	INDUCTIVE POWER TRANSFER.
K	COUPLING COEFFICIENT.
LCC	INDUCTOR-CAPACITOR-CAPACITOR.
LLC-SP	INDUCTOR-INDUCTOR-CAPACITOR SERIES-PARALELL.
LPG	LIQUEFIED PETROLEUM GAS.
LRES	RESONANT INDUCTOR.
MCR-WPT	MAGNETIC COUPLING RESONANT WIRELESS POWER TRANSFER.
MOSFET	METAL-OXIDE-SEMICONDUCTOR FIELD-EFFECT TRANSISTOR.
MPPT	MAXIMUM POWER POINT TRACKING.
MRPT	MAGNETIC RESONANCE POWER TRANSFER.
MR-WPT	MAGNETIC RESONANT WIRELESS POWER TRANSFER.
MSE	MEAN SQUARE ERROR.
NGV	NATURAL GAS VEHICLE.
P&O	PERTURB AND OBSERVE.
PEVS	PLUG-IN ELECTRIC VEHICLES.
PFC	POWER FACTOR CORRECTION.
PFM	PULSE FREQUENCY MODULATION.
PGND	POWER GROUND.
PHCT	PRIMARY HIGH-ORDER COMPENSATOR TOPOLOGIES.
PI	PROPORTIONAL-INTEGRAL.
PMPT	PERMANENT MAGNETIC POWER TRANSFER.
PTE	POWER TRANSMISSION EFFICIENCY.
PWM	PULSE WIDTH MODULATION.
Q	QUALITY FACTOR.
RFID	RADIO-FREQUENCY IDENTIFICATION.
RIPT	RESONANT INDUCTIVE POWER TRANSFER.
RL	LOAD RESISTOR.
RMS	ROOT MEAN SQUARE.
RX	RECEIVER COIL.
SAE	SOCIETY OF AUTOMOTIVE ENGINEERS.
SEPIC	SINGLE-ENDED PRIMARY INDUCTANCE CONVERTER.
SPWM	SINUSOIDAL PULSE WIDTH MODULATION.
THD	TOTAL HARMONIC DISTORTION.
TPS	TRADITIONAL PHASE-SHIFT MODULATION.
TX	PRIMARY WINDING.
UTET	ULTRASONIC TRANSCUTANEOUS ENERGY TRANSFER.
VA	VEHICLE ASSEMBLIES.
WPT	WIRELESS POWER TRANSFER.
ZCS	ZERO-CURRENT SWITCHING.
ZVDS	ZERO-DERIVATIVE-VOLTAGE SWITCHING.
ZVS	ZERO VOLTAGE SWITCHING.

ABSTRACT

Wireless Power Transfer has emerged as a promising solution for contactless battery charging in small electric vehicles, offering enhanced safety, convenience, and system reliability. This work presents the design, modeling, control, and experimental validation of a magnetic resonant wireless power transfer system based on a high-frequency Class-DE resonant inverter for charging lithium-ion batteries. A comprehensive theoretical analysis is carried out considering series, parallel, and series-parallel resonant compensation topologies, enabling efficient energy transfer under varying coupling conditions caused by coil misalignment and distance variation. A novel digital control strategy based on an ADALINE neural network combined with an autoregressive exogenous (ARX) model is proposed to regulate the inverter switching instants and maintain stable output voltage despite load and coupling fluctuations. The control approach is derived from a frequency-domain band-pass filter model of the resonant tank and implemented using a digital signal processing platform. The proposed controller demonstrates fast dynamic response, reduced harmonic distortion, and improved robustness compared to conventional open-loop operation. A laboratory-scale prototype operating in the MHz range is developed to validate the proposed methodology. Experimental results confirm soft-switching operation with zero-voltage and zero-current switching, reduced thermal stress on GaN MOSFETs, and enhanced power transmission efficiency across different coil separations. System performance is evaluated in both time and frequency domains, including harmonic analysis and thermal characterization. The results demonstrate that the proposed Class-DE-based MR-WPT system with ADALINE-based ARX control is a viable and efficient solution for wireless charging applications in light electric mobility systems.

Keywords: ADALINE Neural Network, ARX Model, Class-DE Resonant Inverter, Digital Control, High-Frequency Power Electronics, Magnetic Resonant Wireless Power Transfer, Soft Switching, Wireless Charging of Lithium-Ion Batteries, Wireless Power Transfer

RESUMO

A transferência de energia sem fio WPT surgiu como uma solução promissora para o carregamento de baterias sem contato em veículos elétricos de pequeno porte, oferecendo maior segurança, conveniência e confiabilidade do sistema. Este trabalho apresenta o projeto, a modelagem, o controle e a validação experimental de um sistema de transferência de energia sem fio por ressonância magnética, baseado em um inversor ressonante Classe DE de alta frequência para o carregamento de baterias de íons de lítio. Uma análise teórica abrangente é realizada considerando topologias de compensação ressonante em série, paralela e série-paralela, permitindo uma transferência eficiente de energia sob condições variáveis de acoplamento, decorrentes de desalinhamento das bobinas e variações de distância. Propõe-se uma estratégia inovadora de controle digital baseada em uma rede neural ADALINE, combinada a um modelo autorregressivo com entrada exógena (ARX), com o objetivo de regular os instantes de comutação do inversor e manter a tensão de saída estável, apesar das flutuações de carga e de acoplamento. A abordagem de controle é derivada de um modelo de filtro passa-banda no domínio da frequência do tanque ressonante e implementada utilizando uma plataforma de processamento digital de sinais. O controlador proposto apresenta resposta dinâmica rápida, redução da distorção harmônica e maior robustez em comparação à operação convencional em malha aberta. Um protótipo em escala de laboratório, operando na faixa de MHz, é desenvolvido para validar a metodologia proposta. Os resultados experimentais confirmam a operação com comutação suave, (ZVS) e (ZCS), redução do estresse térmico nos MOSFETs de GaN e melhoria da eficiência de transmissão de potência para diferentes separações entre as bobinas. O desempenho do sistema é avaliado nos domínios do tempo e da frequência, incluindo a análise harmônica e a caracterização térmica. Os resultados demonstram que o sistema MR-WPT baseado no inversor Classe DE controlado pela estrutura ARX baseada na rede neural ADALINE constitui uma solução viável e eficiente para aplicações de carregamento sem fio em sistemas de mobilidade elétrica leve.

Palavras-chave: Carregamento sem fio de baterias de íons de lítio, Comutação suave, Controle digital, Eletrônica de potência em alta frequência, Inversor Ressonante Classe DE, Modelo ARX, Rede neural ADALINE, Transferência de Energia por Ressonância Magnética, Transferência de Energia Sem Fio

CHAPTER I

INTRODUCTION

1.1 Justification

The market for electric vehicles (EVs) has witnessed remarkable growth in recent years, making it an attractive prospect for automotive manufacturers. The need to reduce fossil fuel consumption and greenhouse gas emissions has heightened the demand for EVs [1]. Another essential issue is urban mobility, which motivated the development of small-sized vehicles such as scooters and electric bikes [2]. The gradual replacement of traditional internal combustion engine vehicles (ICEVs) with their electric counterparts will be influenced by various factors, including significant decreases in manufacturing costs, advances in battery energy storage technology, and the introduction of government policies, among others [3].

The great advantage that guarantees a promising future for EV technology is the high efficiency and low energy consumption compared to internal combustion vehicles, as shown in Figure 1.1. The savings in cost per kilometer offered by different vehicles powered with gasoline, ethanol (E85), hybrid, diesel oil, biodiesel, liquefied petroleum gas (LPG), natural gas vehicle (NGV) and electricity are 0%, 1%, 20%, 23% 27%, 33%, 38% and 75%, respectively.

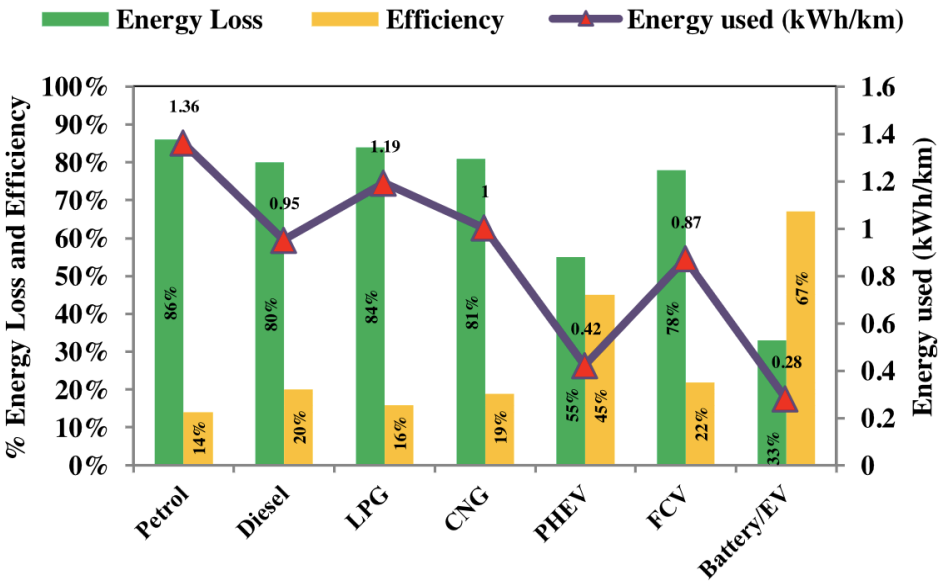

Figure 1.1: Comparative analysis of different kinds of fuels.
Source: [4].

Various factors impact the EV market, including how consumers perceive the return on investment, advancements in technology, urban planning, and access to EV charging infrastructure. To achieve sustainable and balanced growth in charging availability, it is important to consider variables like the location of charging points, energy availability at different times, and the types of EVs that can be connected, all in line with society's consumption patterns; these

are significant factors when considering that nowadays, there are around 9.5 million charging stations worldwide, with seven million in residential areas [5]. Recent analyses indicate that public charging stations are being used just as frequently as private ones, which means that people who don't have access to home charging stations can still charge their Evs [6].

In this sense, four charging modes are established by international standards, how "International Electrotechnical Commission" norm IEC 61851-1:2017 [7], which differ based on how quickly batteries reach their maximum energy storage capacity. These modes are characterized by voltage, current, and power levels: Mode 1 and 2 use alternating current (AC) and operate at low power levels. Mode 3 also uses AC, but at high power, while mode 4 uses direct current (DC) for fast charging. For modes 1-3, the EV needs an onboard converter, while mode 4 requires only an external converter. However, each charging mode needs a specific connection socket depending on the voltage it handles [8].

While battery systems are moving toward higher voltage and lower current, it is crucial to consider the isolation levels when selecting the converter topology. Regarding the commercial voltage levels in EVs, smaller and medium-sized vehicles usually operate within the 400 V range. In contrast, heavy-duty vehicles generally have an operating voltage of approximately 800 V. According to [9], plug-in electric vehicles (PEVs) are an essential part of the future smart cities and play a significant role in achieving sustainable energy goals. The implementation of EV charging stations at a large scale is equally crucial. In both cases, extensive research has been conducted on fast onboard and offboard chargers that depend on power electronic converters[10]. Offboard chargers allow multiple EVs to connect simultaneously to the three-phase grid at charging stations [11]. Therefore, it is vital to minimize charging time while ensuring user safety and preserving battery lifetime [12]. As EVs and hybrid vehicles become more prevalent, the role of charging systems becomes increasingly critical in their operation. Compared to traditional gasoline vehicles, EVs require more time for recharging and have fewer dedicated charging points and stations available. Fast charging equipment can provide up to 50% battery capacity in just three minutes and over 80% in 15 minutes, but this technique can result in quicker battery deterioration. To optimize battery lifespan, a control algorithm that utilizes microcontrollers and digital signal processors to regulate the current/voltage combination may be necessary [13]. The charging levels have been categorized by the Electrical Power Research Institute (EPRI) and the Society of Automotive Engineers (SAE) [12] into AC Level 1, AC Level 2, and Direct Current Fast Charge (DCFC). AC Level 1 is the slowest, requiring 8 to 16 hours to reach maximum battery charge with a current rate of no more than 20 A; domestic charging can require a power consumption of 1.4-1.9 kW. AC Level 2 takes between 4 and 8 hours to charge the battery and has a capacity of over 80A; this charging consumes a power of 7.7-25.6 kW. Lastly, Level 3 refers

to fast charging systems that take only 10 to 15 minutes to reach the desired charge and require higher voltage levels exceeding 480V and three phases with 400A and more than 50 kW.

When selecting the topology of the charging system for EVs, there are currently two options to consider. The first involves charging through wires, which necessitates a physical link between the charging station and the automobile. The second option consists of charging without any physical connection between the energy source and the load, otherwise known as wireless power transfer (WPT), as shown in Figure 1.2. The device includes a transmitter stage that produces a high-frequency signal, generating a variable electromagnetic field. This field induces a current in the receiver's resonator circuit, which, after being rectified, charges the energy accumulator elements. The WPT method is still maturing, but it could supplant plug-in stations in a short time.

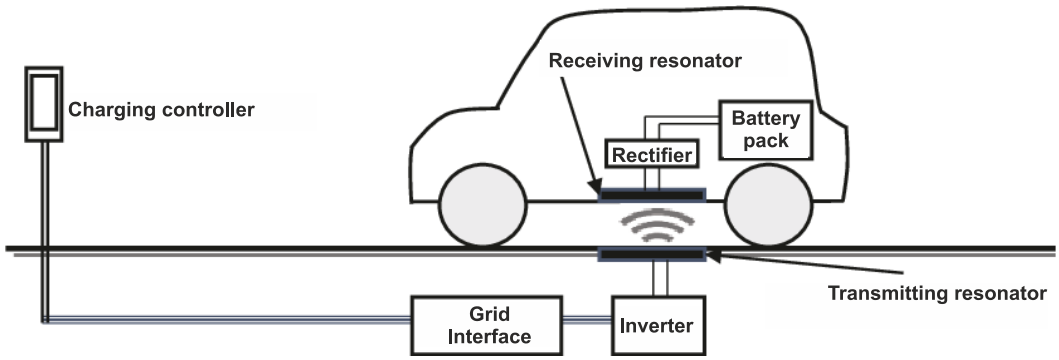

Figure 1.2: Stationary WPT for EVs Charging.
Source: [14]

When connecting an EV to a charging station, it is essential to consider how it may impact the public power grid. To minimize disruptions and maintain optimal charging efficiency, numerous studies have been conducted, Figure 1.3 illustrates this charging process, which involves an AC-DC rectifier with power factor correction (PFC) in the offboard grid interface

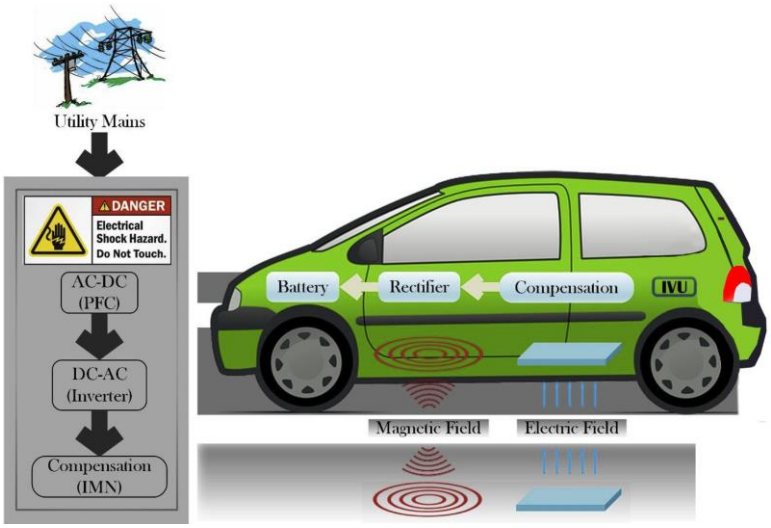

Figure 1.3: Structure diagram for a typical WPT EVs charging system.
Source: [16]

. This converts the commercial voltage into a regulated DC signal. An inverter circuit then converts the DC signal back to a high-frequency AC wave, and a galvanic coupling provides optimal isolation between the AC source and DC load by the magnetic field interface [15].

Although WPT offers convenience, segmentation, flexibility, and security, it involves a significant number of switched elements due to the need for inverter topologies. Therefore, it is essential to carefully study the type of inverter used, as well as its control method, to optimize the performance of the WPT system and further advance this technique's maturation.

Resonant inverters play a crucial role in regulating voltage and frequency levels on the WPT transmitter side, thereby reducing switching losses and optimizing energy transfer. Class E, class E_2, class D, class EF, class EF_2, and class DE are commonly used topologies [17]. However, these topologies must be carefully selected based on the application and power levels, given the high operating frequency, which demands advanced switch construction technology. To make an appropriate choice, it is essential to analyze the advantages and disadvantages of each topology, considering factors such as their current and voltage switch stress, since each topology responds differently to the same power output.

When designing a controller for a resonant inverter, one must consider factors such as mutual inductance, coupling coefficient, eddy currents, and hysteresis. These concerns require significant mathematical development for traditional control models. However, alternative digital control methods, such as fuzzy logic or artificial intelligence, have gained popularity in the literature, as they can achieve optimal operation of resonant inverters while overcoming the complexities outlined above.

1.2 Objectives

Building upon the above information, this work comprehensively analyzes the various inverter topologies used on the offboard side of the WPT for EV charging. It will include a thorough review of the technology, controller models, and implications of electromagnetic emissions on human health.

A comprehensive review of the literature reveals that a factor yet to be explored in WPT systems is the relationship between the difference in the impedance of the magnetic circuit related to the separation of the coils, when this variation is considered from the perspective of a half-bridge class DE resonant inverter, it can serve as a control signal for decision-making regarding the duty cycle of the controlled switching elements. This approach aims to enhance the system's efficiency and streamline the hardware involved in the prototype manufacturing process.

The proposed work involves the development of a mathematical model to estimate the controller that ensures stability in the output voltage of a Class DE resonant inverter used in a

WPT system. The model is based on an Adaptive Linear Element (ADALINE) neural network, which establishes an Autoregressive linear regression with an exogenous input identification procedure (ARX). This enables the implementation of a transfer function in discrete time, which can be realized directly through digital signal processing (DSP) techniques.

Using this control proposal, the system can operate without any issues, even in the presence of disturbances that may occur in the magnetic circuit due to the misalignment between the transmitter and the receiver, without requiring an additional communication channel between them. Such disturbances can directly affect the mutual inductance and load resistance and, consequently, the system's efficiency. This is a significant contribution as it eliminates the need to establish a control loop across compensation topologies for tuning the circuit. Instead, a data matrix for the duty cycle as a function of the load resistance is obtained and used for training the ADALINE neural network. This approach simplifies the work for the designers.

The primary objectives of this work are to:

- Develop a mathematical model for the class DE inverter and control strategy using an ARX parameter identification system based on an ADALINE neural network.
- Verify the accuracy of the obtained equations through frequency sweep simulations in electrical circuit simulation software.
- Conduct simulations to compare the proposed control strategy with three different topologies from inverters, i.e., series, parallel, and series-parallel resonant tanks.
- Examine the controller's response to variations in the DC source voltage and load resistance due to misalignments between the resonant transmitter and receiver.

1.3 Organization of topics

Chapter 2 provides a concise bibliographic review of WPT technology. It discusses the topologies of resonant inverters commonly used in WPT systems. The chapter also analyzes various control strategies applied to these systems, considering the efficiency achieved in each case. This review aims to comprehensively understand the latest developments in WPT technology for EV charging and highlight the importance of efficient control strategies in this field.

In Chapter 3, a mathematical description is provided for this work. By deriving the characteristic equation for each topology under analysis, an appropriate control strategy is established using the ARX-based Adaline network. Additionally, a study of behavior in terms of resonance frequency and switching frequency is conducted for each resonant circuit together with the class DE resonant inverter. This analysis establishes the premises for adopting a successful operating point for each case. In addition, the text discusses the comparison between various control strategies, where a brief analysis is presented based on their complexity for

implementation, as well as the advantages and disadvantages associated with each control methodology. This comparison has been derived from the existing literature on the subject, highlighting the different approaches researchers take in the field. By analyzing the effectiveness and feasibility of each methodology, the text aims to provide a comprehensive understanding of the various control strategies and their practical implementation in real-world scenarios.

Chapter 4 delves into the computer simulation results conducted on the PSIM® software. This simulation validates the expressions for the transfer functions of the class DE inverter, thereby confirming the efficiency of the three types of resonant load adopted. In addition, the study also establishes the behavior of the voltage at the load by applying variations to the ohmic value of the load resistance. This helps to gauge the performance of the ADALINE-based ARX controller system under different conditions, thereby providing a better understanding of its operational capabilities. Moreover, the study also defines the operating range of the load resistance for each of the topologies. This provides insights into the optimal parameters that need to be maintained for the system to function at its best, thereby ensuring that the desired outcomes are achieved efficiently.

Chapter 5 begins by outlining the physical design of the developed prototype, taking into account the recommendations for construction from the manufacturers of the selected switching and control components, as well as design guidelines for electronic board production. Subsequently, the chapter provides a detailed overview of the work conducted on the WPT system, examining its performance at three randomly chosen operating points based on the separation between the transmission and reception coils. This examination validates several aspects, including the system's efficiency, controller operation, harmonic content of the resonant circuit waves, and thermal effects on the switches, all of which are related to the correlation between the primary load impedance and the MOSFET duty cycle.

1.4 Publications

The research presented in this work was published in the international peer-reviewed journal *Energies* (MDPI). The paper proposes a novel control approach for resonant Class-DE inverters applied to wireless power transfer (WPT) systems, addressing one of the main challenges of such systems: maintaining efficient and stable operation under coil misalignment and varying coupling conditions. The proposed method combines an adaptive linear neuron (ADALINE) network with an autoregressive model with exogenous input (ARX) to accurately determine the switching instants of the power devices. This adaptive strategy enables the inverter to preserve soft-switching operation and regulated output voltage despite changes in alignment. Experimental results demonstrate that the proposed controller outperforms conventional linear

control techniques, providing improved robustness, efficiency, and dynamic response, which are essential for practical WPT applications such as electric vehicle charging.

CHAPTER II

LITERATURE REVIEW

2.1 Preliminary considerations

This chapter aims to provide a comprehensive literature review on the latest trends in WPT technology for charging EV batteries. This review will delve into the most significant technologies available, including Inductive Power Transfer (IPT), Magnetic Resonance Power Transfer (MRPT), Capacitive Power Transfer (CPT), and others. Furthermore, various aspects related to the types of inverters used in MRPT will be examined, such as their implementation complexity and energy transfer efficiency. Lastly, a study will be conducted on the various control techniques applied to the resonant inverters under analysis.

2.2 Overview of WPT Technology

According to [16], depending on the type of converter used and its transmission mode, WPT technology can be classified in various ways. The potential applications of this technology are vast, ranging from remote monitoring and magnetic field communication systems to radio-frequency identification (RFID) and aerospace systems, among others. However, one of the most exciting prospects is the development of wireless charging systems for EVs. The possibility of charging batteries without physical connections or cabling could revolutionize the industry [18]. The IPT, Resonant Inductive Power Transfer (RIPT), Permanent Magnetic Power Transfer (PMPT), and Capacitive Wireless Power Transfer (CWPT) methods can be achieved within a limited distance; on the other hand, the Optical Wireless Power Transfer (OWPT), Magnetic Resonant Power Transfer (MR-WPT), and Ultrasonic Transcutaneous Energy Transfer (UTET) technologies enable longer transmission distances since their wavelengths are longer than the transmission length; this characteristic allows for enhanced transmission efficiency and reduced signal loss over far away. One can classify WPT systems into two major groups: near-field (non-radioactive) systems and far-field (radioactive) systems [19]. The first type comprises all IPT technologies and CWPT approaches. CWPT relies on contactless power transfer via electric-field coupling between two pairs of metal capacitive plates. Still, most modern CWPT systems are used in low-power applications, where the transmission distance is only a few millimeters [20]. In turn, IPT systems can achieve high power transmission efficiency (PTE) at transmission distances on the order of centimeters. The systems need ferrite cores to guide the electromagnetic flux, which makes it suitable for not resonant low-frequency operation , and the transmitter and receiver are separated by air, being a safe and low-cost system; however, the primary and secondary coils must be perfectly aligned, and the efficiency is achieved only for short distances [21]. Table 2.1 provides a comprehensive overview of the WPT methods and their details.

Table 2.1: Comparison among the different types of WPT [16].

Methods	Efficiency	Merits	Demerits
IPT [22-24]	99.5% 6.6 kW, 0.5 mm	Extremely high efficiency	Limited achievable power transfer distance
RIPT [25-27]	94% 11 kW, 10–15 cm	Good balance between power transfer distance and efficiency	Parameter-sensitive (e.g., mutual inductance, load impedance)
PMPT [28, 29]	81% 1.6 kW, 15 cm	Low EMF exposure and temperature rise of the foreign object	noise, vibration, harshness problems
CWPT [30, 31]	84% 30 W, 5 mm	No core losses, more straightforward and more compact design	Higher exciting voltage for the same power class
OWPT [32, 33]	84% 30 kW, 1 mile	Free of flux guidance and no comparable energy density	Hazardous and easily affected by weather conditions
MR-WPT [34-36]	59.2% @10 kW, 1.2 m 5.01% @250 mW, 1 m	No rigid alignment is required, with potential in both near-field and far-field applications. applications	Poor efficiency and inevitable field exposure
UTET [37]	39% 30 mm, 360 mW	Non-radiative and suitable for multiple pickups	Inefficient and costly

Research has revealed that some factors must be carefully considered when ensuring the safety of users and the system. For instance, the presence of foreign metallic elements near the magnetic circuit of the WPT, specifically in the primary winding (T_x), can significantly impact the distribution of electromagnetic field lines between the transmitter and receiver. This can ultimately impair crucial characteristics of the WPT system, including performance efficiency, quality factor (Q), and mutual inductance (M), among others, due to the interference introduced. In a study carried out by [38], three methods for detecting metallic objects in the WPT system were analyzed. The first approach, "Sensor-based," utilizes temperature, pressure, image, and radar sensors. While susceptible and independent of power levels, oscillation frequency, and system misalignment, this method does have some drawbacks, including a high cost, difficulty detecting non-metallic materials, susceptibility to environmental variations, and requiring a large implementation area. The second approach, namely “parameter-variation”, involves analyzing system parameter changes when making decisions; the factor of mutual inductance between the transmitter and receiver coil is crucial to power transmission efficiency to the load. If there is misalignment of the magnetic circuit, it can reduce the mutual inductance, leading to a degradation of the system's efficiency. Finally, the "sensing pattern-based" strategy relies on inducing a voltage in the receiver winding and measuring its inductance variation. This approach offers high sensitivity immunity to misalignment, environmental factors, and non-metallic materials. However, it does require careful design of the detection coil to ensure no power loss to the load.

The influence of the quality factor is examined in [39], which presents a novel inductor design aimed at achieving a high Q value that remains independent of the size of each litz wire and the depth of its skin effect. This innovative topology consists of multiple conductor layers and dielectric layers, with each conductor layer shaped like a "C" and each dielectric layer having a toroidal shape. A single dielectric layer separates two conductor layers. The system achieves its highest efficiency of 75% when the primary and secondary coils are in direct contact. However,

the maximum separation between these coils can be up to 8 cm, resulting in a power transfer efficiency of 2%. Additionally, the IPT system can enter standby mode to conserve energy consumption. This option has the advantage of being low cost and quick to detect but is limited to low powers and susceptible to misalignment.

The authors in [40] offer an analysis approach that focuses on the safety of vehicle users when charged by the WPT system. The findings indicate that by implementing sufficient shielding, the electromagnetic field emissions within the vehicle never rise above 7.5 μT. This value is 28 times below the maximum limit of 207 μT recommended by Institute of Electrical and Electronics Engineers (IEEE) standards for exposure to electromagnetic fields [41], ensuring a safe experience for passengers.

The study outlined in [42] examined the temperature of the WPT system and found that the coil, ferrite core, and protective shield were the primary sources of heat in the WPT system transmitter; for a thickness ferrite of 5 mm, the inductor reached a maximum temperature of 65° C in both simulations and experiments. However, the ferrite can quickly get 150°C at this thickness, and the metal parts of the block's external structure reached 57° C. The experiment also revealed that the metal parts around 2 to 3 inches of the coil came with dangerous thermal values, indicating the need for shielding with low-permeability and high-conductivity materials.

To ensure the utmost safety, it is recommended that EV users opt for isolated load topologies when the power supply input voltage exceeds 60 VDC. These topologies fall under the WPT category and can be soft or hard-switching. Of the two, the soft-switching topology is ideal, as it is optimized for high frequencies, resulting in minimized switching losses and increased operational efficiency. Whereas, IPT systems demonstrate superior transmission efficiency and a more excellent range than near-field WPT systems. Based on these criteria, Figure 2.1 depicts a standard IPT system designed for EV charging applications. It comprises four conversion stages that work together seamlessly. The first stage, a rectifier, corrects the input power factor (PFC) and generates a regulated DC output voltage with minimal low-frequency ripple. A high-frequency inverter then generates a high-frequency sine wave, and the power is transmitted through a conductive medium with a defined magnetic permeability, such as air, via magnetic coupling. A second rectifier is needed to charge the battery bank to obtain a DC voltage that supplies a DC-DC converter. IPT technology holds great promise and requires careful attention to coil structure development, energy management strategies, and converter topologies, among other factors [43].

Additionally, Figure 2.1 presents an innovative IPT technology called magnetic coupling resonant wireless power transfer (MCR-WPT). In this scenario, the voltage and current waveforms on both the primary and secondary sides are synchronized, and the circuit functions

as a purely resistive load. This magnetic coupling attribute has enhanced performance, such as increased efficiency and longer transmission ranges. Nonetheless, certain variables can impact the efficiency of WPT systems, such as misalignment in the magnetic coupling circuit along the x-axis, the y-axis, or both.

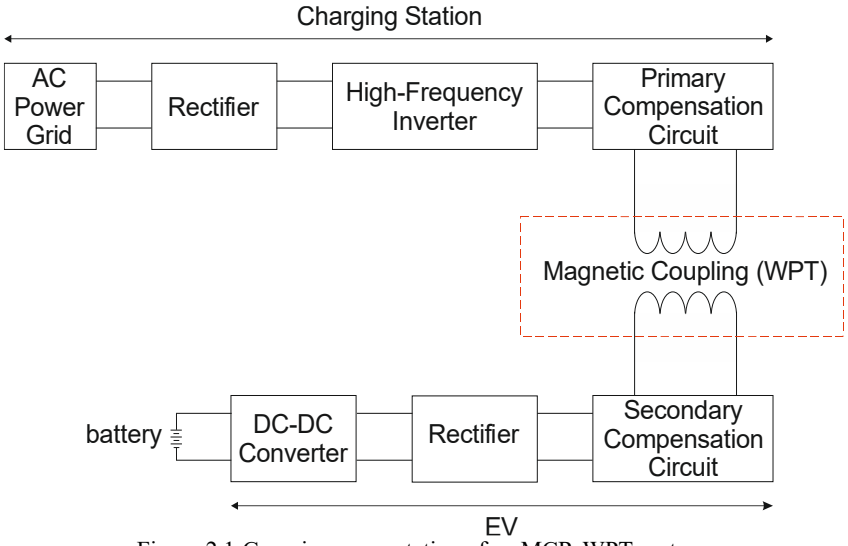

Figure 2.1:Generic representation of an MCR-WPT system.

Compensation circuits play a crucial role in neutralizing the leakage inductance of magnetically coupled systems, thereby prolonging battery life and ensuring optimal output waveform levels [44]. IPT battery charging systems are designed with a constant current (CC) or constant voltage (CV) profile, eliminating the need for wireless communication and detection circuits. This inherent characteristic of IPT systems provides the benefits of simplicity and reliability, making it an efficient solution for EVs battery charging applications.

The development of WPT systems is still hindered by some factors that impede their widespread adoption for EV battery charging [45], such as the low energy transfer rate compared to conventional charging technologies. Additionally, safety concerns regarding electromagnetic radiation continue to be debated. A contactless energy transfer system consists of an emitter on the ground and a receiver inside the EV. Thus, users' exposure to the magnetic field is inherent in the system's operation. In addition to being efficient, this arrangement ensures proper values of the mutual inductance and coupling factor, as previously analyzed. However, they must comply with public health regulations for the maximum levels of non-ionizing radiation tolerated by humans. In this sense, the International Commission for Non-Ionizing Radiation Protection (ICNIRP) established the limits of 27 μT for the magnetic induction and 4.05 V/m for the electric field, which seem to be the most appropriate specifications for MCR-WPT applications involving EVs.

WPT systems face a significant challenge due to high-temperature levels, which limit their development; choosing appropriate materials for the construction of coils is a difficult task. A research work described in [46] considers several factors that cause losses in the system and result

in the heating of both the emitter and the receiver. By developing a mathematical model that represents the heat transfer for the magnetic circuit, the researchers propose an optimization method using a genetic algorithm that establishes ideal parameters for manufacturing primary and secondary coils. They tested this model with a prototype, which achieved an efficiency of 93.6% with a chassis temperature of 48.6°C. This study shows that it is possible to predict the steady-state temperature for the magnetic coupling circuit in a WPT system through this algorithm; it can facilitate the design of more stable and efficient WPT systems.

A challenge in the WPT system for EVs charging at present is that implementing large-scale charging stations requires substantial investment in road modifications, parking lots, parking spaces, and associated maintenance costs. The SAE has introduced the first worldwide standard for WPT systems to promote the widespread use of WPT systems for EVs, as documented in SAE-J2954 [47].

2.3 State of the Art of WPT for EV Charging Systems

Due to various factors, such as heat dissipation in semiconductors and misalignment between windings leading to magnetic medium variation, the resonant circuit parameters of a WPT system may change, affecting the system's performance. To address this issue, the researchers in [48] have proposed the implementation of a resonant magnetic coupling configuration for WPT, utilizing series compensation circuits for both the transmitter and receiver along with a fuzzy logic controller that adjusts the system by varying the switching frequency to uphold the magnetic circuit's tuning. As determined by the analysis provided, it has been established that when the impedance angle equals zero, the voltage and current in the system are synchronized perfectly. As a result, any alterations made to the load or coupling coefficient, or both, will not cause any detuning in the system. This means the system will continue operating seamlessly even if the load or coupling coefficient changes. This confirms that the resonance point is where maximum efficiency is achieved. However, it is essential to note that this does not necessarily mean that the resonance point delivers the highest power output to the load. The results show that the system achieves efficiencies close to 77% and 73% for the primary and secondary circuits, respectively, outperforming traditional Inductive Power Transfer architectures. It should be brought to attention that the analysis mentioned earlier does not consider the losses that may arise from switching frequency shifts. Such a scenario could cause the system to operate outside the soft-switching range, resulting in it being classified as a hard-switching system.

A crucial aspect of EV development is the advancement of battery storage technology, which aims to enhance storage capacity, decrease charging times, and minimize costs. Currently, lithium-ion batteries are the predominant choice. In this context, the author in [49] examines various characteristics, including accumulator technologies, models, charging types, thermal

analysis, and diverse charging methods. The significance of the Battery Management System (BMS) is highlighted, as it plays a vital role in the functioning of EV batteries, where user safety is of utmost importance, as summarized in the accompanying table.

Table 2.2: Li-Ion Battery Types: Source [49].

Battery Type	Cathode Material	Anode Material	Nominal Voltage (V)	Life Cycle	Energy Density (Wh/L)	Cost	Safety
Lithium Iron Phosphate ($LiFePO_4$)	$LiFePO_4$	Graphite	3.2	High	Low	High	Safest Li-ion cell Chemistry
Lithium Cobalt Oxide ($LiCoO_2$)	$LiCoO_2$	Graphite	3.6	Medium	High	Low	Highest safety concern
Lithium Nickel Manganese Cobalt Oxide ($LiNiMnCoO_2$)	$LiNiMnCoO_2$	Graphite	3.6	Medium	High	Medium	Good Safety
Lithium Manganese Oxide ($LiMnO_2$)	$LiMnO_2$	Graphite	3.7	Low	Low	Medium	Good Safety
Lithium Nickel Cobalt Aluminum Oxide ($LiNiCoAlO_2$)	$LiNiCoAlO_2$	Graphite	3.6	Medium	High	Medium	Safety Concern Required

Another essential factor to consider is the charging time and method of the battery. Both CC and CV charging techniques require careful management to ensure their efficiency and to maintain the battery's longevity, as excessive charging currents can shorten the battery's lifespan. In contrast, CV charging focuses on identifying the optimal moment to maintain a fixed charging voltage while gradually reducing the current, all without increasing the battery's temperature. This process is detailed in [50], where the analysis illustrates that an optimal charging cycle for a lithium battery should adhere to the guidelines presented in Figure 2.2.

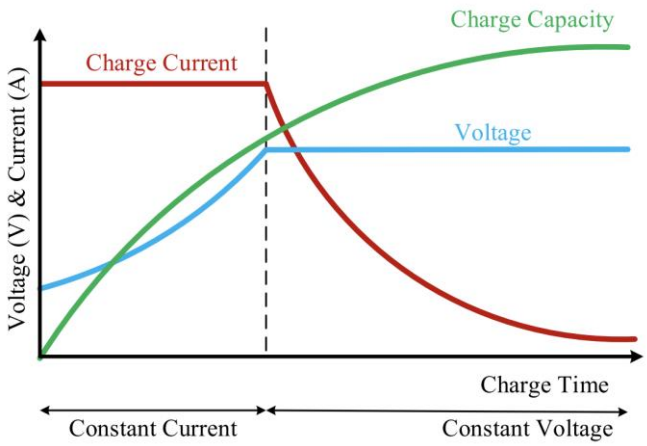

Figure 2.2: CC – CV Charging approach

Two critical parameters to consider when designing inductors for WPT systems are the coupling coefficient and quality factors. The coupling factor represents the proportion of electromagnetic flux originating from the transmitter coil (T_x) transmitted to the receiver coil (R_x). On the other hand, the quality factor is a metric that describes the inductance's stability concerning the winding's geometrical features. Achieving optimal efficiency in EVs requires careful consideration of the Q, coupling coefficient (k), and distance, among others. Generally, increasing the quality factor and coupling coefficient while reducing the distance between components can improve efficiency. An analysis of such quantities is presented in [51] for traditional IPT and

MCR-WPT systems, whose basic configurations are illustrated in Figure 2.3. The work demonstrates that the MCR-WPR technology demands higher values for the assessed parameters and involves additional design complexity. The study also shows that the two technologies can reach a theoretical efficiency of up to 98%. As the design's quality factor increases, the inductor's physical design becomes more complex. Therefore, it is essential to consider power losses in both the copper and core windings when evaluating the efficiency of an MCR-WPT system.

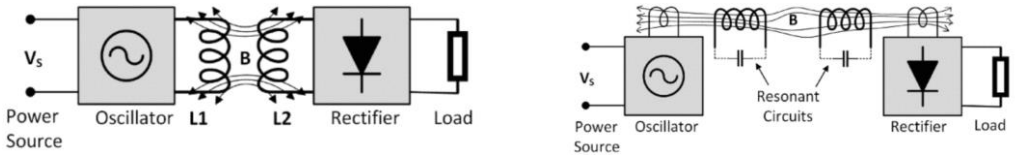

(a) (b)

Figure 2.3: (a) Inductive coupling method. (b) Magnetic resonant coupling method. Source: [51]

Another important issue when analyzing the coupling factor between the primary and secondary circuits is the constructive characteristics of the windings. An approach based on simulations is presented in [52], in which different manufacturing possibilities for double-sided winding structures with distinct conductor characteristics are analyzed. It is worth noting that the system's efficiency is also impacted by the coupling coefficient, making it a crucial factor to consider. A maximum coupling coefficient of approximately 62% can be achieved with the appropriate number of turns and diameter. It is recommended to use this value as a reference point. Additionally, the double-layer structure, which minimizes the number of outer layer turns, has enhanced the coupling coefficient and resisted the radial offset in quantity and quality.

Various techniques have been suggested in the literature to identify mutual inductance for single-transmitter and single-inverter WPT applications without a communication system. However, MCR-WPT systems with multiple transmitters and receivers have seldom been studied regarding their mutual inductance. A recent study by researchers at [53] proposed an identification approach for mutual inductance in a static multi-transmitter resonant WPT system. The method involves driving current from a single transmitter while blocking all others, and then determining the mutual inductance sequentially for each transmitter by measuring the DC bus voltage and the transmitter's Root Mean Square (RMS) current values. When approached as an optimization problem, this method was highly efficient in terms of computational cost for identifying mutual inductance. Additionally, from a hardware perspective, it boasts the advantage of requiring only one current sensor for each transmitter. As a result, it can achieve an impressive 96.89% success rate in determining the value of "*k*" even surpassing the effectiveness of a single transmitter system. The structure has a high level of accuracy that is suitable for a wide range of mutual inductances and can be easily integrated with any multi-transmitter system, regardless of the transmitter system used or the load level applied. This level of interoperability makes it adaptable and scalable to meet the needs of various settings.

The work in [54] assesses the PTE in an MCR-WPT system. The authors incorporate two independent coils into the transmitter and receiver, resulting in a resonant coupling system with four coils. The magnetic field would substantially affect the coupling coefficient, mutual inductance, and overall MRC performance. This arrangement enhances the coupling coefficient between the inductors, yielding a higher efficiency of 76.3% for a transmission distance equivalent to 1.33 times the diameter of the coils. According to the results of the study, the performance of the 4-coil system in terms of separation distance was found to be 24% better than that of the two-coil system. Moreover, at a separation distance of 6.5 cm, the improvement exceeded 50%. These findings suggest that the effectiveness of the design increases as the separation distance surpasses the radius of the coil. In other words, the further apart the coils are, the better the system performs. This information is beneficial for designing and optimizing electromagnetic systems for various applications.

Distinct constructive characteristics, such as geometry, conductor type, and core features, can be considered in implementing the inductors that constitute the transmitter and receiver. This is because all the issues above influence the quality factor. In this sense, the study carried out by [55] proposes an inductor topology that best suits the magnetically compensated WPT system, considering circular, square, and square superimposed geometries. The study concluded that the planar inductor with a circular geometry presented the best performance for an MCR-WPT system, achieving an efficiency of 92.4% in terms of energy transferred to the load with a mutual inductance of 1.17 μH. The relationship between the receiver open-circuit voltage and the transmitter current, known as mutual inductance, can be influenced by external variables such as T_x and R_x misalignment. To account for this, the authors simulated a Gaussian distribution and confirmed the results through experimentation. The coil location was determined by variations in both the *x* and *y* axes, while changes in the *z-axis* accounted for air gap variance between the coils.

It is also noteworthy that the higher the mutual inductance, the lower the system efficiency. This is a fundamental concept when validating a WPT system in which two coils are close. A misalignment between the coils and a variation in the distance between the windings directly affect the resulting mutual inductance between the primary and secondary windings. A two-coil arrangement placed on the primary side is assessed in [56], in which the tests consider overlapping conditions of one-third and one-half the radius and non-overlapped coils. The results show that one-half the radius leads to the best performance in terms of stability in the mutual inductance. Therefore, this issue will likely influence the conversion efficiency of the power delivered to the secondary side, resulting in a maximum coupling coefficient close to 27% and a mutual inductance of around 100 μH. Thus, one way to overcome the inconvenience of misalignment is undoubtedly incorporating an additional coil into the primary side.

One crucial factor to consider is the behavior of the nonlinear load, which is connected to the receiver side of the WPT. A comprehensive study, as presented in [57], highlights the significance of the system's behavior as both a constant current source (CCS) and a constant voltage source (CVS). A continuous current is required to ensure optimal load until the battery reaches the desired voltage levels. Therefore, a hybrid compensator topology LCC series-parallel (LCC-SP) is proposed, which allows the WPT system to behave as either CCS or CVS based on load requirements. The analysis is conducted to validate switching losses and efficiency and assess the harmonic content of the output wave. The proposed topology demonstrates a satisfactory response regarding zero-voltage switching (ZVS), with smooth switching between CCS and CVS guaranteed, minimizing losses associated with the switches. The efficiency of the LLC-SP system is 90.14%, which is higher and more efficient than other high-order compensation circuits. Furthermore, it is more economical. The authors in [58] suggest a modified approach involving a constant power source (CPS) instead of a CCS to address issues related to excessive component heating. However, this change results in a broader range of load resistor variation compared to the previous method. To overcome this drawback, a full-bridge active rectifier (FBAR) presented in Figure 2.4 is proposed, which ensures ZVS, eliminates the need for primary-secondary communication, and supports a broader range of load impedance conversion. An experimental prototype of 150 W was tested under coupling coefficients *of k = 0.2 and k = 0.15, yielding* efficiency levels of 93.7% and 92.5%, respectively. The controllable range of load resistance variation was between 6 and 20 ohms.

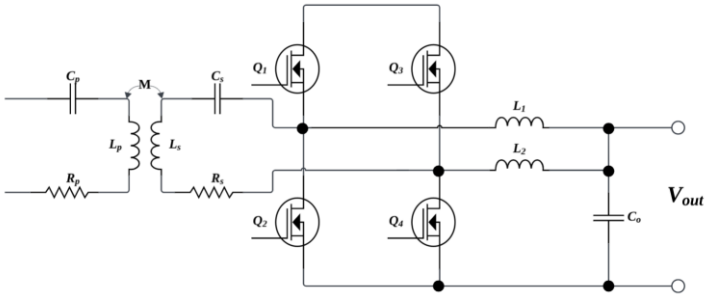

Figure 2.4: Full-Bridge Active Rectifier

The battery-charging mode in stationary parking, which eliminates the need for a wire connection, requires the use of a relatively simple IPT system by adjusting the distance to optimize transmission efficiency. Nevertheless, an interoperability analysis is necessary to define proper standards while considering distinct IPT architectures [59]. A typical figure of merit in a WPT system is the transmission efficiency between the primary and secondary inductors. The analysis developed in [60] demonstrates that this parameter depends directly on the operating frequency, the coupling coefficient, and the physical characteristics of the inductors. The coupling coefficient is directly related to the mutual inductance ratings, which influence the overall system efficiency. Given the above, the authors state that, for each coil type, one can determine an optimum distance for which the inductor will operate under the critical coupling coefficient. This parameter is

specified mathematically according to the winding's geometry and specifications. The results showed that optimal distances of 5 cm, 7 cm, and 12 cm are obtained for three distinct inductors with a diameter of 15 cm while varying the cross-sectional area of conductors and the number of turns. Thus, it resulted in critical coefficients of 0.23, 0.14, and 0.07, respectively. In other words, the smaller the coupling coefficient of the inductor, the longer the maximum transfer distance.

When a WPT system experiences misalignments, it can decrease the power delivered to the load, instability, and increase energy losses. To address this issue, various studies have explored ways to improve the misalignment tolerances in magnetically coupled systems. One approach is to reduce the variation of the mutual inductance between the windings. At the same time, another involves using compensating circuits or adopting control strategies that equalize the mutual inductance under critical misalignment conditions. In [61], the authors propose a solution that adds a reverse bias inductor to the primary winding of the WPT system. This ensures mutual inductance remains stable despite magnetic circuit misalignments. The approach achieves an efficiency of 93% under misalignment conditions up to 40% of the set point while maintaining the soft switching characteristic and not affecting the efficiency of the system when compared to a typical LCC compensation model. A different approach to address the impact of mutual inductance variation on system efficiency is outlined in [62]. The authors examine the displacement in the *x*, *y*, and *z* axes and the rotation of the windings about each other. To solve this issue, they propose an LCC-series compensation topology with a resonant L-C circuit next to the transmitter. This generates a second resonant source, adding another level of freedom to the analysis. Practical validation showed an efficiency of 85.22% at a 150 mm separation. Additionally, the input maintains a zero-phase angle (ZPA) within a misalignment tolerance of ±200 mm in both the x and y axes, as well as a 20° rotation. The system still functions as a CCS for load resistance variations between 5 Ω to 20 Ω.

In [63], the authors propose a topology consisting of two inductors on the T_x side, each controlled by a single switch. This approach effectively reduces the number of required semiconductor elements, and with the proper control strategy, it addresses the problem of misalignment in a WPT system. However, it is worth noting that this approach results in a slight decrease in efficiency. Specifically, when the load resistance varies due to displacement, the voltage stability is maintained at the expense of reduced load current and transferred power. In practice, this translates into an efficiency drop from 89% to 84% when load resistance varies between 30 Ω and 80 Ω, generated by a misalignment between -6 and 10 cm. This issue arises primarily due to overlooking the fluctuation of mutual inductance between the primary and secondary windings. As previously examined, this directly impacts the efficacy of the WPT system, resulting in overheating and disruption of the resonant magnetic circuit. Additionally, this could lead to switching losses in the active switches.

A study carried out in [64] considers the influence of the transmission medium on the WPT system since, at low frequencies, the losses caused by the series resistance of the inductors are predominant when compared to the ones generated by the electromagnetic radiation effect. However, the latter portion cannot be neglected at high frequencies since the eddy currents will strongly influence the system's efficiency. The authors also considered a 5-cm block with different conductivity ratings of the magnetic circuit, varying from 0 S/m to 8 S/m. The results showed that higher operating frequencies are preferred for lower conductivity values. The best performance in media with a higher conductivity occurs at lower oscillation frequencies. When comparing the traditional IPT and MCR-IPT systems, the latter demonstrated improved performance, considering the same distance and geometry.

As previously mentioned, the plate type is the best-performing inductor geometry for WPT systems. In this way, the work in [65] presents an approach for which the constructive characteristics of a planar inductor of a circular shape are investigated. The plate's external radius, the conductor's diameter, and the separation distance are carefully assessed. The authors concluded that a winding with a smaller cross-sectional area and a higher number of turns performs better than one with a higher cross-sectional area and a lower number of turns, considering the same plate diameter. Thus, the coupling coefficient varies because it depends directly on the inductance, resulting in a variation in the resonance frequency. Consequently, including a tuning system is necessary to ensure the proper coupling of inductors and enhance the system's performance.

Although the LCC is a popular choice for the primary compensator circuit due to its ease of design and implementation, it has several drawbacks, including limited design flexibility, sensitivity to misalignment, and lack of open circuit protection. As a solution, researchers have proposed in [66] an in-depth analysis of alternative primary high-order compensator topologies (PHCT). While the mathematical procedures for analyzing PHCT are more complex than usual, the investigators evaluated the performance of a prototype from 250W of power and a 100mm coil separation distance. The results show that the order five compensator circuit achieved 90% efficiency, and the order six compensator reached 92% efficiency. However, implementing a higher-order compensator block can increase the system's size and cost, so it is up to the designer to balance the desired efficiency with practical considerations.

2.4 Review of Resonant Inverter Topologies for WPT Applications

A resonant inverter comprises switches and high-order filters, transforming DC voltage into high-frequency AC voltage. The converter switching frequency matches the output frequency, which can cause significant switching losses with high-frequency modulations like sinusoidal pulse width modulation (SPWM). This modulation is not suitable for WPT systems [23].

Comparing a high-frequency resonant inverter with a low-frequency one reveals several advantages, such as high efficiency, high power density, and fast dynamic response. These benefits make them attractive and interesting in both academic and industrial fields for WPT applications in EVs. Their soft switching characteristics and low harmonic content are particularly beneficial. Selecting the appropriate power converters for compensation circuits is crucial to ensure optimal power transfer efficiency. The series-series (S-S) and inductor-capacitor-capacitor (LCC) resonant topologies are noteworthy options for WPT systems. The S-S configuration allows for higher voltages on the emitter side. In contrast, the LCC resonant circuit on the secondary side behaves as a controlled current source, making it an ideal choice for EV battery charging applications [67].

The high-frequency inverter on the transmitting side facilitates the generation of sinusoidal current waveforms and energy transfer between the coils. While half-bridge and full-bridge inverters are straightforward options for this task, there are some challenges to consider. Semiconductors operating under hard-switching conditions, high conduction losses, and elevated electromagnetic interference (EMI) levels justify careful attention.

To address the limitations mentioned, resonant inverters with soft-switching characteristics offer a more appealing solution, with reduced switch stress, increased power density, and higher efficiency. Depending on the resonant tank configuration, the available topologies can be categorized as series, parallel, or series-parallel converters [68]. Various structures have been explored in WPT systems, including class E, class E^2, class D, class EF, class EF_2, and class DE inverters [17].

The class E resonant inverter shown in Figure 2.5 is a highly efficient single-switch topology that reduces losses using a low component count [69]. Its unique design enables ZVS and zero-derivative-voltage switching (ZVDS), ensuring optimal operation. One can adjust the switching frequency, DC input voltage, or duty cycle to control the inverter output voltage. However, frequency control may be less effective under light-load conditions. It is important to note that this topology requires a choke inductor, adding complexity to the mathematical model and system design. Furthermore, careful attention must be paid to the physical implementation of magnetic elements, which are responsible for energy transfer, as is the case with L_r, which requires a high-quality factor and may affect the WPT circuit's mutual inductance and coupling coefficient. Finally, it is worth noting that the peak voltage across the switch can reach up to 3.5 times the DC input voltage, making this topology more suitable for low-power applications.

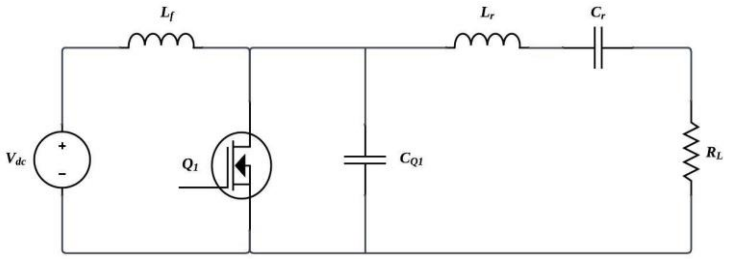

Figure 2.5: Class E inverter

The class EF, presented in Figure 2.6, utilizes a similar active switch as the class E topology, but with the addition of a parallel capacitor to the inductor-capacitor branch. This results in a peak switch voltage that is 2.5 times the DC input voltage, while allowing modifications to the switched waveform. An optimal duty cycle of around 30% can be employed using reactive elements. The EF inverter boasts a broad frequency range, reaching several megahertz, and delivers high performance and power output. However, it is less tolerant of misalignment, and its complex control system design and mathematical modeling may be attributed to its high component count.

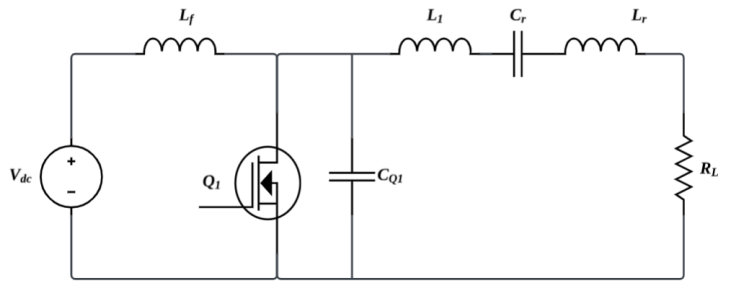

Figure 2.6: Class EF inverter

The prerequisites for a WPT system to be deemed suitable for home use or integration into public charging stations include maintaining CC and CV at the battery charging terminals, while ensuring a power factor close to unity with the primary power supply. In their publication [70], the authors propose a solution that employs the EF_2 inverter topology shown in Figure 2.7, to generate a high-frequency AC waveform, with CC, CV, and PFC characteristics achieved through gate control of a single switch. After analyzing a prototype scaled to a 200 W power output, they could transfer up to 12 cm for a 24 V and 30 Ah battery with an efficiency of 85.5%. However, adding a communication module between T_x and R_x was necessary, increasing the system's complexity, size, and production costs and ultimately limiting its use to vehicles that conform to the adopted communication method.

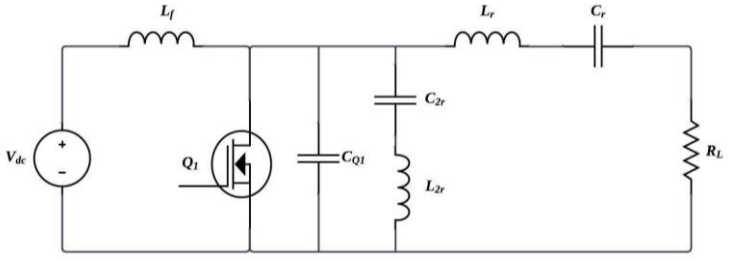

Figure 2.7: Class EF_2 inverter topology

Figure 2.8 presents the Class D inverter topology, which can operate at high frequencies, enabling the use of smaller components. It is frequently paired with soft-switching techniques to minimize switching losses and enhance the efficiency of WPT systems. While it is efficient, one of the primary challenges lies in maintaining a stable output under varying load conditions or coil misalignment. This may require advanced control techniques, as the system is susceptible to load fluctuations and coupling variations [71].

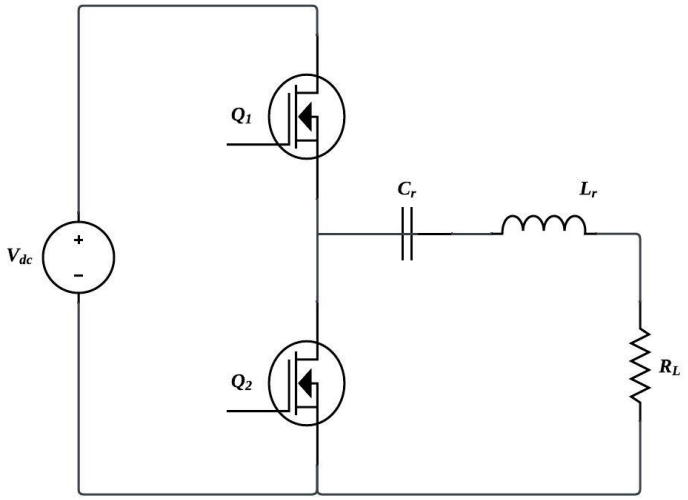

Figure 2.8: Class D Inverter topology

The class DE inverter is an advantageous topology due to its ability to facilitate soft switching of active switches and reduce voltage and current stresses. Additionally, the control system can be designed to maintain a constant load voltage, so variations in load caused by emitter-receiver misalignment shouldn't affect system performance. This topology is highly efficient in high-frequency DC-AC conversion and is widely used across many applications. Depending on whether a series or parallel-resonant tank is used, it can act as either a voltage or current source and ensure soft switching under ZVS or ZVDS conditions during turn-on and turn-off, respectively [72].

The demand for higher power and redundancy in WPT systems has recently posed a challenge, regardless of the inverter topology used. There are two ways to approach this challenge: one is by adopting an inverter with a high rate of managed power, which can be costly to implement and may result in power source failure in case of a malfunction. The other option is to connect low-power inverters in series or parallel, which increases system stability and ensures operability in case of power failures while providing a more comprehensive range of available power levels. When using multiple inverters, the heat generated by the system is distributed evenly, which can help alleviate heat dissipation issues. This approach also offers greater flexibility when working with higher power levels and can be more cost-effective for expansion. However, there are some potential drawbacks to using multiple inverters. Inevitably, the components used in each inverter will have different intrinsic parameters, such as activation time,

which can lead to discrepancies between their outputs. A phase shift or output voltage or current difference can seriously compromise the system's efficiency and cause electromagnetic interference between the inverters. Additionally, an inverter with multiple stages in parallel or series must ensure stability between its subcircuits to achieve balanced power distribution and reduce current flow between inverters [73]. Various methods have been explored to maintain balance between the inverters, with particular emphasis on those that utilize magnetic circuits and delta or star connections between the different inverter arms. After careful analysis, the most effective approach was coupling circuits with inductors or transformers. In this sense, the authors of [74] have developed a configuration that combines inductors in star and delta topologies, achieving a current balance of nearly 100% and an efficiency rating of 94.46% for a transferred power of 800 W. In contrast, the research outlined in [75] introduces the use of two transformers, one for each inverter, to achieve current balance in the transmitter. Notably, this proposed topology provides impedance-matching capability and isolates the balancer's output from its input. Experimental results demonstrate that current balance is attained when the output voltage of each inverter differs by no more than 8 ns. However, it is worth noting that including transformers in the system may introduce new mutual inductances, which could impact the system's overall efficiency. This facet has yet to be analyzed in the proposal. Other considerations are studied in [76]; for example, various EVs with different charging power levels and different vehicle assemblies (VA) can be set by different charging station assemblies (CSA). However, it is essential to note that the efficiency of the WPT system can drop significantly when there is a significant difference between CSA power and VA power. To address this drawback, the authors propose a solution involving a parallel DC-link for the secondary and an AC-link in series for the primary, which results in a high-power WPT system. By implementing a control method based on mutual inductances analyses, they achieved an efficiency of up to 97.5% in the energy transfer to the load for a 20kW prototype system.

2.5 Review of Control Strategies Applied in WPT Systems from EVs

In a WPT system, misaligned coils can reduce transmission efficiency. To address this issue, various techniques, such as proportional-integral (PI) control, perturb and observe (P&O), and sliding mode control, have been proposed in the literature to regulate the load voltage [77]. A widely used method is variable frequency control, which adjusts the switching frequency of the resonant inverter to ensure proper magnetic coupling while accounting for changes in the load resistance. However, it is essential to note that reactive power flow through the system may result in a notable decrease in efficiency [78].

An alternative approach involves manipulating the DC input voltage. However, implementing a front-end DC-DC converter becomes essential, leading to added expenses and losses. To address this, the experts in [79] propose a dual-side control method for WPT systems

that utilize series compensation for both the transmitter and receiver. One can attain the maximum efficiency point by adjusting the duty cycle in the primary-side inverter. The controller on the secondary side then regulates the load voltage based on this. Yet, note that this design necessitates a wireless communication module.

The researchers in [80] proposed a control technique for adaptive frequency tracking that involves detecting the phase angle between load current and voltage. This information is then fed into a neural network to generate tuning parameters for a proportional-integral-derivative (PID) controller and adjust the switching frequency. Meanwhile, reference [81] suggests a dual-loop cascaded control solution for eV battery charging, utilizing linear controllers. Nevertheless, the closed-loop control system's bandwidth remains a significant limitation.

In a study depicted in [82], a control strategy was evaluated for MCR-WPT systems with multiple frequencies and loads. This method uses multifrequency modulation waves to drive the resonant inverter through mutual inductance coupling. The result is an inductive power transfer that accommodates multi-resonant networks on the secondary side. Another approach in [83] examined the impact of mutual inductance and coupling coefficient on maintaining efficiency above 80%; the resonant circuit utilizes bilateral phase-shift control, necessitating feeding the current induced on the secondary side back into a neural network to obtain active switch drive signals. However, this approach requires a wireless communication system for data transmission between the primary and secondary circuits. A different topology was presented in [84], where a control strategy that permits variable phase-shift angles regulates load voltage and active switch operation under ZVS conditions. An optimization method is also employed to determine the optimal operating point. As the transmission distance increases, the transmitted power and efficiency decrease because the coupling coefficient between the inductors becomes extremely low. A first obvious choice could be using coils with a high self-inductance by increasing the number of turns, but it will lead to additional losses in the windings associated with increased size, weight, volume, and cost.

In [85], the objective is to enhance the circuit efficiency by reducing the losses that arise when the primary and secondary currents reach equilibrium. The proposed solution involves utilizing multilayer coils in primary and secondary circuits, resulting in an impressive 80% efficiency for transmission distances up to 100 cm.

In [73], the authors propose a mathematical model for a WPT system with an LCC compensator circuit for the primary and a resonant series tank for the secondary. They suggest using genetic algorithms to adjust the quantities associated with distance transmission and alignment, which allows for controlling the load voltage by changing the duty ratio of the active switch. In [86], a hybrid control solution is presented, which uses small variable capacitors to

regulate the load voltage by changing both the switching frequency and impedance of the resonant tank. However, this method requires a complex strategy for driving the switches associated with the shunt capacitors.

To achieve optimal resonance frequency in a WPT system, control measures are discussed in [80]. The author notes that implementing a frequency tracking model can be highly complex due to its non-linear behavior, as variable switching frequency can result in significant energy losses. As such, bilateral control techniques have been extensively explored in various works found in the literature [87].

2.6 Final Considerations

This chapter presented an approach that considers the most relevant aspects for understanding WPT technology.

RIPT, then, is the option best suited to EV charging due to its ability to operate in near-resonant switching, which increases its efficiency and improves its transmission distance, being feasible even with the interconnection of several inverter modules, thus reaching higher power levels.

After evaluating various resonant inverter topologies, it was possible to identify the advantages and disadvantages of each. The class DE resonant inverter is considered the most optimal option due to its ability to ensure a smooth switching of its semiconductor components. This is achieved by satisfying the ZVS and ZCS conditions upon disconnection. Additionally, its topology structure has fewer elements, making it an appealing choice in terms of implementation cost and size. Overall, the class DE resonant inverter proves to be a highly efficient and reliable power conversion solution. A variety of methodologies have been described for controlling class DE inverters. The feasibility of applying digital control methods with Artificial Intelligence (AI) opens new opportunities to propose strategies for improving system performance.

Chapter III

CLASS DE RESONANT INVERTER: THEORETICAL ANALYSIS, MODELING, AND CONTROL

3.1 Preliminary Considerations

This chapter introduces the primary contribution of this work. Using the transfer function that characterizes the resonant topology, a mathematical model is developed to determine the turn-on times for each semiconductor element, ensuring a consistent output voltage despite variations in load resistance.

The model is built on the band-pass filter criterion, which is applied to the resonant circuit to derive the Fourier series for the first harmonic. This information generates a function representing the voltage values at the output, regulated through the turn-on instants of the active switches.

Using an ADALINE neural network, future values can be projected based on current and past values. This results in a discrete-time transfer function that establishes the parameters for controlling the commutated elements within the resonant inverter topology.

This chapter presents mathematical models for the class DE inverter circuit. The resonant circuit configurations analyzed are:

a) series resonant circuit,
b) parallel resonant circuit,
c) series-parallel resonant circuit.

In addition, the differential equations for each resonance model are depicted together with the mathematical analysis that yields the transfer function for inverter control. After undergoing ADALINE network training, an ARX model is produced, enabling the acquisition of inverter control pulses through a digital controller setup.

3.2 Theorical Analysis of The Class DE Resonant Inverter

The Class DE resonant inverter depicted in Figure 3.1 has been selected for the proposed WPT system because it can operate at high switching frequencies in the megahertz range and offers the soft-switching characteristics of the Class D topology, along with the high efficiency of the Class E topology. The circuit comprises a DC voltage source V_i, two switches (Q_1 and Q_2), two shunt capacitors (C_{Q1} and C_{Q2}), a resonant capacitor (C_{res}), a resonant inductor (L_{res}), and a load resistor (R_L). Furthermore, the input and output voltage transfer function corresponds to the mathematical expression outlined in (3.1) [88]. Notably, this expression comprises solely the inverter's passive elements, thereby ensuring the system's controllability.

$$G_{DE}(s) = \frac{\frac{R_L}{L_{res}} s}{s^2 + \frac{R_L}{L_{res}} s + \frac{1}{L_{res} C_{res}}} \tag{3.1}$$

By measuring the variations in resistance within the magnetic circuit on the primary side and utilizing a microcontroller system that integrates a predefined reference signal, one can achieve a regulated output. This output is crucial for determining the activation timing of the switches in the class DE inverter. The zero-crossing detector offers guidance to ensure smooth switching operations for both current and voltage when functioning at the resonance frequency.

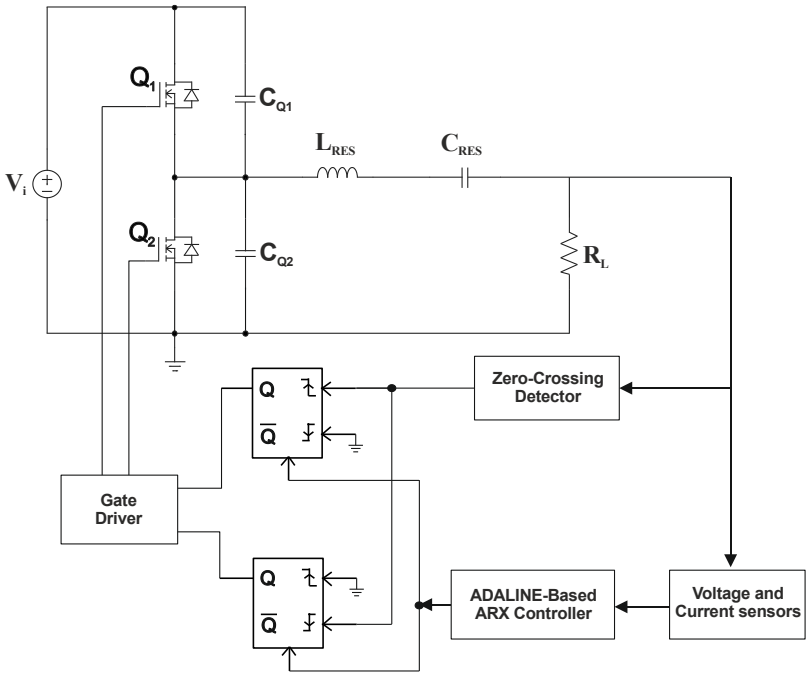

Figure 3.1: Class DE Resonant Inverter.

Figure 3.2 represents the waveforms of the class DE inverter. The drive signals of the active switches corresponding to $v_{g(Q1)}(t)$ and $v_{g(Q2)}(t)$, respectively, are shifted by one-half of the switching period. Thus, the switches operate under ZVS and ZVDS conditions [89].

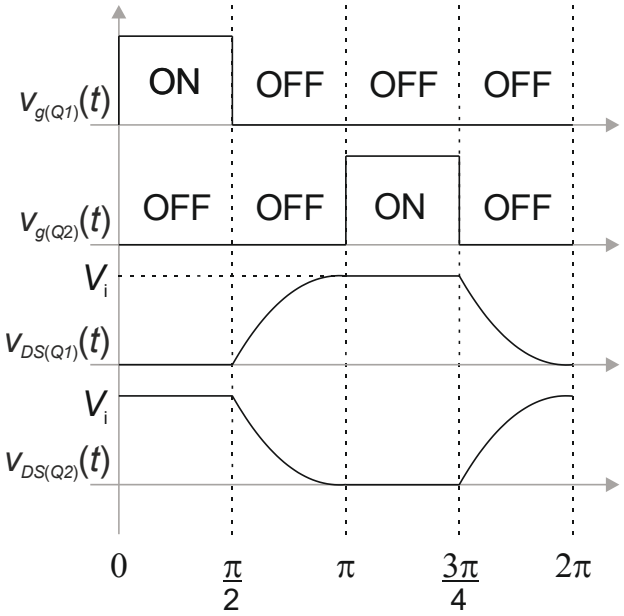

Figure 3.2: Main theoretical waveforms of the class DE resonant inverter.

The waveform of $v_{DS(Q2)}(t)$ is described mathematically expressed in(3.2), where D is the duty cycle of switches Q_1 and Q_2, V_i is the DC source voltage, and ω is the commutation angular frequency.

$$V_{DS(Q2)}(t)=\begin{cases} V_i & 0\le \omega t\le 2\pi D \\ V_i\left[1+\cos\left(\omega t\right)\right] & 2\omega D\le \omega t\le \pi \\ 0 & \pi\le \omega t\le \pi(1+2D) \\ V_i\cos\left(\omega t\right) & \pi(1+2D)\le \omega t\le 2\pi \end{cases} \tag{3.2}$$

According to [90], one can design the components for a class DE inverter with a series resonant circuit that behaves as a constant current source based on equations (3.3) - (3.6).

$$R_L=\frac{V_i^2}{2\pi P_o} \tag{3.3}$$

$$C_{Q1}=C_{Q2}=\frac{1}{2\pi\omega_o R_L} \tag{3.4}$$

$$L_{res}=\frac{Q_{DE}R_L}{\omega_o} \tag{3.5}$$

$$C_{res}=\frac{1}{\left(Q_{DE}-\frac{\pi}{2}\right)\omega_o R_L} \tag{3.6}$$

Where P_o is the output power, ω_o is the angular resonance frequency, and Q_{DE} is the quality factor.

Through the resonant circuit L_{res}, C_{res}, and R_L, the band-pass filter extracts the first harmonic of the signal present at $v_{DS(Q2)}(t)$. This extracted signal is then multiplied by the circuit's inherent gain to produce the voltage signal at the output v_o. Equations (3.7) and (3.8) specifically describe the first harmonic component of the Fourier series for $v_{DS(Q2)}(t)$.

$$v_{ds2}(t)_s = \frac{V_i}{\pi}\left[\pi - 2\pi D - \frac{\sin(4\pi D)}{2}\right]\cos(t-\phi_D) + \frac{V_i}{\pi}\left\{2 - \left[\sin(2\pi D)\right]^2\right\}\sin(t-\phi_D) \tag{3.7}$$

$$\phi_D = \frac{\pi}{2} - \tan^{-1}\left\{\frac{2 - \left[\sin(2\pi D)\right]^2}{\pi - 2\pi D - \frac{\sin(4\pi D)}{2}}\right\} \tag{3.8}$$

Where ϕ_D represents the phase shift caused by the resonant circuit.

One can calculate the voltage gain G_{DE} from (3.9).

$$\left|G_{DE}\right| = \frac{\frac{R_L\omega_o}{L_{res}}}{\sqrt{2\left[\left(\frac{1}{L_{res}C_{res}} - \omega_o^2\right)^2 + \left(\frac{R_L\omega_o}{L_{res}}\right)^2\right]}} \tag{3.9}$$

Then, multiplying (3.7) by (3.9) gives the RMS voltage v_o across the load R_L, expressed in (3.10). Upon analyzing the mathematical function for v_o, it is discernible that the voltage at the load can remain constant even if there are changes in the load resistance value. This can be achieved through the adjustments to the duty cycle D of the switches Q_1 and Q_2, a topic that will be further explored in this work.

$$v_o = \frac{\frac{R_L\omega_o V_i}{\pi L_{res}}\left\{\left[\pi - 2\pi D - \frac{\sin(4\pi D)}{2}\right]\cos(t-\phi_D) + \left\{2 - \left[\sin(2\pi D)\right]^2\right\}\sin(t-\phi_D)\right\}}{\sqrt{2\left[\left(\frac{1}{L_{res}C_{res}} - \omega_o^2\right)^2 + \left(\frac{R_L\omega_o}{L_{res}}\right)^2\right]}} \tag{3.10}$$

By manipulating the equation (3.1), it becomes feasible to express the transfer function of the class DE inverter in terms of the quality factor Q_{DE}, as presented in the equation (3.11). Furthermore, a variable denoted by u (3.12) is introduced for analysis purposes, which signifies the ratio between the circuit's resonance frequency (ω_o) and the switching frequency (ω).

$$G_{DE}(j\omega) = \frac{\frac{\omega_o}{Q_{DE}}j\omega}{(j\omega)^2 + \frac{\omega_o}{Q_{DE}}j\omega + \frac{\omega_o^2\left(Q_{DE} - \frac{\pi}{2}\right)}{Q_{DE}}} \tag{3.11}$$

$$u = \frac{\omega_o}{\omega} \tag{3.12}$$

By substituting (3.12) into (3.11), and computing the absolute value, it results the expression presented in (3.13), enabling to examine the performance of the class DE resonant inverter under Q_{DE} variations from 1 to 5, within a frequency range of $0.9u$ to $1.1u$, as shown in Figure 3.3.

$$|G_{DE}(u)| = \frac{u}{\sqrt{\left(Q_{DE} - u^2\left(Q_{DE} - \frac{\pi}{2}\right)\right)^2 + u^2}} \tag{3.13}$$

After conducting an in-depth analysis of Figure 3.3, it becomes apparent that the frequency range for implementing system control decreases as the value of Q_{DE} increases. Moreover, it is essential to note that a topology with a series resonant circuit will result in voltage reduction behavior when the maximum gain amplitude is equal to unity. This implies that the voltage V_i of the DC source must exceed the desired peak voltage at the load in order to maintain a stable power supply. Therefore, it is crucial to carefully consider the values of Q_{DE} and the gain amplitude when designing a resonant circuit system to ensure optimal performance and reliability.

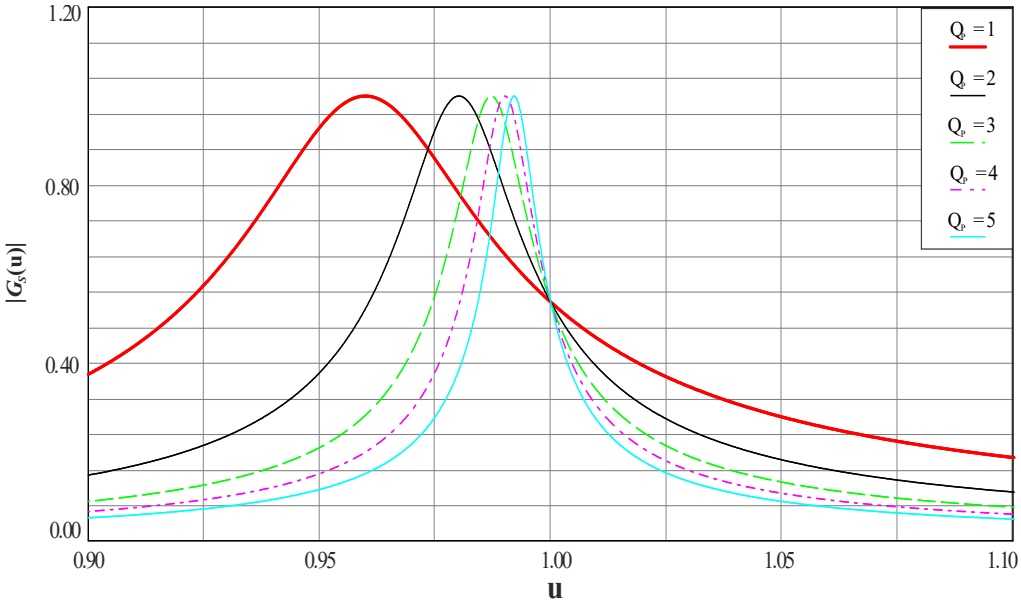

Figure 3.3: G_{DE}(u) module under Q_{DE} variations.

3.3 Parallel and Series-Parallel Resonant Tank Circuit Description.

Identical to what was described before in section 3.2 for the series resonant tank, mathematical analysis has been developed for both parallel resonant circuit [72] and series-parallel resonant circuit [91], presented in Figure 3.4.

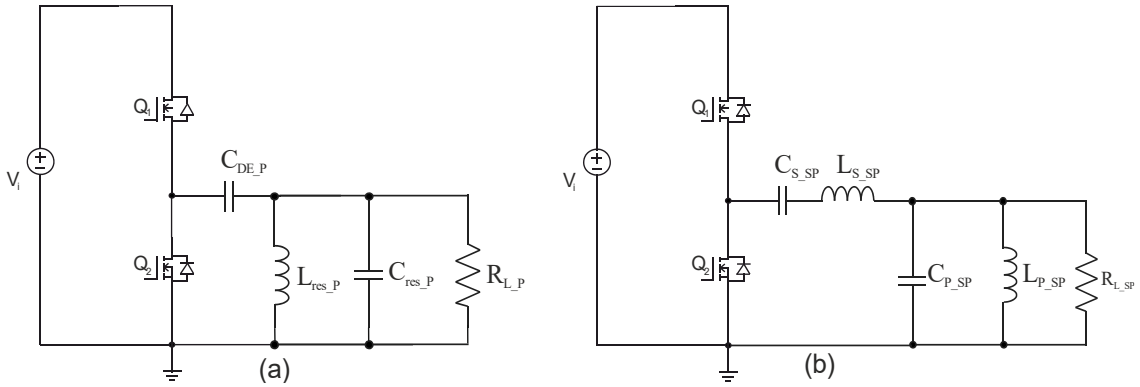

Figure 3.4: Resonant topologies: (a) parallel (b) series-parallel.

The mathematical expressions for designing the parallel class DE resonant inverter topology are summarized in equations (3.14)–(3.17).

$$R_{L\_P} = \frac{V_i^2}{2P_o} \tag{3.14}$$

$$C_{DE\_P} = \frac{\pi}{\omega_o R_{L\_P}} \tag{3.15}$$

$$C_{res\_P} = \frac{2Q_P - \pi}{2\omega_o R_{L\_P}} \tag{3.16}$$

$$L_{res\_P} = \frac{R_{L\_P}}{Q_P \omega_o} \tag{3.17}$$

Where Q_P is the parallel class DE inverter quality factor.

The transfer function for the parallel class DE resonant inverter is outlined in (3.18). One can express $G_{DE\_P}(S)$ in terms of Q_p and u, in (3.19).

$$G_{DE\_P}(s) = \frac{\dfrac{C_{DE\_P}}{C_{DE\_P} + C_{res\_P}} S^2}{S^2 + \dfrac{S}{(C_{DE\_P} + C_{res\_P})R_{L\_P}} + \dfrac{1}{(C_{DE\_P} + C_{res\_P})L_{res\_P}}} \tag{3.18}$$

$$\left|G_P(u)\right| = \frac{2\pi u^2}{\sqrt{\left[2Q_{DE} - \left(\pi + 2Q_P\right)u^2\right]^2 + 4u^2}} \tag{3.19}$$

For the series-parallel class DE resonant inverter, according [91], the design expressions and transfer function are outlined across (3.20)-(3.25)

$$C_{S\_SP} = \frac{\pi}{\omega_o R_{L\_SP}} \tag{3.20}$$

$$L_{S\_SP} = \frac{R_{L\_SP}}{\omega_o} \tag{3.21}$$

$$C_{P\_SP} = \frac{Q_{s-p}}{\omega_o R_{L\_SP}} \tag{3.22}$$

$$L_{P\_SP} = \frac{1}{\omega_o^2 C_{P\_SP}} \tag{3.23}$$

$$G_{DE\_SP} = \frac{\dfrac{S^2}{L_{S\_SP}C_{P\_SP}}}{S^4 + A\cdot S^3 + B\cdot S^2 + C\cdot S + D}$$

$$A = \frac{1}{C_{S\_SP}R_{L\_SP}}; \quad B = \frac{C_{P\_SP}L_{P\_SP} + C_{S\_SP}L_{S\_SP} + C_{S\_SP}L_{P\_SP}}{C_{P\_SP}L_{P\_SP}C_{S\_SP}L_{S\_SP}} \tag{3.24}$$

$$C = \frac{1}{C_{s\_SP}L_{s\_SP}C_{P\_SP}R_{L\_SP}}; \quad D = \frac{1}{C_{P\_SP}L_{P\_SP}C_{S\_SP}L_{S\_SP}}$$

$$\left|G_{S-P}(u)\right| = \left| \frac{(ju)^2}{Q_{s-p}(ju)^4 + (ju)^3 + \dfrac{\pi + \pi Q_{s-p} - 4.61 + Q_{s-p}}{\pi}(ju)^2 + \dfrac{ju}{\pi} + \dfrac{\pi Q_{s-p} - 4.61}{\pi^2}} \right| \tag{3.25}$$

Upon analyzing Figure 3.5, it becomes clear that the parallel tank exhibits a step-up characteristic behavior; in other words, the load voltage is higher than the DC source voltage, which is advantageous when dealing with high load voltage levels in the WPT secondary.

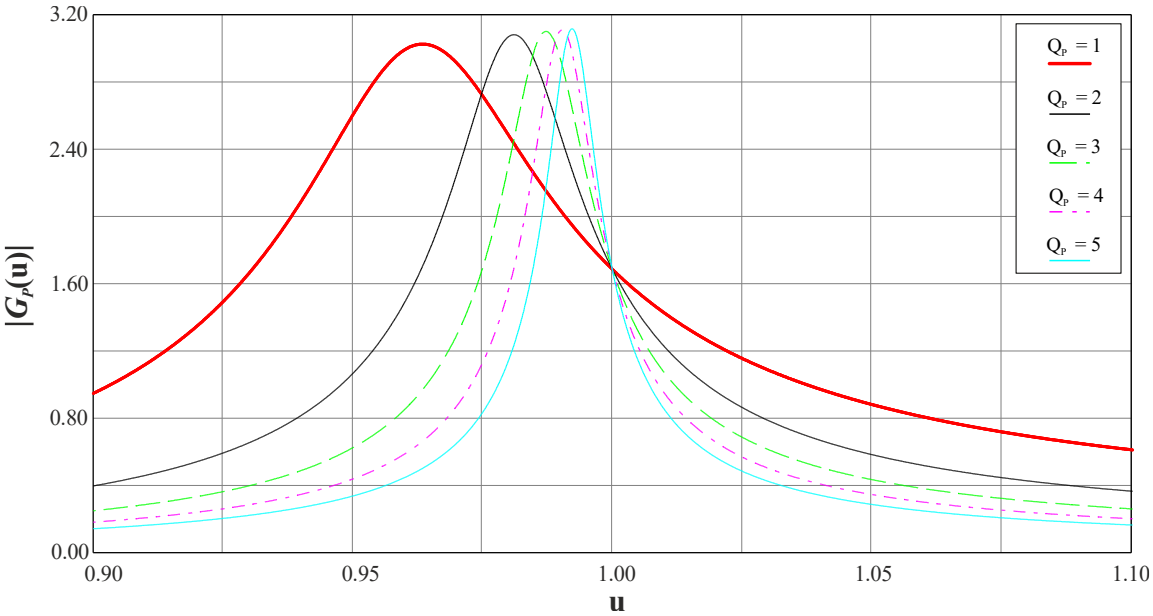

Figure 3.5: Behavior of $|G_P(u)|$ for several values of Q_P.

Further analysis is necessary to verify the response obtained for the $G_{s\_p}(u)$ transfer function. Due to the presence of two resonant circuits, L_s-C_s and L_p-C_p, there are two local maxims, as depicted in Figure 3.6. It is worth noting that the maximum observed at $u=1.05$ indicates that the circuit can operate as a voltage booster or reducer with slight variation. Moreover, increasing the value of $Q_{S\text{-}P}$ has minimal impact on the available frequency range for system control. When the switching frequency ω is greater than the natural frequency ω_o, the system becomes unstable, which makes it impossible to design a control system for this zone. However, during implementation, series-parallel resonant tank design comes with a higher cost and increased physical system size.

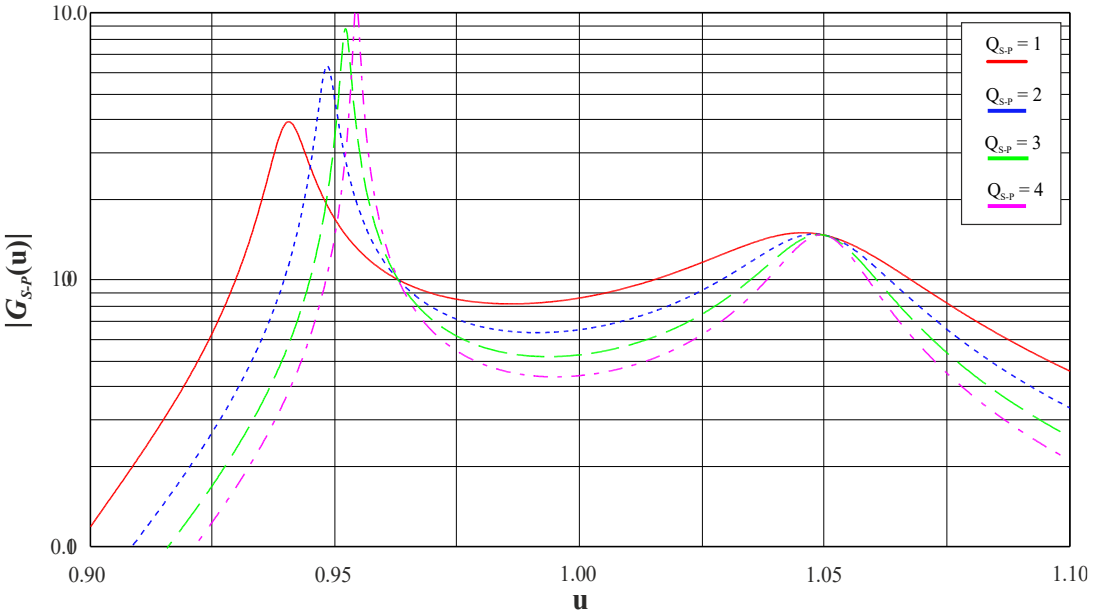

Figure 3.6: Behavior of $|G_{S\text{-}P}(u)|$ for several values of $Q_{S\text{-}P}$.

Based on the premises analyzed, this work aims to develop a control strategy for the class DE inverter with series, parallel, and series-parallel resonant circuits. The objective is to ensure immunity to magnetic circuit misalignment and reduce system losses.

3.4 Proposed Control Approach

The strategy proposed in the present work aims to vary the load resistance of the class DE resonant circuit, which, in turn, is directly associated with the coupling coefficient. Thus, there is no need for a primary compensation circuit because the system operation at the resonance frequency is always ensured. The active switches operate under ZVS and zero-current switching (ZCS) conditions using zero-crossing detectors that rely on an ADALINE-based ARX neural network.

Based on Figure 3.7, the network generates a two-dimensional data matrix comprising the duty cycle values while considering changes in the load resistance between a given predefined range. The matrix is also used for the learning and training process of the neuronal network.

The ADALINE-based ARX model, depicted in Figure 3.7, is a neural network used for data prediction purposes from current and past values [92]. It is mathematically described by the differential equation corresponding to (3.26), and represented as a discrete-time linear system. The known input is the load resistance R_L, while the resulting output is ϕ_D, which defines the duty ratio of switches Q_1 and Q_2 in Figure 3.1

$$\phi_D[k]+a_1\phi_D[k-1]+a_2\phi_D[k-2]+\cdots+a_n\phi_D[k-n]=b_1R_L[k-1]+b_2R_L[k-2]+\cdots+b_mR_L[k-m] \quad (3.26)$$

Where $a_1, a_2, \ldots, a_n$, *and* $b_1, b_2, \ldots, b_m$ are the polynomials estimated by the ARX neural network; m and n represent the linear regression limits for the input and output vectors, respectively; and k is the pointer for an actual value obtained from the input vector R_L[k] and the output vector ϕ_D[k]. In the event of 100% convergence, the values of ϕ_D[k] and ϕ_{RL}[k] would be identical, indicating that the error is zero. However, the chances of achieving such a perfect convergence point are extremely low.

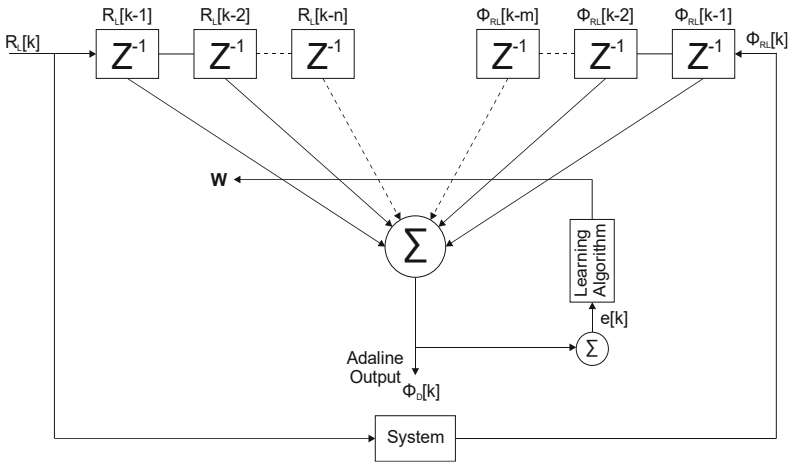

Figure 3.7: ADALINE-based ARX model.

A matrix was obtained by manipulating the data to establish the relationship between the R_L and ϕ_D values required to maintain a constant output voltage v_o. This matrix has a size of [3000 x 2] and was utilized to implement an algorithm for training the ADALINE-based ARX neural network in MATLAB® software.

When training the ADALINE-based ARX neural network using the Least Mean Squares (LMS) rule, the effective division of the dataset is essential for achieving stable convergence and strong generalization. Standard practice, as highlighted in machine learning literature [93], suggests allocating between 70% and 80% of the data to the training set and between 20% and 30% to the validation set. This ratio ensures that the algorithm has an adequate number of samples to adjust the synaptic weights while minimizing the MSE. By using this algorithm, it was made possible to calculate the weights vector w, which contains the corresponding values a_1 to a_n and b_1 to b_m of the z-variable for the discrete-time transfer function in (3.27). This process was crucial in achieving accurate and consistent results in the system. The performance measure was

determined by comparing the mean square error (MSE) of the data obtained through the ADALINE-based ARX model ϕ_D with the expected analytical data ϕ_{RL} from the matrix.

Applying the Z transform to (3.26), one can obtain the discrete-time transfer function of the controller used by the class DE resonant inverter as in (3.27).

$$\frac{\phi_D[z]}{R_L[z]} = \frac{b_1 z^{-1} + b_2 z^{-2} + \cdots + b_m z^{-m}}{1 + a_1 z^{-1} + a_2 z^{-2} + \cdots + a_n z^{-n}} \tag{3.27}$$

Applying the bilinear transform to (3.27) yields (3.28), which is the continuous-time transfer function corresponding to the ADALINE-based ARX controller with 2-step regression from both R_L and ϕ_{RL} proposed in this work for the Class DE inverter with series resonant circuit. The error associated with the linear approximation also influences the second-order transfer function H_{DE}(s). However, some preliminary tests showed that adopting a higher-order model does not significantly decrease the MSE. Therefore, good trade-offs between complexity and accuracy result when representing H_{DE}(s) as in (3.28).

$$H_{DE}(s) = \frac{-1.11\times10^{7} s + 2.604\times10^{10}}{s^2 + 5.719\times10^{5} s + 1.243\times10^{11}} \tag{3.28}$$

To evaluate the proposed solution, it is helpful to examine other similar approaches found in existing literature. Taking Table 3.1 into consideration, traditional control methods utilized in WPT will be briefly discussed. Pulse frequency modulation (PFM) is commonly used on the primary side to achieve constant mode control and a constant current [94]. However, if the switching frequency varies too greatly from the resonant frequency, the switches may be unable to maintain soft-switching conditions. On the other hand, pulse width modulation (PWM) applied on the secondary side can help to overcome these issues. By keeping the switching frequency constant and close to, or the same as, the resonance frequency, the reactance associated with leakage inductance and compensation capacitance can be canceled, resulting in soft-switching operation and a higher efficiency [94].

Table 3.1: Comparison of control strategies applied in WPT systems.

Technique	Implementation Complexity	Advantages	Shortcomings
Primary-side PFM control [94]	Simple implementation while relying on a traditional PI controller.	High efficiency due to the ZVS operation and simple control structure.	The feedback communication requires a radiofrequency (RF) transceiver.
Secondary-side PWM control [94]	Simple implementation while relying on a traditional PI controller.	Operation at a fixed frequency and low interference caused by the RF transceiver.	High implementation cost.
TPS control [95]	Moderate implementation complexity.	Low EMI levels. The output voltage contains only odd harmonics.	Sensitivity to load variations. Limited operating range. This strategy is better recommended for higher power levels.
ADC control [95]	Moderate implementation complexity.	Capacity to adapt to varying load conditions. Precise voltage regulation. High efficiency.	The uneven distribution of switching losses in the semiconductors must be considered in the design.

Technique	Implementation Complexity	Advantages	Shortcomings
ACM control [95]	Complex implementation while requiring advanced digital signal processing techniques.	Capacity to adapt to varying load conditions. Reduced stresses on the semiconductors.	The output voltage will contain both even and odd harmonics. Sensitivity to changes in various parameters. The uneven distribution of switching losses in the semiconductors must be considered in the design.
P&O-based impedance matching [96]	A complex mathematical model is required to represent the system transfer function.	The WPT system can operate over a wide load range.	The output voltage will contain both even and odd harmonics. Higher component count.
Proposed ADALINE-based ARX model	Moderate implementation complexity while relying on a straightforward transfer function to represent the system.	Load variations resulting from misalignment between the emitter and receiver are not likely to affect the system's performance.	Deriving the mathematical model is not a trivial task.

In [95], a comparison was made between consolidated fixed-frequency control techniques, including traditional phase-shift (TPS) control, asymmetrical clamped-mode (ACM) control, and asymmetrical duty-cycle (ADC) control. The authors noted that TPS control causes the output voltage to be clamped to zero on both sides, whereas ADC or ACM control allows the output voltage to be clamped to zero on only one side or not at all, respectively. This can lead to nonuniform switching losses in the active switches and the appearance of both even and odd harmonics in the inverter output voltage.

The authors in [96] evaluate the well-known P&O algorithm, which utilizes a single-ended primary inductance converter (SEPIC) on the secondary side of an MCR-WPT system to achieve maximum power point tracking (MPPT) and match load changes by adjusting the duty cycle of the converter. However, this approach inevitably involves redundant power processing, a higher component count, and increased complexity.

3.5 Final Considerations

The class DE inverter has undergone thorough examination and evaluation, considering the various operational scenarios depending on the resonant circuit's features, series, parallel, and series-parallel configuration. It has demonstrated remarkable efficiency, particularly at high switching frequencies, while ensuring that semiconductor voltage stresses remain consistent with the power supply voltage. A concise comparison between the proposed control method and other established approaches in the literature has been outlined.

An exhaustive analysis of its training process and quality indicators has summarized the system as a continuous-time transfer function that effectively relates output voltage to load resistance variations within a defined range. Its ADALINE-based ARX controller boasts an adaptive nature and does not rely on the physical components of the resonant topology for proper control, making it both robust and reliable.

CHAPTER IV

SIMULATION RESULTS AND DISCUSSION

4.1 Preliminary Considerations

To ensure that the transfer functions acquired from the Class DE inverter model with different resonant tanks and the ADALINE-based ARX controller are suitable for use in the WPT system implementation, it is essential to conduct a computational simulation of the system before the experimental phase. To achieve this, the Bode diagrams are plotted, depicting the modulus and phase of the expressions obtained, and these diagrams are compared with the frequency sweep resource (*AC Sweep*) available in PSIM®, the software utilized for this project.

Drawing from the mathematical analysis of the series, parallel, and series-parallel resonant circuits outlined in Chapter 3, a thorough validation of the performance of each topology under analysis is presented. Simulating variations of the load resistance R_L would establish a definitive foundation for assertively selecting the topology that perfectly aligns with the requirements of the WPT system.

4.2 Model Validation for The Class DE Inverter with A Series Resonant Tank

For the development of the project, for the purposes of calculating passive components, the operation of the inverter has been considered within the range where the duty cycle *D is* 0.25, which is established as the optimum operating point for the DE class inverter [97]. In other words, the switches are turned on for 1/4 of the switching period, which allows for accurately determining the elements that comprise the class DE series resonant inverter from (3.3)-(3.6) as described in Table 4.1.

Table 4.1: parameters of the class DE resonant inverter with series resonant tank.

Parameter	Value
Input Voltage	V_i=350 V
Output Power	P_o=2000 W
Quality Factor	Q_{DE}=20
Switching Frequency	f_o=1 MHz
RMS output voltage	$V_{o,rms}$ = 120 V
Output peak voltage	$V_{o,peak}$ = 169.70 V
Load Resistance	R_L=3.1 Ω
Resonant Inductor	L_{res}=9.88 µH
Resonant Capacitor	C_{res}=2.78 nF
Shunt Capacitors	C_{Q1}= C_{Q2}=8.16 nF

A switching frequency of 1 MHz has been established, following previous studies and recommendations from the SAE. Additionally, the input voltage is set at 350 Vdc to ensure the desired RMS output voltage levels, specifically $V_{o,rms}$ = 120.00 V. Lastly, a Q_{DE} parameter of 20 is utilized to improve the rejection of harmonic content within the LLC resonant tank..

As previously discussed, a key factor in assessing the proposed resonant inverter control circuit's efficiency is analyzing it in the frequency domain. Figure 4.1 illustrates the models for small signals, along with their corresponding resonant inverters within a frequency range of 100

Hz to 450 MHz. It is worth noting that the small signal model is applicable up to half of the selected switching frequency. This analysis was conducted using the AC-Sweep tool in PSIM®. Upon analyzing the amplitude and phase Bode diagrams derived from the modeling, it has been determined that the transfer function inferred for the DE class resonant inverter with a series resonant tank is a valid representation of the inverter within the frequency spectrum analyzed. This holds true for the inverter's operation at the point corresponding to the duty ratio D=0.25.

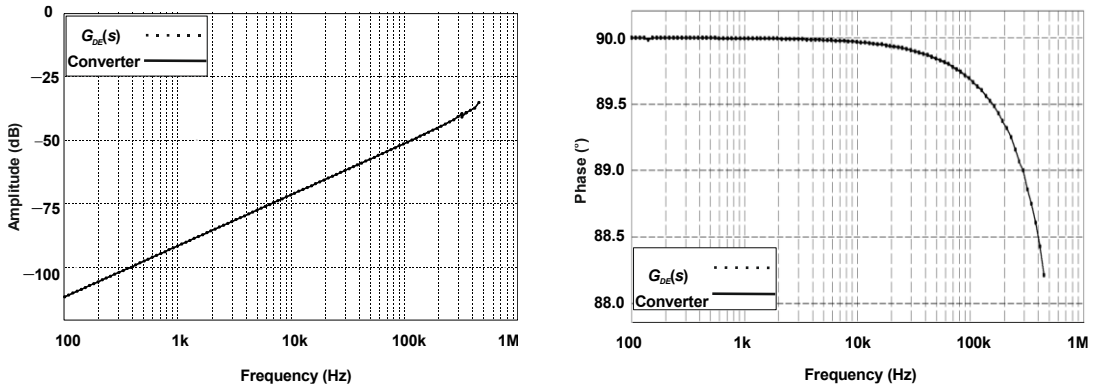

Figure 4.1: Bode plots of the class DE series inverter and its respective transfer function GDE(s): (a) magnitude and (b) phase.

The literature review highlighted several factors to consider, including maintaining a regulated voltage at the load and ensuring a reliable sine wave signal within established standards. To test the effectiveness of the proposed ADALINE-based ARX controller, a load step was applied at time t=0.3 ms, causing the load variation to go from 3.6 Ω to 2.6 Ω, Figure 4.2 depicts the behavior from output voltage under load stepdown. During system start-up, an overvoltage of 189.88 V was observed, and a maximum voltage of 172.76 V was noted during load value changes. It is also important to pay attention to the wave's accommodation time, which depends on the duty cycle and soft-switching characteristic of the active switches. The accommodation time for start-up is 0.04 ms, and after the load variation at 0.3 ms, it is equal to 60 µs.

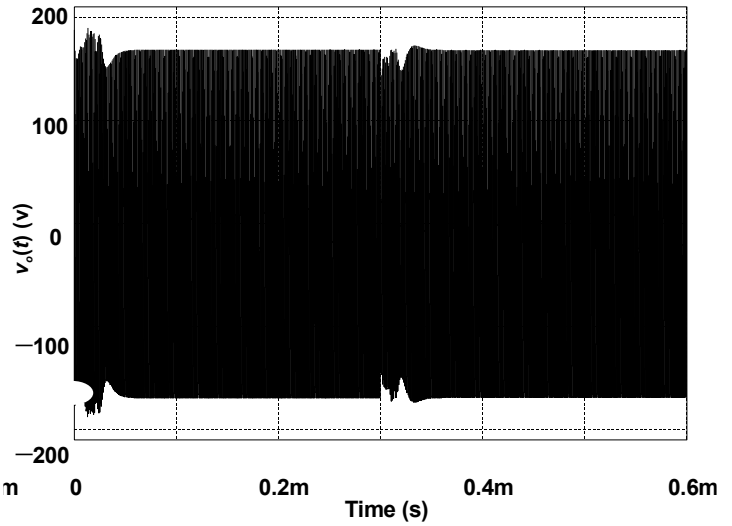

Figure 4.2: Behavior of the class DE series inverter output voltage under load steps.

Figure 4.3 displays the output voltage steady-state behavior after the load step-down. The duty cycle period is equal to 1.022 µs, corresponding to a frequency of 0.9784 MHz, resulting in

a deviation of 1.79% from the resonance frequency. The peak voltage for the analyzed signal is 168.65 V, deviating 0.6% from the expected value $V_{o,peak}$ = 169.70 V.

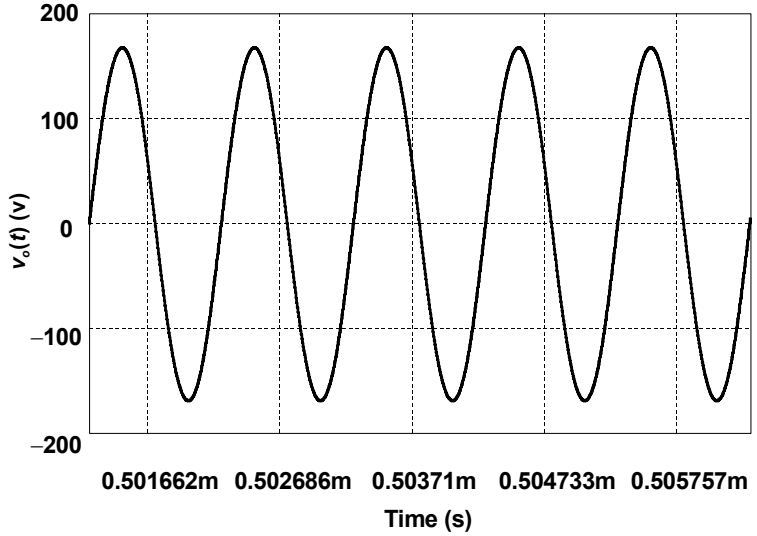

Figure 4.3: Detailed view of the load voltage in steady state from class DE series resonant inverter.

Efficient WPT systems rely heavily on the proper regulation of RMS voltage on the load, as it impacts the voltage and current stresses on the active elements of the topology. In Figure 4.4, the behavior of the RMS voltage on the load for the class DE series resonant inverter under load resistance perturbations is displayed. Theoretically, this should maintain a constant 120 V RMS. However, the proposed controller response shows oscillations between 103 V and 132.41 V under perturbations, ultimately reaching the desired value in a quick accommodation time of no more than 0.04 ms, for booth, startup and load variations.

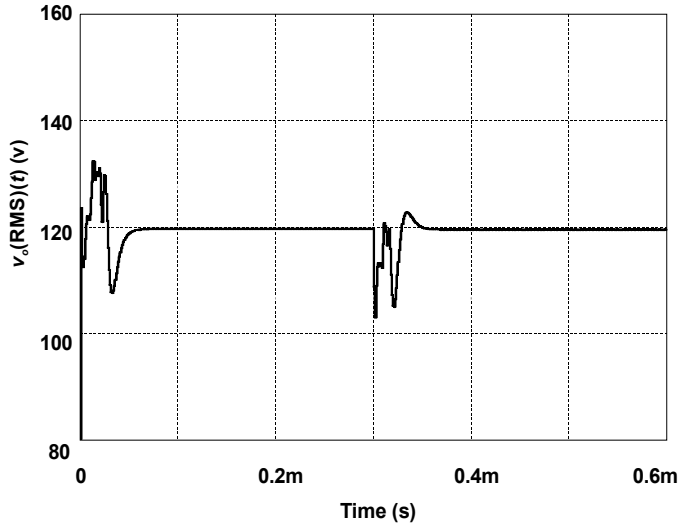

Figure 4.4: Behavior of the RMS output voltage from class DE series resonant inverter.

By incorporating a soft switching feature for switches Q_1 and Q_2 in Figure 3.1, the risk of damaging the controlled semiconductor elements and negatively impacting the power efficiency of the system is significantly reduced. This feature only allows for switches activation when their drain current and drain-source voltage are at zero, preventing any current or voltage spikes. The implementation of a neural network controller topology proposed optimizes the selection process

of the appropriate duty cycle value based on system requirements, resulting in optimal tuning and achieving ZVS and ZCS conditions. Ultimately, the total efficiency achieved for the class DE series resonant inverter is 17.54%; however, it is worth noting that this theoretical value does not account for the physical characteristics of the elements that comprise the system, assuming them to be ideal. Figure 4.5 shows the soft switching reaching for current and voltage for the series resonant inverter with the ADALINE-based ARX controller.

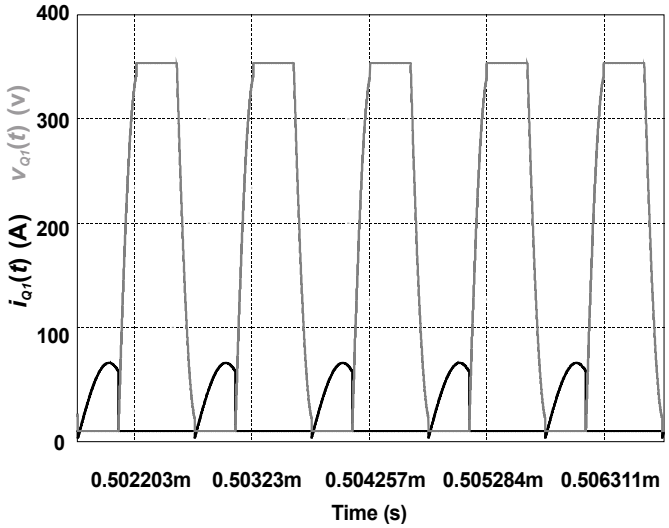

Figure 4.5: Behavior of the drain current and drain-source voltage of switch Q_1.

The waveform delivered by the resonant inverter in a WPT system may contain harmonic content that can disrupt the operation of the switches and control circuit. Hence, it is crucial to maintain low harmonic content in the current signal in both the primary and secondary circuits of the magnetic coupling used for power transfer. The author proposes in [98] a mathematical expression depicted in (4.1) for the Total Harmonic Distortion (THD_1) estimation, as percentage for the current waveform passing through the load resistor R_L in a series resonant circuit, where k_i represents the WPT system coupling factor.

$$THD_1 = \sqrt{\frac{0.018k_i^4 Q_{DE}^2 + 1.266 \cdot 0.018k_i^4}{1 - 1.266^2 k_i^4}} \tag{4.1}$$

Figure 4.6 illustrates the THD behavior in the primary circuit of the WPT system across various coupling factors. It is evident that as the Q_{DE} increases, so does the harmonic distortion of the current in the primary circuit, which escalates considerably at higher values of the k_i. In other words, the closer the T_x inductor is to the R_x inductor, the more significantly the distortion amplifies.

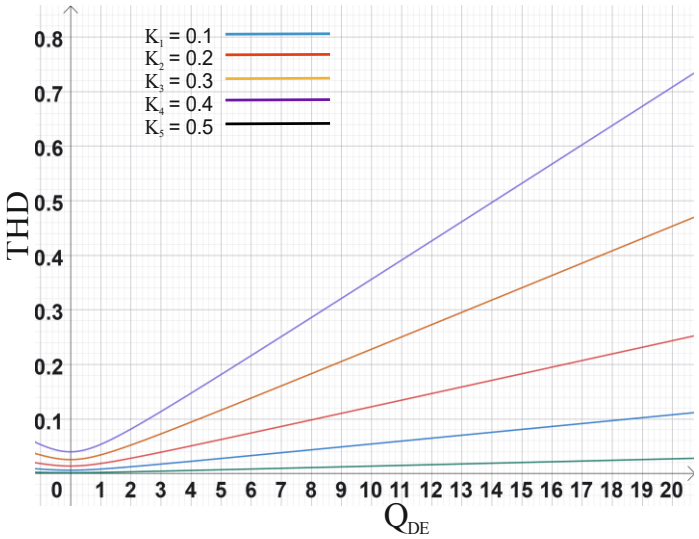

Figure 4.6: THD_I with different coupling factors based on the equation (4.1)

4.3 Model Validation for The Class DE Inverter with A Parallel Resonant Tank

The specifications for the passive elements and voltage and power characteristics of the parallel resonant tank associated with the class DE inverter circuit, as depicted in Figure 3.4a, have been established across the equations described in section 3.3 and are detailed in Table 4.2.

Table 4.2: Parameters of the class DE resonant inverter with parallel resonant tank.

Parameter	Value
Input Voltage	V_I=350 V
Output Power	P_o=2000 W
Quality Factor	Q_P=20
Switching Frequency	f_o=1 MHz
Load Resistance	R_{L_P}=30.625Ω
Resonant Inductor	L_{res_P}=243 nH
Resonant Capacitor	C_{res_P}=95.77 nF
Shunt Capacitors	C_{DE_P}=16.33 nF

Utilizing the ACSWEEP function in the PSIM® software, the response was validated for both the circuit depicted in the Figure 3.4a and its corresponding mathematical model $G_{DE\_P}(s)$, outlined in equation (3.18). Figure 4.7 illustrates the response achieved over a frequency range of 1 kHz to 300 MHz, demonstrating convergence in the responses of the two analyzed models.

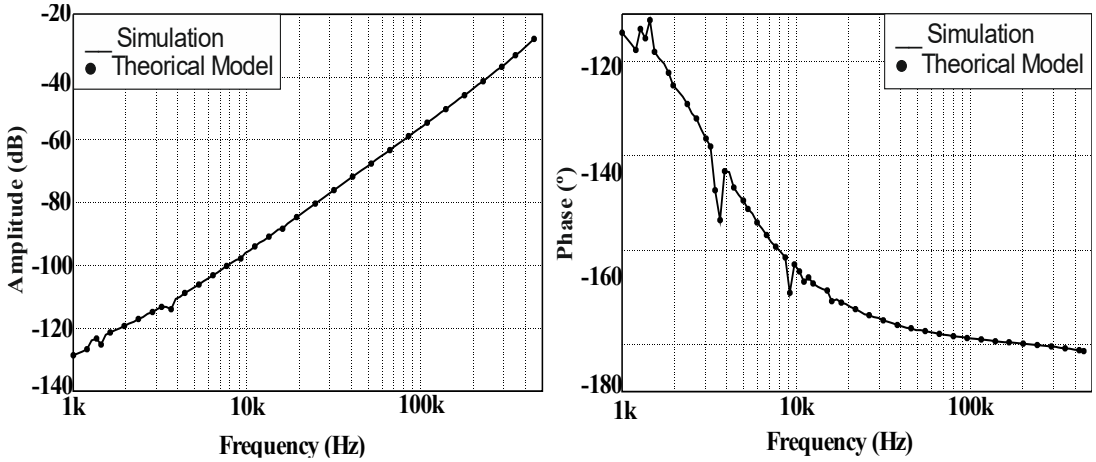

Figure 4.7: Bode plots of the class DE parallel inverter and its respective transfer function G_{DE_P}(s): (a) magnitude and (b) phase.

The class DE inverter, with a resonant parallel tank operated by the ADALINE-based ARX controller, exhibits a response to load variation as depicted in Figure 4.8. The transcendental waveform values include a maximum voltage of 282.50 V and an accommodation time of 20 µs during start-up and 11.79 µs for the interference instant at 1 ms. Notably, the load resistance in this instance oscillates between 11 and 30 ohms, which represents a broader range of variation than observed in the case of the series resonant circuit described in Section 4.2. This feature could prove to be useful since it allows for a broader range of possible values for the variation of R_L resistance, which may occur due to misalignments and decoupling of the WPT magnetic system.

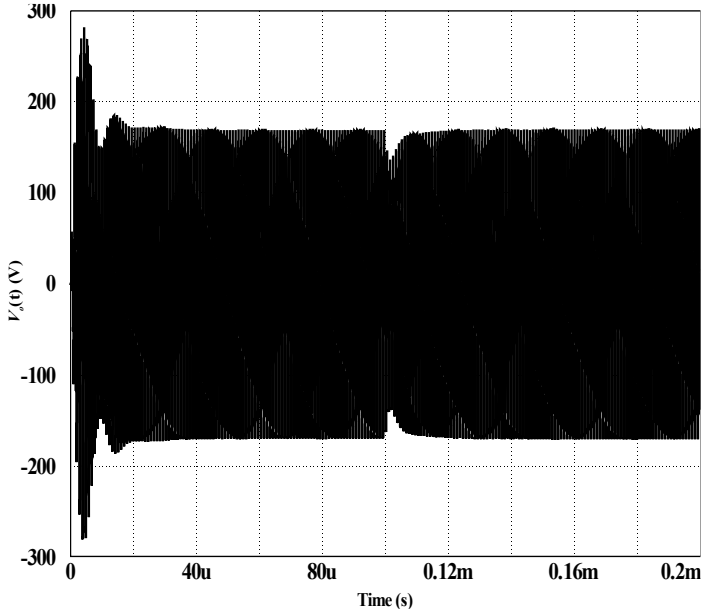

Figure 4.8: Behavior of the class DE parallel inverter output voltage under load steps.

Upon conducting a thorough analysis of the class DE inverter response with a parallel resonant load, it has been observed in Figure 4.9 that the waveform period aligns with 0.9452 µs, related to an oscillation frequency of 1.058 MHz, i.e., 5.79% deviation from the base frequency mentioned in Table 4.2.

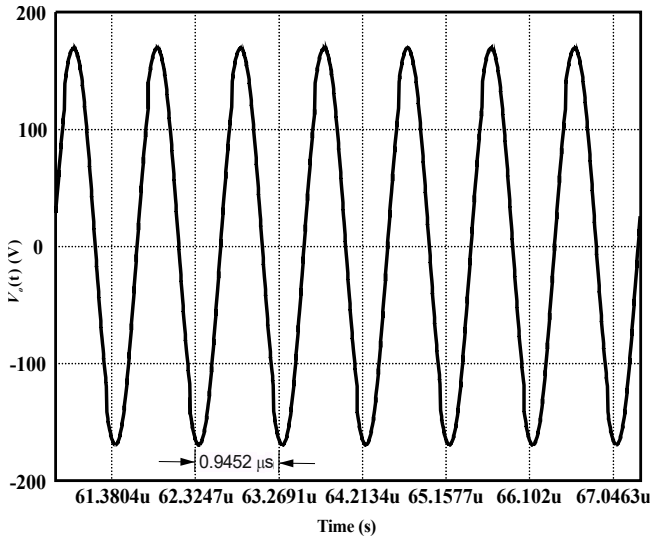

Figure 4.9: Detailed view of the load voltage in steady state from class DE parallel resonant inverter.

Upon evaluating the controller response for the class DE parallel resonant inverter and its RMS voltage delivery to the load, noticeable oscillations are detected. These oscillations directly impact system efficiency by affecting the magnetic coupling between the transmitter and receiver of the WPT link. This is a consequence of not achieving soft switching conditions. This intrinsic characteristic of the parallel system prevents the proposed control strategy from reaching its optimal working point. Nonetheless, the steady-state RMS voltage remains at 119.94 V before any load resistance alterations and at 119.87 V after such modifications are carried out at the 1 ms instant, as shown in Figure 4.10.

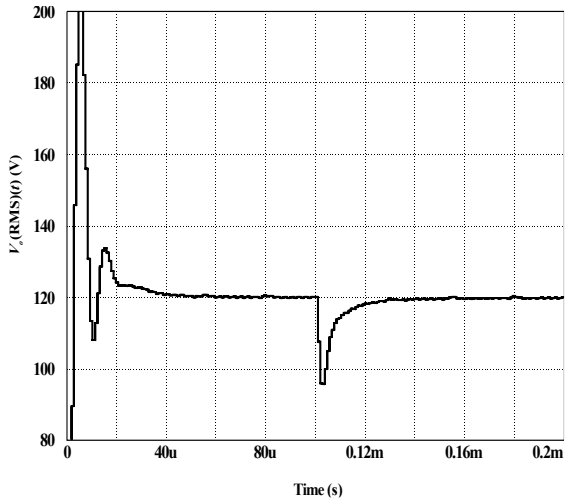

Figure 4.10: Behavior of the RMS output voltage from class DE parallel resonant inverter.

Upon analyzing the behavior of voltage in switch Q_1, it became apparent that the turn-on of the switches occurs when the voltage is not null, as illustrated in Figure 4.11, which presented a problem that the proposed control strategy could not resolve. This issue poses a potential risk of damaging the active element due to the possibility of current levels exceeding the manufacturer's designated values. As previously mentioned, the class DE inverter with a parallel resonant load requires more specialized control to ensure the system's operability, as the switch turn-on coincides with the maximum peak voltage on the load.

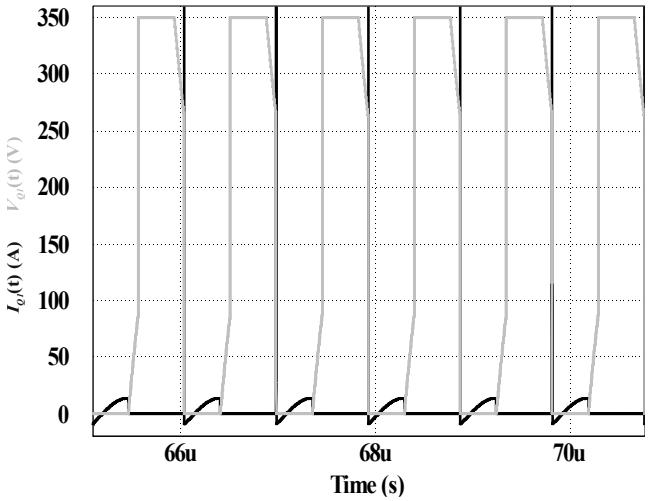

Figure 4.11: Drain current and drain-source voltage of switch Q_1 for class DE parallel resonant inverter.

After conducting simulations, it was determined that the THD of the voltage wave in the load is 8.91%. However, this measure cannot be used to confirm the validity of the magnetic circuit coupling factor calculation k_i, as it falls outside the practical feasible range, according to the author in [98], It is worth noting that an increase in the value of k_i results in a significant rise in the total harmonic distortion in the primary circuit. Further examination is required to obtain analytical results like those in (4.1) for the series resonant circuit. This analysis will establish a correlation between the magnetic coupling coefficient k_i and the THD for the primary of the WPT system with a parallel resonant tank.

4.4 Model Validation for The Class DE Inverter with A Series-Parallel Resonant Tank

In order to carry out the necessary calculations for the class DE inverter with series-parallel resonant load, the equations outlined in (3.25) were used. This allowed us to project the passive elements required for the inverter, which are integral to its operation. The design specifications for the inverter are also presented in Table 4.3 for reference.

Table 4.3: Parameters of the class DE resonant inverter with series-parallel resonant tank.

Parameter	Value
Input Voltage	V_i=350 V
Output Power	P_o=2000 W
Quality Factor	Q_{SP}=4
Switching Frequency	f_o=1 MHz
Load Resistance	R_{L_SP}=8.83Ω
Resonant series Inductor	L_{S_SP}=1.4 µH
Resonant series Capacitor	C_{S_SP}=56 nF
Resonant parallel Capacitor	C_{P_SP}=72 nF
Resonant parallel Inductor	L_{P_SP}=555 nH

The functionality of the class DE inverter with a series-parallel resonant load, has been confirmed through simulation. The transfer function, expressed in equation (3.19), together with the circuit shown in Figure 3.4b were used to generate the Bode diagrams depicted in Figure 4.12, which illustrate the amplitude and phase. It is worth noting that there is a divergence that occurs at frequencies above 100 kHz, which is likely due to the computational cost involved in the process. It is therefore feasible to assert that both the mathematical model and the simulated circuit guarantee the proper operation of the system under evaluation. The analysis of the fourth-order G_{DE_SP} mathematical expression is highly complex due to its main characteristic of having two resonance frequency values, as previously mentioned in section 3.3. It is worth noting that the working point is established based on the higher frequency value, as it closely aligns with the chosen switching frequency f_o for the class DE resonant inverter.

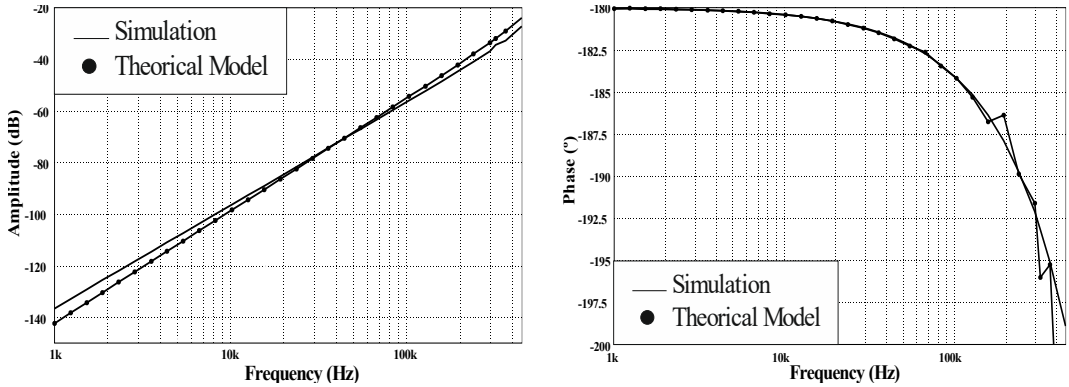

Figure 4.12: Bode plots of the class DE series-parallel inverter and its respective transfer function $G_{DE\_SP}(s)$: (a) magnitude and (b) phase.

Figure 4.13, displays the response of the class DE series-parallel resonant inverter under load resistance variations. At load step-up, the maximum voltage achieved is 227.58 V with an accommodation time equal to 8.01 µs. During the start-up, an accommodation time of 7.50 µs is observed. This resonant inverter offers a range of values for R_L between 5 Ω and 120 Ω, which is significantly greater than what was previously expressed for the topologies studied.

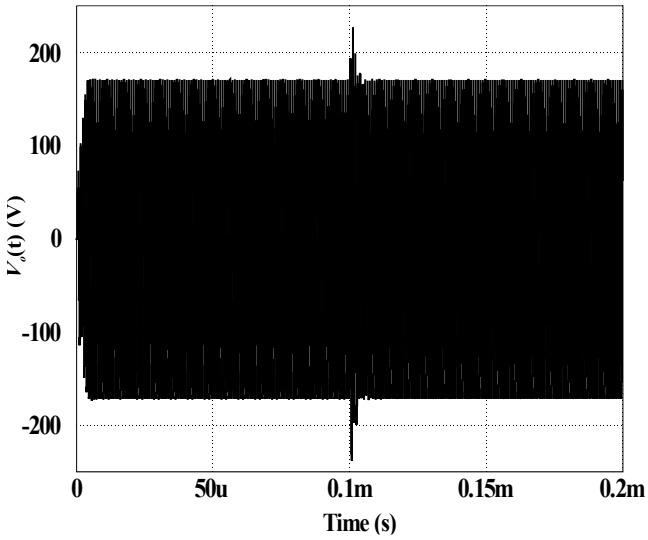

Figure 4.13: Class DE series-parallel inverter output voltage under load variation.

According to the data presented in Figure 4.14, the output voltage exhibits a period of 0.88 us, indicating a switching frequency of 1.13 MHz. This implies that a 13% frequency shift from f_o, this one, was considered during the computation of class DE series-parallel resonant inverter. The peak voltage of $v_o(t)$ is equal to 170.45 V.

To characterize the harmonic content present in the output voltage waveform $v_o(t)$, the THD analysis tool available in the PSIM® software environment was employed. The analysis was conducted at an oscillation frequency of 1.1375 MHz. The resulting THD value for the sine wave, depicted in Figure 4.14, was 2.31%. The THD analysis provides valuable insights into the distortion of the voltage waveform, aiding in the optimization of inductor design. Developing a mathematical expression to establish the relationship between K_i and THD for the inductor in a

series-parallel resonant circuit is essential, similar to what is depicted in the equation (4.1) for the series-resonant load case.

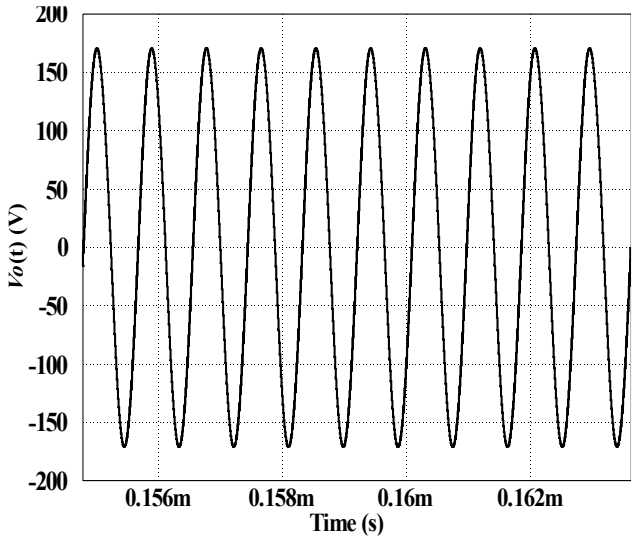

Figure 4.14: Detailed view of the load voltage in steady state from class DE series-parallel resonant inverter.

After conducting an analysis of the RMS voltage that was supplied to the load as depicted in Figure 4.15, it was observed that the maximum point was equal to 164.83 V. This peak voltage occurred precisely when the load step was initiated, and it took only 23 μs for the system to adjust and stabilize. This fast response time under unstable conditions was made possible by the ADALINE-Based ARX controller, which proved to be an efficient and reliable means of adapting to the series-parallel resonant load. Moreover, it is worth noting that no voltage peaks were observed at the starting point, which is a significant advantage in terms of reducing semiconductor stress. Finally, the RMS voltage supplied to the load stabilized at level of around 120.64 V, indicating that the system operates smoothly and efficiently.

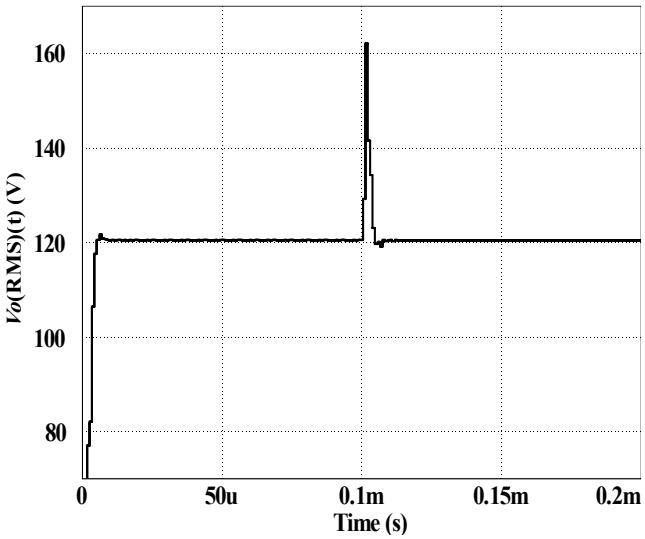

Figure 4.15: The RMS output voltage from class DE series-parallel resonant inverter under load step.

When analyzing resonant inverters, it is important to consider the soft-switching characteristics, specifically ZVS and ZVDS, as illustrated in Figure 4.16. The turn-on switch Q_1

enables current conduction during the positive half-cycle when the drain-source voltage is zero. During the negative half-cycle, current conduction is a result of the antiparallel diode. It is noteworthy that the maximum drain current is 43.79 A, while the minimum is equal to -39.12 A.

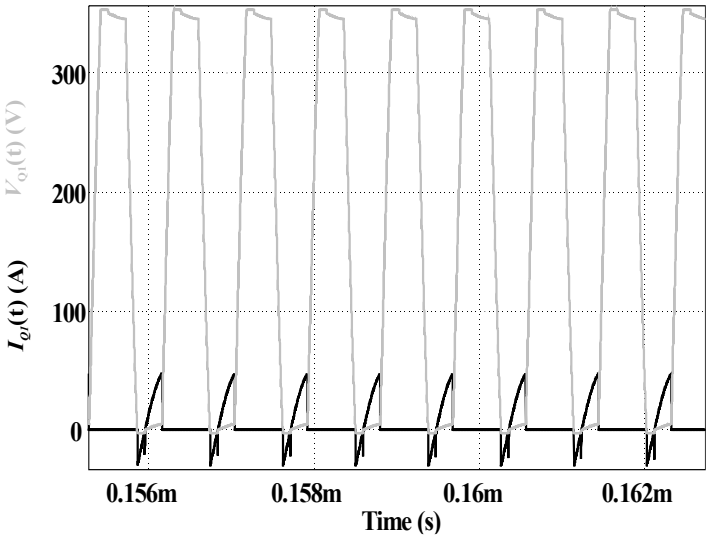

Figure 4.16: Drain current and drain-source voltage of switch Q_1 for class DE series-parallel resonant inverter.

4.5 Final Considerations

This chapter presented the validation of the transfer functions obtained for the class DE inverter with series, parallel, and series-parallel resonant loads. For this purpose, the mathematical expressions previously obtained were compared with the curves generated through simulations using the PSIM software.

A succinct analysis of the response of the ADALINE-based ARX controller proposed for each of the topologies was also presented. The voltage waveforms in the load were studied under variations in both the resistance of R_L and the continuous supply voltage source V_i. Additionally, the soft switching operation of switches Q_1 and Q_2 was verified using the current and voltage waveforms in the switches.

A final consideration regarding THD was also carried out as part of the analysis in this chapter, validating the disturbances present in the load voltage waveform.

The analysis of the results obtained allows to verify the use of the control system designed and its efficiency for each of the topologies under analysis. It was also possible to show that the mathematical models obtained for the different types of load configurations are capable of faithfully representing their behavior for a frequency range that goes from 1 kHz to 450 kHz. Thus, it is reasonable to assume that these expressions are valid for the design stage of the ADALINE neural network-based controller.

CHAPTER V

PRACTICAL WPT PROTOTYPE DESIGN

5.1 Preliminary Considerations

To validate the transfer function of each resonant inverter and the proposed ADALINE-based ARX controller, it is crucial to conduct practical verification of the methodology. However, this chapter will concentrate solely on the design topology of the Class DE inverter with a series resonant load, along with the proposed control strategy.

The prototype output power has been established to 50 W with a source voltage of 50 Vdc, thereby adhering to the specifications outlined in the Metal-Oxide-Semiconductor Field-Effect Transistor (MOSFET) and driver data sheets. Some topologies were engineered to sample the voltage and current from the flat inductor at the core of the primary WPT, which are influenced by the separation distance in the magnetic circuit. Amplification and signal conditioning stages are provided, along with zero-crossing detection for each waveform as previously described. Then, an ADALINE-based ARX neural network running on an ESP32 microcontroller calculates the appropriate duty cycle for switching the class DE half-bridge inverter MOSFETs based on the sensed signals. Therefore, the inverter operates in soft-switching mode, with activation pulses precisely aligned with both ZVS and ZCS points.

Selecting suitable components for analog signal treatment is crucial to maintaining operation at a resonance frequency of approximately 1 MHz; special emphasis is placed on choosing ferrite cores for the inductors discussed in this chapter. Additionally, electronic circuit boards have been carefully designed in accordance with the manufacturer's guidelines to minimize the electromagnetic interference generated by high-frequency switching.

The criteria for selecting components and topologies for each stage: amplification, zero-crossing detection, and signal division are described. The chapter also explains how signals are conditioned to conform to the ESP32's allowable input ranges and details the design of coupling filters to both decouple incoming control signals and handle duty-cycle signals generated by the microcontroller.

5.2 Class DE Resonant Inverter Power Stage

GaN power devices have garnered significant attention as a promising alternative to traditional silicon (Si) and silicon carbide (SiC) technologies in power electronics. Compared with Si-based devices, GaN transistors offer notably higher switching frequencies and lower switching losses, leading to improved efficiency and higher power density [99]. While Si technology remains cost-effective and well-established, its performance becomes limited in high-frequency operations.

In contrast to SiC devices, GaN technology offers quicker switching characteristics and is better suited for low- to medium-voltage applications. On the other hand, SiC devices boast superior voltage blocking capability and thermal resilience for high-power systems. Consequently, GaN devices present distinct advantages in applications where compactness and efficiency are essential, such as in wireless power transfer systems and high-frequency power converters [100].

The GS61008P MOSFET from Infineon [101] was selected for the Class DE half-bridge with LLC series resonant inverter as shown in Figure 5.1, owing to several key attributes: its capability to operate at frequencies up to 10 MHz, an output capacitance of 250 pF, minimal drain-to-source ON resistance, and a straightforward gate driver (0 V for off, 6 V for on). These features render it highly suitable for the project's criteria. Furthermore, the GS61008P exhibits ultra-low switching losses owing to its low gate charge ($Q_g \approx 5$ nC) and reduced output capacitance (Q_{oss}). This characteristic is particularly critical at 1 MHz, where switching losses typically dominate the efficiency of Class DE topologies. By minimizing transition related energy dissipation, the device enables inverter efficiencies above 90%, which is essential in WPT systems where thermal constraints are stringent.

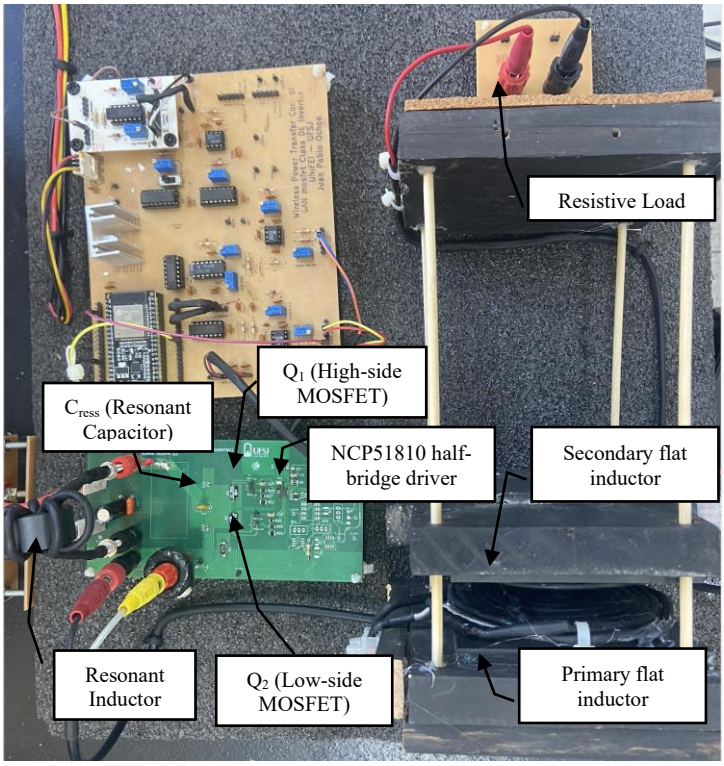

Figure 5.1: Class DE Inverter power electronic board with series resonant circuit

The power stage of the class DE resonant inverter consists of a tank circuit comprising an inductor and a capacitor. This stage is powered by a regulated DC source delivering 50 Vdc and 4 Adc. According to the foregoing theory, the inductor used in the resonant circuit, assembled on a toroidal core with an average diameter of 7.5 cm and composed of 130 parallel 33-gauge Litz

wires, requires six turns to achieve an inductance of 60 μH. When combined with a 390 pF ceramic capacitor, the circuit functions at a specified frequency of 1 MHz. Table 5.1 outlines the specifications of each component comprising the power stage of the prototype developed for the class DE resonant inverter.

Table 5.1: Parameters of the class DE resonant inverter prototype with series resonant tank

Parameter	Value
Input Voltage	V_i=50 V
Output Power	P_o=50 W
Quality Factor	Q_{DE}=20
Switching Frequency	f_o=1 MHz
Load Resistance	R_L=3.9Ω
Resonant Inductor	L_{res}=70 μH
Resonant Capacitor	C_{res}=390 pF
Shunt Capacitors	C_{Q1}= C_{Q2}=8.16 nF

The total inductance required for the resonant tank circuit is 70 μH. Given that the toroidal core inductor provides 60 μH, it was concluded that the flat inductor for the primary WPT should be approximately 10 μH. Thus, two planar inductors depicted in Figure 5.2 were designed and mounted on two different square ferrite cores (KEMET model FPL100/100/6-BH1T), which have a relative permeability of approximately 3000 ± 25% at 1 MHz. Utilizing the same Litz wire as the toroidal coil, the planar inductors, consisting of 14 concentric turns, yielded a measured value of 13 μH.

In this study, the secondary side of the WPT system is implemented with a simplified configuration to isolate and analyze the intrinsic power-transfer characteristics of magnetic coupling. The secondary circuit features a flat spiral inductor directly connected to a purely resistive load, omitting active power conditioning stages or rectification circuitry.

Employing a resistive load enables a controlled, repeatable evaluation of system performance by eliminating the nonlinear effects associated with power electronic converters and energy storage components. This configuration ensures that the measured secondary-side voltage, current, and power are determined exclusively by the magnetic coupling, resonant behavior, and operating frequency of the WPT system. Thus, any variations in power transfer efficiency can be directly linked to changes in coupling conditions, such as coil separation and alignment.

Furthermore, the flat spiral inductor used on the secondary side is designed to match the resonant characteristics of the primary circuit, maximizing power transfer under nominal operating conditions. By connecting a resistive load directly to the secondary inductor, the experimental setup serves as a clear and meaningful benchmark for comparing open-loop and closed-loop control strategies and for validating the effectiveness of the proposed control approach under varying operating conditions.

The KEMET ferrite [102] tile is exceptionally well-suited for WPT systems, thanks to its optimized magnetic, thermal, and structural properties tailored for high-frequency energy transmission. Designed explicitly for WPT applications, the FPL series supports operating

frequencies of up to 1 MHz, facilitating efficient magnetic coupling between transmitter and receiver coils in resonant inductive power links. The ferrite material boasts a high initial permeability and is guaranteed to minimize magnetic losses, enabling practical flux guidance while reducing core heating and hysteresis losses.

With dimensions of 100 × 100 × 6 mm, the core provides a generous cross-sectional area for magnetic flux concentration and serves as a robust magnetic shield. This configuration confines the magnetic field within the coupling region, thereby minimizing electromagnetic leakage and enhancing overall system efficiency by reducing eddy-current losses in adjacent conductive structures. Coupled flat inductors were built for the primary and secondary WPT systems, as shown in Figure 5.2.

Figure 5.2: WPT Flat Concentric Inductor

Integrated into the circuit, the 74HC126 device provides essential voltage buffering and isolation for the ESP32 control unit, enhancing overall system stability. It plays a key role in both the reference signal collection stage (involving current and voltage sensors) and the interfacing between the microcontroller and the MOSFET driver.

With the resonant LLC circuit established, which connects directly to the intermediate point of the class DE inverter and includes the toroidal inductor, flat inductor, and ceramic capacitor, the next step is to determine the controller responsible for turning on the switches Q_1 and Q_2. In a conventional half-bridge inverter configuration, the upper MOSFET does not use ground as its reference point. To resolve this issue, the circuit incorporates a driver that creates a virtual ground for the reference point of the semiconductor device. For this purpose, the NCP51810 high-speed half-bridge driver from ON Semiconductor [103] has been selected due to its compatibility with Gallium Nitride (GaN) power switches. This driver features two internally regulated supply voltages: V_{DDL}, which supports the low side and is referenced to power ground (*PGND*), and V_{DDH}, which serves the high side and is referenced to the SW pin. Both outputs are designed exclusively for output and should not be connected to external voltage sources; their operating range is -0.3

to 5.5 Vdc. Additionally, the driver offers fast transient response, with an output fall time of 1.5 ns and an output rise time of 2 ns, thereby enabling high-frequency operation. Importantly, there is no magnetic isolation between the PWM signal on the NCP51810 and its power-gate control signals, allowing direct interconnection between the power and control circuit reference points. A graphical representation of the controller's configuration is provided in Figure 5.3.

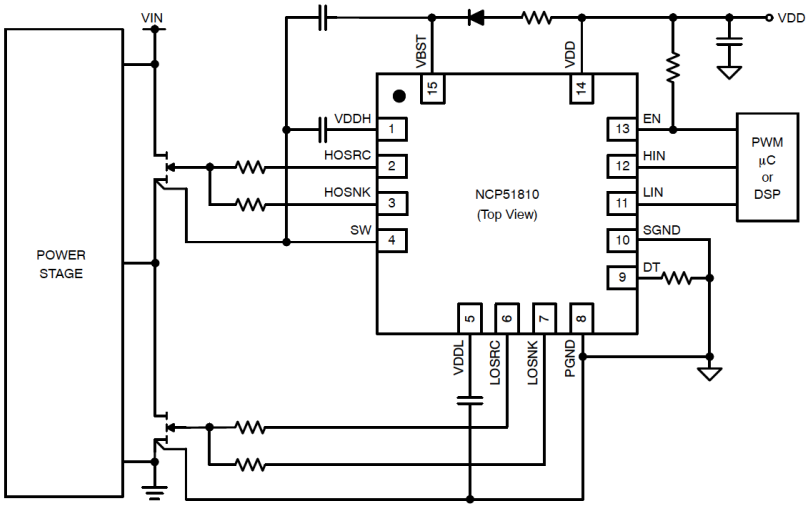

Figure 5.3: Typical Application Schematic. Source: [103]

5.3 Controller Stage Board configuration

Figure 5.4 presents the complete architecture for signal acquisition and conditioning designed for synchronized voltage and current measurements in the proposed WPT system. The setup features two parallel, functionally identical signal paths. One dedicated to current sensing and the other to voltage sensing, ensuring uniform phase and timing characteristics across both measurements.

Within each signal path, the measured quantity is first captured by an appropriate sensor and then directed to an amplification stage using the LM318 operational amplifier [104], chosen for its high slew rate and wide bandwidth, both critical for accurately processing the high-frequency sinusoidal waveforms typically encountered in WPT systems. This amplification stage scales the sensor output to an appropriate voltage level while maintaining waveform integrity and minimizing phase distortion. Additionally, adjustable resistor networks powered by ±10 V supplies facilitate offset control, centering the amplified signal around the reference level needed for reliable zero-crossing detection.

The amplified signal is processed by a zero-crossing detection stage implemented with the LM319 high-speed comparator [105], which was selected for its rapid response time and minimal propagation delay, which facilitates accurate detection of zero-crossing instances, even at elevated operating frequencies.

Following the comparator stage, the digital output is routed through a 74126 tri-state buffer for signal conditioning. This component provides electrical isolation between the analog and digital domains, ensures compatibility with logic-level requirements, and enhances noise immunity by delivering clean and well-defined digital transitions. Additionally, the buffer protects downstream digital circuitry from potential voltage spikes or transient disturbances originating from the analog front end.

The conditioned digital signals are then interfaced with the ESP32-S3 microcontroller via the 40HS17. The ESP32-S3 is responsible for time-domain processing, synchronization analysis, and the execution of higher-level control algorithms. By converting the original analog voltage and current waveforms into accurately timed digital events, this architecture enables reliable phase measurement and real-time monitoring of WPT system performance.

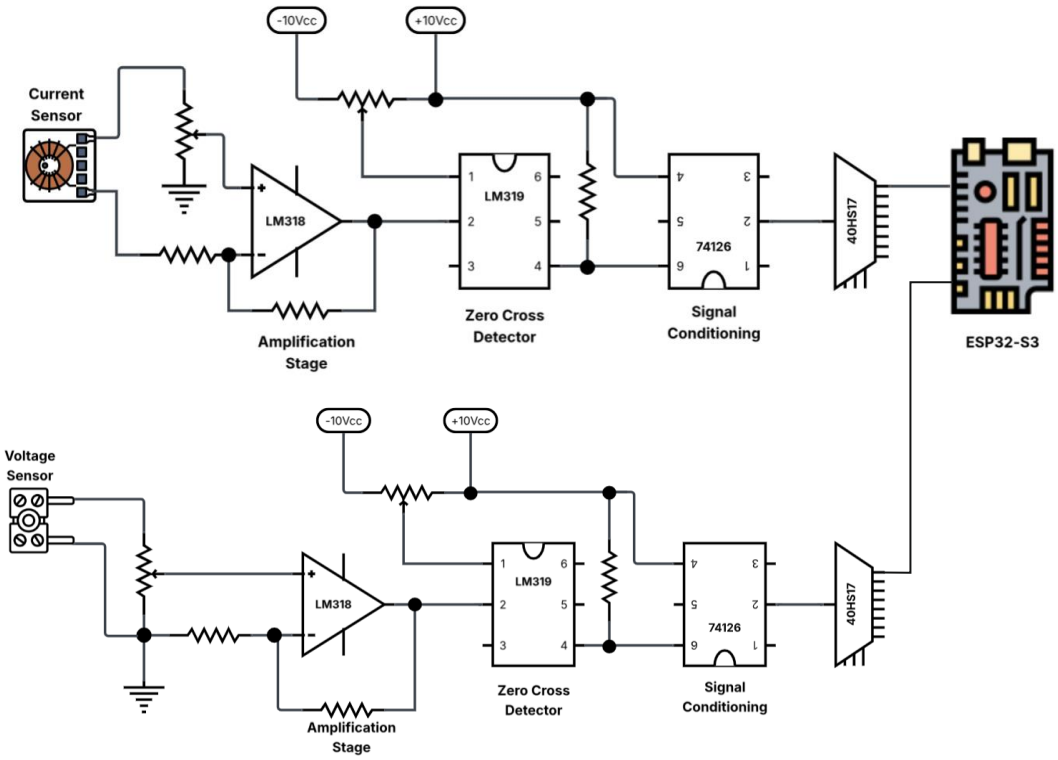

Figure 5.4: Control Stage block configuration

The toroidal current sensor, designed with 8 turns of 28 AWG wire, features a passband extending into the megahertz range. Due to the limited number of turns and the resulting low parasitic capacitance, the sensor demonstrates sufficient bandwidth to operate at 1 MHz, allowing for precise high-frequency current measurement essential for wireless power transfer applications. The upper cutoff frequency is primarily limited by parasitic elements and core losses, estimated at 1–2 MHz, which aligns well with the operating frequency of the proposed system.

Figure 5.5 provides a comprehensive overview of the key components that constitute the controller's board. This assembly not only houses the essential connection terminals but also

incorporates line filters to eliminate electrical noise and signal conditioning circuits to ensure optimal signal quality. Additionally, it features a reliable 5-volt voltage regulator, which plays a crucial role in maintaining a stable power supply to the internal circuits, alongside several other components that work together to enhance the controller's performance.

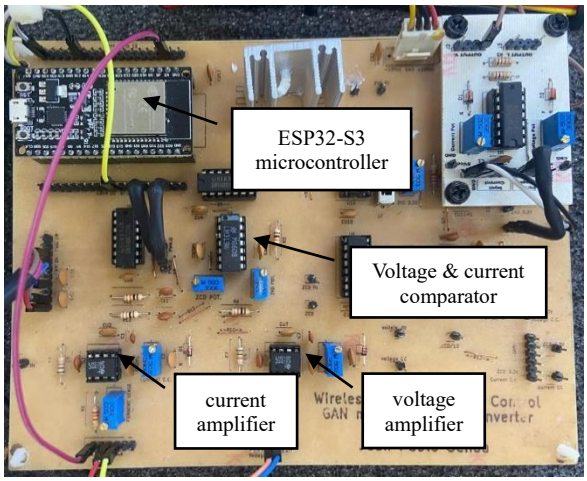

Figure 5.5: ADALINE-based ARX control board

The input amplifier circuit for voltage and current sampling is depicted in Figure 5.6. It has been designed according to the manufacturer's specifications and employs a configuration known in the literature as Feedforward Compensation, which enhances the inverting slew rate. This setup ensures optimal performance at the resonant circuit's operating frequency. By utilizing feedforward compensation in the LM318 chip, slow internal stages are bypassed, resulting in a significant increase in the inverting slew rate. This allows the device to manage large signal swings at 1 MHz without distortion, an accomplishment unattainable with older, Miller-compensated designs [106].

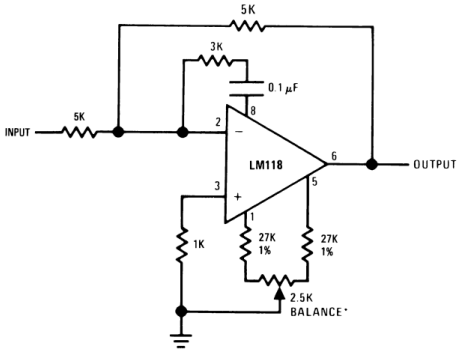

Figure 5.6: Feedforward Compensation for Greater Inverting Slew Rate. Source: [106]

The comparator circuit is designed to accurately detect the precise moments when the sample signal, whether in current or voltage form, crosses the zero point. This functionality generates a square wave signal that fluctuates between 0 and 10 volts at the identified crossing moments. The LM319 component is utilized to achieve this, meeting the essential specifications for reliable operation, including the necessary operating frequency and voltage levels. The LM319 boasts several advantages [107], including a speed of approximately 80 ns, flexible open-collector

outputs, a high drive capability of 25 mA, a wide supply range, robust inputs with protection diodes, and a long-standing track record of reliability. These features make it particularly well-suited for applications such as 1 MHz zero-crossing detectors and other high-speed comparator functions, while remaining cost-effective and easy to integrate.

The electronics integrated into the proposed controller not only ensure the system functions as intended but also prioritize minimizing interference, particularly electromagnetic interference arising from the high operating frequency. While it may not be a conventional analog filter, the 74HC126 provides significant advantages for digital signal conditioning when interfaced with microcontrollers such as the ESP32. Serving as a quad buffer and line driver with three-state outputs, it fulfills multiple roles that enhance signal integrity, protect input stages, and improve noise immunity.

One of the key advantages of the 74HC126 is its buffering capability. By electrically isolating the signal source from the ESP32's general-purpose input/output (GPIO) pins, it prevents loading effects, ensuring the microcontroller receives a stable, well-defined logic signal rather than a degraded or noisy waveform. Furthermore, when powered at 3.3 V, the 74HC126 limits its outputs to levels compatible with the ESP32's voltage specifications, offering protection against overvoltage and ensuring compliance with the device's logic-level requirements.

5.4 ADALINE-based ARX Design

The ADALINE-based ARX controller network, implemented on the ESP32 platform [108], represents a streamlined realization of an adaptive linear predictive model tailored for embedded control and signal estimation applications. This implementation seamlessly integrates analog input acquisition, data preprocessing, ADALINE-based ARX prediction, and real-time pulse-width modulation (PWM) output generation. This method effectively combines system identification, adaptive filtering, and digital signal control within a microcontroller-based environment.

Given the high operating frequency of the proposed system (1 MHz), the ESP32 microcontroller is not suitable for directly sampling the instantaneous current and voltage waveforms. The internal analog-to-digital converter (ADC) of the ESP32 does not possess the necessary sampling rate and bandwidth for complete waveform acquisition at this frequency. Therefore, an alternative measurement strategy has been implemented that relies on high-speed analog preprocessing and time-domain feature extraction.

The current and voltage signals are initially captured using specialized sensing circuits. Current measurement is accomplished with a toroidal current transformer, while voltage sensing relies on a resistive network. These analog signals are then amplified through high-bandwidth operational amplifiers and transformed into digital timing signals using high-speed comparators

configured as zero-crossing detectors. Consequently, the ESP32 receives digital pulse signals that encode the timing information of the original waveforms, rather than their instantaneous amplitudes.

The ESP32 processes the comparator outputs by capturing signal-transition timing using its internal hardware timers and interrupt mechanisms. As a result, the effective measurement resolution is determined by the timer clock frequency rather than the ADC sampling rate. With internal timers operating in the tens of megahertz range, the system achieves a timing resolution on the order of tens of nanoseconds, which is adequate for resolving phase differences at an operating frequency of 1 MHz, corresponding to a signal period of 1 μs.

The estimation of current and voltage characteristics is conducted using the ADALINE algorithm. Rather than working directly with raw waveform samples, the ADALINE model analyzes derived temporal features, such as the phase relationship between voltage and current, and the known gain of the analog front-end circuitry. Assuming quasi-sinusoidal steady-state operation, the fundamental components of the signals can be estimated with sufficient accuracy for control and performance evaluation.

This feature-based estimation significantly reduces computational complexity and enables real-time operation on a resource-constrained embedded platform.

This approach allows accurate estimation of phase and frequency information while avoiding the need for high-speed analog sampling. This averaging method serves as a low-pass filter, thereby increasing resilience against transient disturbances and quantization effects. Additionally, the system calculates a ratio between the two input signals, introducing a nonlinear dynamic element into the predictive process.

Once the average ratio input is obtained, it is processed using a simplified ARX model, with parameters derived from a dataset of experimentally collected input-output pairs. This dataset defines the system's dynamic behavior, enabling the ADALINE structure to adaptively estimate the next output value based on recent input and output information. The predicted value is normalized and used to modulate the duty cycles of two PWM signals generated by the MCPWM peripheral on the ESP32. These PWM signals operate at the resonant frequency and maintain a 180° phase shift, with outputs on GPIO12 and GPIO13. The duty cycle varies continuously between 25% and 45%, reflecting the predicted output and effectively encoding the network's response into a high-speed, hardware-synchronized output waveform.

The controller obtained from the learning process of the ADALINE-based ARX neural network achieved a minimum error, as determined by the Akaike Information Criterion (AIC) [109], to establish the regression that best fits the system, yielding a minimal convergence value.

Figure 5.7 shows the results obtained in terms of the expected values compared with the ones provided by the parameter estimation network, resulting in a negligible error.

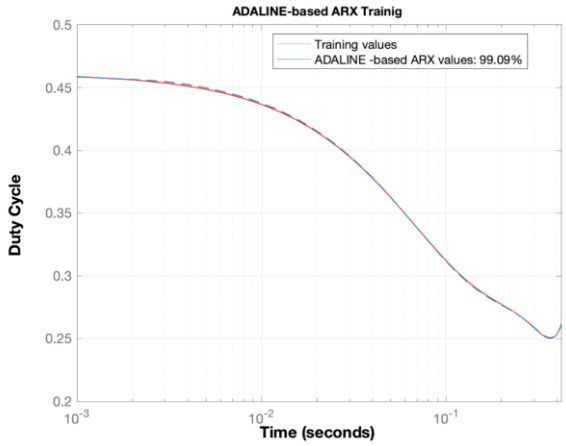

Figure 5.7: ADALINE-based ARX fitting process

The AIC determines the regression that best fits the ARX parameter estimation system by minimizing a cost function that both penalizes high residual errors and excessive model complexity. This guarantees that the selected regression strikes an optimal balance between accuracy and generalization in the ADALINE-based ARX estimator. Therefore, the transfer function for the controller that best suits the system requirements is the one presented in (4.2).

$$H(s) = \frac{-0.004175 \cdot s + 8.331}{s^2 + 12.78 \cdot s + 10.44} \tag{4.2}$$

Computational architecture is strategically distributed across the ESP32's dual cores to enhance real-time performance. The PWM generation task is assigned to Core 1, ensuring a stable and deterministic waveform output. At the same time, Core 0 handles analog sampling and prediction, including signal acquisition, filtering, and model evaluation. This division effectively minimizes timing interference between the high-frequency PWM updates and the slower analog input processing.

Overall, the implementation demonstrates the feasibility of embedding an adaptive predictive network, such as the ADALINE-based ARX, within a low-cost microcontroller. It establishes a framework for real-time signal estimation, adaptive control, and learning-based regulation in compact systems, making it well-suited for applications specific to power electronics and WPT. Evaluation of WPT Prototype Outcomes

To ensure the reliability of the proposed ADALINE-based ARX controller, several phases of analysis and validation are essential. This involves observing the behavior of the WPT system in both the frequency and time domains, accounting for variations in the distance between the primary and secondary inductors, ranging from 0 cm to 10 cm. These variations will affect the

duty cycles of switches Q_1 and Q_2. The timing of the PWM signals generated must align with the transfer function presented in Chapter 3, achieving a maximum duty cycle of 45%.

In the next section, graphs depicting voltage, current, and available power on the primary flat inductor are presented, demonstrating the validation of WPT under both the controller's action and open-loop operation. A similar analysis is conducted for the waveforms observed in the secondary flat inductor, enabling the assessment of the WPT system's efficiency under different operating modes of the magnetic circuit.

Some analysis that provides a thorough examination of the operational characteristics of the Class DE inverter circuit, specifically under soft-switching conditions, are evaluated. The studies offer insights into critical parameters, including the inverter's operating frequency and the delays observed between the current and voltage waveforms in the resonant circuit. Additionally, it is necessary to evaluate the intrinsic response times of essential components and stages in the system, such as the driver and the zero-crossing detection circuit. These response times directly affect switching efficiency and system stability. Moreover, essential electrical metrics are examined, including active, reactive, and apparent power. These measures will help identify potential areas for improvement in the WPT system, including efficiency and reliability.

5.5 Primary inductor without separation from the secondary inductor in WPT system under ADALINE-based ARX control

If the geometry of the two flat inductors in the WPT circuit is not separated, an analysis of the behavior of the class DE inverter with a resonant LLC series load was carried forward. The control and power stages were powered sequentially, and then the characteristic waveforms for the system stages under investigation were validated. The results are presented below in a clear, concise manner.

As expected, placing the two flat inductors in proximity led to an immediate shift in the system's natural frequency. This shift resulted from an increase in the inductance reflected into the primary, as viewed from the inverter side, which, in turn, influenced the LLC circuit's resonance frequency. It was also confirmed that the class DE inverter operates under ZVS and ZCS conditions solely at that frequency. In essence, soft switching characteristics for both current and voltage are achieved exclusively at resonance, as presumed.

Figure 5.8 illustrates the instantaneous gate-source voltage of switch Q_2, $v_{GQ2}(t)$. Additionally, it displays $v_{WPT1}(t)$ and $i_{WPT1}(t)$, representing the instantaneous load voltage and current signals, respectively, from the flat inductor of the WPT primary. Notably, the switch is turned on when both the voltage and current are near zero in the load. It has been determined that $v_{GQ2}(t)$ presents a delay of 5.20 ns relative to the $v_{WPT1}(t)$ voltage and 7.06 ns concerning the $i_{WPT1}(t)$ current. The resonance operating frequency was set to 800 kHz due to the integration of the

secondary flat inductor , resulting in a waveform period of 1.25 µs. In this context, the percentage phase shift of $v_{GQ2}(t)$ relative to the load voltage is 0.41% of the period, whereas for the current it is 0.52% of the period. This ensures the system operates in soft-switching mode, which is typical for a class DE inverter.

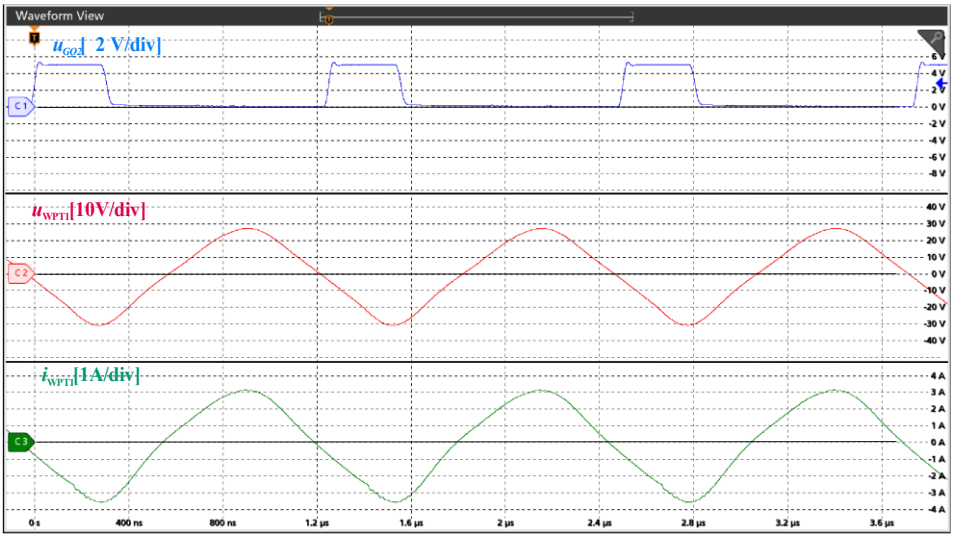

Figure 5.8: Primary WPT voltage and current, Gate-source signal of Q_2. Under ADALINE-based ARX control.

A similar analysis is conducted for Q_1 switch turning on, as illustrated in Figure 5.9. The $v_{GQ1}(t)$ waveform depicts the gate-source voltage of switch Q_1. The presence of transient events during both the turning on of Q_1 and Q_2 switches is particularly noticeable. This is primarily because the reference point for Q_1 is established through the bootstrap diode, as previously mentioned. Although this injected noise characteristic is not ideal, it does not significantly impact the system's overall behavior, as the peak values do not alter the inverter's oscillation characteristics. These values are maximum at 6.46 Vdc and minimum at -4.59 Vdc, while the gate of the GS61008P transistor operates normally within a range of -10 to 7 Vdc. The oscillation behavior indicates an underdamped system, characterized by a damping constant $\zeta < 1$. This demonstrates that following abrupt signal changes, the system stabilizes before completing a cycle at the resonance frequency. Once again, it is evident that the system meets the criteria for soft-switching, with delays of 17.45 ns relative to the load voltage and 21.83 ns relative to the load current. These values correspond to 1.44% and 1.75% of the duty cycle, respectively.

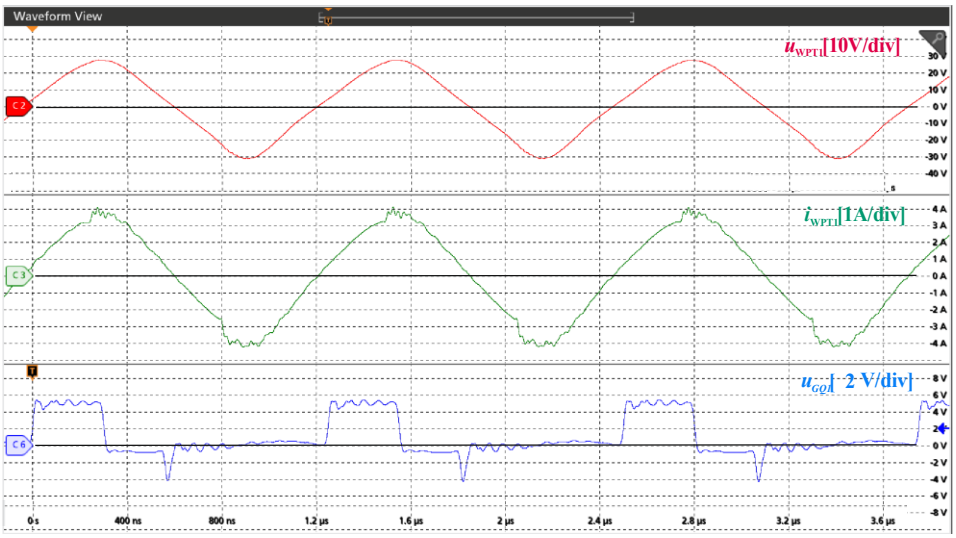

Figure 5.9: Primary WPT voltage and current, Gate-source signal of Q_1. Under ADALINE-based ARX control.

According to the theoretical framework presented in Chapter 3, the output comportment of the class DE resonant inverter is anticipated to depend on the charging and discharging cycles of the capacitors integrated into the inverter circuit, which are connected in parallel to both Q_1 and Q_2. Figure 5.10 illustrates this behavior, highlighting that the two waveforms, $vds_{Q1}(t)$ and $vds_{Q2}(t)$, are 180º out of phase as they alternately charge and discharge energy within a single duty cycle. The maximum voltages recorded are 51.24 Vdc for Q_1 and 49.67 Vdc for Q_2. The high time is estimated at approximately 655 ns, exceeding half the period of 625 ns by 30 ns. This occurrence can be attributed to the construction characteristics of the two semiconductor components and their respective intrinsic output capacitances. According to the manufacturer, these values can range from 250 pF to 330 pF, depending on the operating frequency, with the provided data based on a test frequency of 100 kHz. This variation is a valid criterion that accounts for the slight differences observed between the two components of the same model, even though it is influenced by the passive elements present in the circuit.

The maximum drain-source voltages across the two switches remain constant at the timing calculated by the ADALINE-based ARX controller. In the analyzed scenario where the WPT circuit is not separated, the duty cycle is set to 25% of the total period, specifically 312.50 ns. This timing aligns seamlessly with the moments when $vds_{Q1}(t)$ and $vds_{Q2}(t)$ reach their maximum values, as shown in Figure 5.10, which occur at approximately 310 ns for both. The rise time for the $vds_{Q1}(t)$ voltage to reach its maximum value is approximately 300 ns for a 390 pF resonant capacitor. Since the operating frequency and the MOSFET's output capacitance directly influence this duration, it is crucial to analyze these parameters. Together with the resonant capacitor, the device requires about 1/3 of the working period (420 ns) to charge and discharge the total capacitance. This explains why the maximum charging value or the minimum discharge value is not achieved at the instant of turn-on for both Q_1 and Q_2.

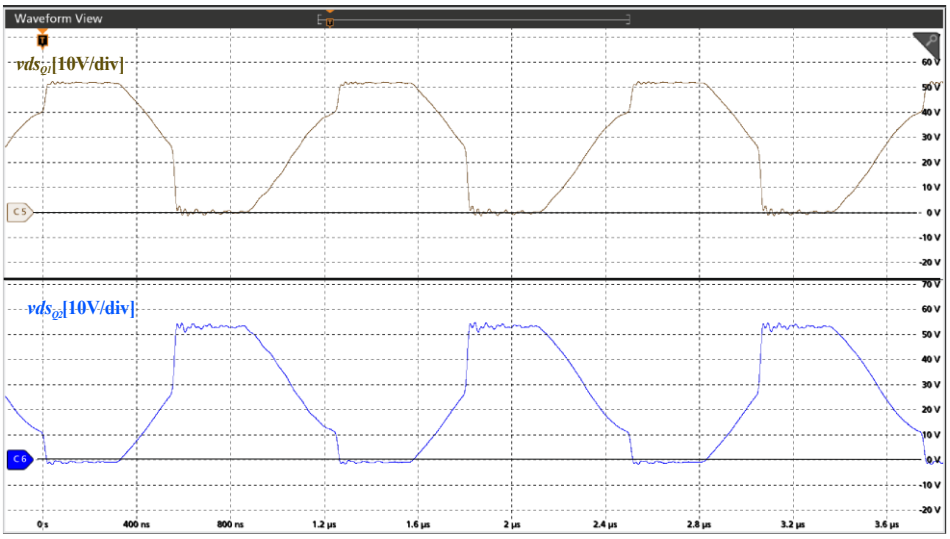

Figure 5.10: $vds_{Q1}(t)$-Drain-Source voltage of switch Q_1. $vds_{Q2}(t)$-Drain-Source voltage of switch Q_2.

Upon analyzing Figure 5.11, both the voltage signal $v_{WPT1}(t)$ and the current signal $i_{WPT1}(t)$ exhibit sinusoidal characteristics, which support the operation of the class DE half-bridge inverter near its resonance frequency. Notably, the current leads the voltage slightly, suggesting a mildly capacitive behavior typical of an inverter designed to achieve ZVS. The absence of distortions or deviations from the sinusoidal waveform indicates that the LLC filter effectively filters out the harmonics present in $vds_{Q2}(t)$.

Furthermore, examining the behavior in the frequency domain, the graphs on the right side of Figure 5.11 reveal a peak around 800 kHz, confirming the circuit's fundamental oscillation frequency. Secondary harmonics are observed at 1.62 MHz, 4 MHz, and so forth, with attenuated magnitudes of approximately -20 dBm or lower, which ensures an almost pure sinusoidal waveform. Above 10 MHz, the spectrum shows a rapid decline, indicating effective filtering and minimal EMI.

The nearly phase-aligned behavior of $v_{WPT1}(t)$ and $i_{WPT1}(t)$ results in a high active power output and a power factor approaching unity. The slight lead in current suggests that a portion of the energy exchanged between reactive elements is converted into minimal capacitive reactive power. Consequently, the system operates with high efficiency. This characteristic is typical of a resonant circuit slightly tuned above its resonance frequency, which further reduces switching losses.

The analysis revealed that the current leads the voltage by 25 ns, which corresponds to 2% of the system operating period and a phase angle of 7.2º. In addition, apparent power is calculated from the RMS values of $v_{WPT1}(t)$ and $i_{WPT1}(t)$.

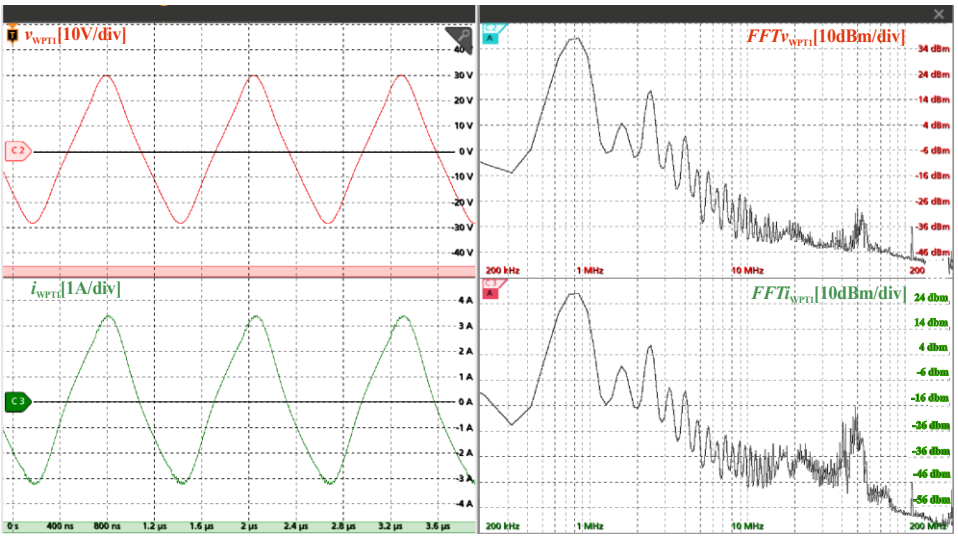

Figure 5.11: Time-domain waveforms of $v_{WPT1}(t)$ and $i_{WPT1}(t)$. Spectrum frequency waveforms of $v_{WPT1}(t)$ and $i_{WPT1}(t)$

According to IEEE 1459 norm [110], "Only pairs of voltage and current components of the same odd order contribute to active power". The active power of the WPT primary is calculated using the peak values of the Fast Fourier Transform (FFT) components 1, 3, and 5, as illustrated in Figure 5.11.

The power analysis of the Class DE resonant inverter used in the WPT system shows near-ideal resonance conditions. The RMS values measured for the primary voltage and current were $V_{WPT1,RMS}$ = 19.43 V, and $I_{WPT1,RMS}$ = 2.15 A, yielding an apparent power of S_{WPT1} = 41.77 VA. Considering a measured phase shift of ϕ_{WPT1} = 7.2°, the reactive and active power components were calculated as Q_{WPT1} = 9.63 VAR and P_{WPT1} = 40.64 W, respectively. The resultant power factor of 0.972 indicates that the inverter operates with the current waveform slightly leading the voltage, confirming a predominantly resistive load with a minor capacitive component. This behavior reflects the flat characteristics of the system's primary inductor, which ensures stable inductance, minimal reactive energy circulation, and high overall conversion efficiency under soft-switching conditions.

In accordance with IEEE Std 1459-2010 recommendation [111] and IEC 61000-4-30 standards norm [112], the evaluation of reactive power in the proposed system is conducted using a harmonic-based calculation method. This approach is especially applicable to resonant and high-frequency switching converters, where the voltage and current waveforms are inherently nonsinusoidal due to switching and resonant effects.

In the adopted methodology, the measured voltage and current signals are analyzed through frequency-domain techniques to decompose them into their fundamental and harmonic components. The fundamental reactive power component is determined by examining the phase displacement between the fundamental voltage and current components, which signifies the

energy that is alternately stored and released by the system's reactive elements. This component embodies the classical definition of reactive power under sinusoidal conditions.

Moreover, the harmonic components of voltage and current introduce distortion-related reactive effects that contribute to non-active power. As outlined in IEEE Std 1459-2010, these effects must be explicitly considered to accurately evaluate apparent power and system efficiency. For each harmonic order, the reactive power contribution is calculated based on the associated voltage and current magnitudes and their phase relationship. The total reactive power is then derived by aggregating the reactive contributions from both the fundamental and harmonic components.

This harmonic-based evaluation framework facilitates a precise distinction between active and reactive power under no sinusoidal operating conditions. By integrating harmonic effects into the calculation of reactive power, the proposed method ensures an accurate representation of power flow and losses in the system. As a result, it provides a dependable foundation for assessing power quality and evaluating efficiency in resonant- and switching-converter applications.

Figure 5.12 illustrates the measured voltage $v_{WPT2}(t)$ and current $i_{WPT2}(t)$ waveforms of the secondary circuit within the WPT system, which, in this case, was only a resistive load. The left side of the figure displays the time-domain signals, while the right side presents the corresponding frequency-domain spectra obtained through Fast Fourier Transform.

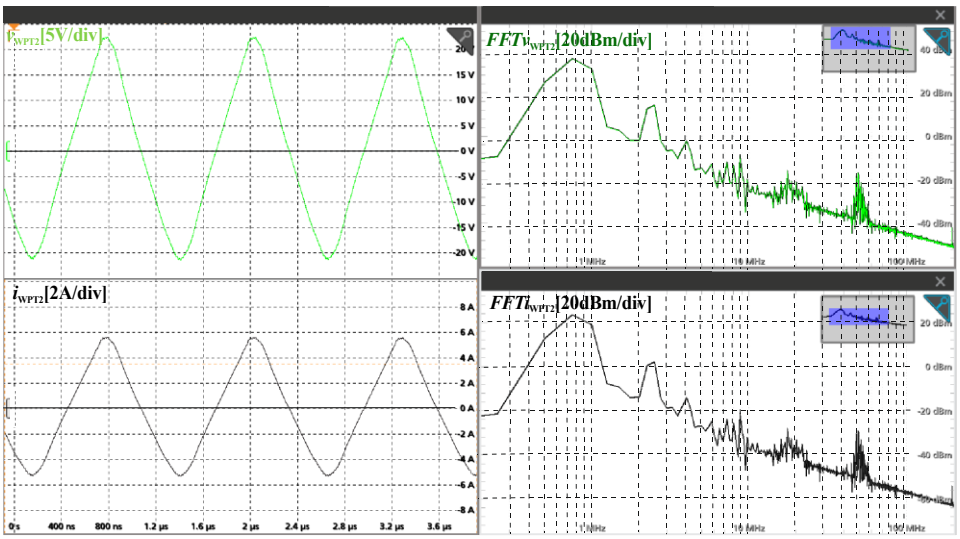

Figure 5.12: Time-domain waveforms of $v_{WPT2}(t)$ and $i_{WPT2}(t)$. Spectrum frequency waveforms of $v_{WPT2}(t)$ and $i_{WPT2}(t)$

The voltage waveform is nearly sinusoidal, with a peak-to-peak amplitude of 38.78 V. This indicates stable resonant behavior at the designed operating frequency of 800 kHz, in line with the inverter switching frequency. Similarly, the current waveform follows a sinusoidal pattern, reaching a peak-to-peak value of 9.76 A, and shows a phase shift relative to the voltage. This phase difference highlights the secondary side's resonant characteristics and reactive power behavior, which is typical of inductive wireless coupling systems. The minimal waveform

distortion suggests low harmonic content and effective resonance tuning between the transmitter and receiver coils.

The FFT spectrum indicates that both the voltage and current are primarily dominated by the fundamental frequency component near 800 kHz, with secondary harmonics appearing at lower amplitudes (below -20 dBm). Minor spectral peaks around 10 MHz correspond to switching transients or coupling-induced disturbances; however, their amplitudes remain significantly lower than that of the fundamental component, demonstrating a well-compensated link.

The secondary voltage amplitude is significantly lower than the primary ($\approx 60V_{pp,WPT1}$ vs. $40V_{pp,WPT2}$), consistent with the magnetic coupling ratio and coil design. This reduction reflects the typical energy-transfer efficiency and the coupling coefficient k < 1 in mid-range inductive systems.

The phase shift between voltage and current on the secondary side is reduced, indicating that resonant tank tuning has effectively minimized the reactive component at the load. This confirms efficient power transfer and proper alignment between the transmitter and receiver.

Additionally, the FFT analysis of the secondary signals shows lower harmonic distortion than on the primary side. This indicates that the resonant circuit functions as a band-pass filter, allowing the fundamental power component to prevail while attenuating the high frequency switching harmonics generated by the class DE inverter.

Using measurements obtained from the TEKTRONIX MSO46 oscilloscope, the RMS values from voltage and current in the secondary circuit of the WPT system were determined under the IEEE 1459 specification, and the power vector values for the secondary WPT system controlled by an ADALINE-based ARX model are: Apparent power, $S_{2WPT,CL}$ = 36.41 VA; active power, $P_{2WPT,CL}$ = 36.29 W; and reactive power, $Q_{2WPT,CL}$ = 2.93 VAR.

Secondary active power $P_{2WPT,CL}$ is lower than primary active power $P_{1WPT,CL}$, as expected, since the power delivered to the secondary load will either match or be less than the primary input due to inverter losses and coupling inefficiencies. A simple calculation of the end-to-end efficiency, defined as the active power received at the secondary divided by the power supplied by the power supply (P_{SUPPLY} = 43.20 W). It is determined that the class DE half-bridge inverter operating with an LLC resonant load, without separation in its WPT magnetic circuit and controlled by the ADALINE-based ARX strategy, achieves a total efficiency of 84.28% at a purely resistive power output.

5.6 Primary inductor without separation from the secondary inductor in WPT system under open-loop operation

An analysis like that in section 5.5 is conducted, with the key difference being that the system operates in open loop, without the ADALINE-based ARX controller. Figure 5.13 presents the turning on signals for both the Q_1 gate, $v_{GQ1}(t)$, and the Q_2 gate, $v_{GQ2}(t)$, along with the waveforms for the voltage $v_{WPT1}(t)$ and the current $i_{WPT1}(t)$ in the primary flat inductor of the WPT system. The soft-switching characteristic requirements are not met, resulting in noticeable switching losses, particularly in the $i_{WPT1}(t)$ waveform. Furthermore, the analysis indicates that the voltage over the primary WPT is not in phase with its current, leading the system to operate out of resonance. This misalignment not only aggravates losses due to magnetic coupling in the system but also adds to the previously mentioned losses associated with switching characteristics. A thorough examination of the signals reveals that the current leads the voltage by 153.31 ns, corresponding to 44.15º, or 12.26% of the duty cycle period. Additionally, the delay in the MOSFETs' turn-on relative to the voltage waveform is 87.33 ns, while the delay in the current is 240 ns.

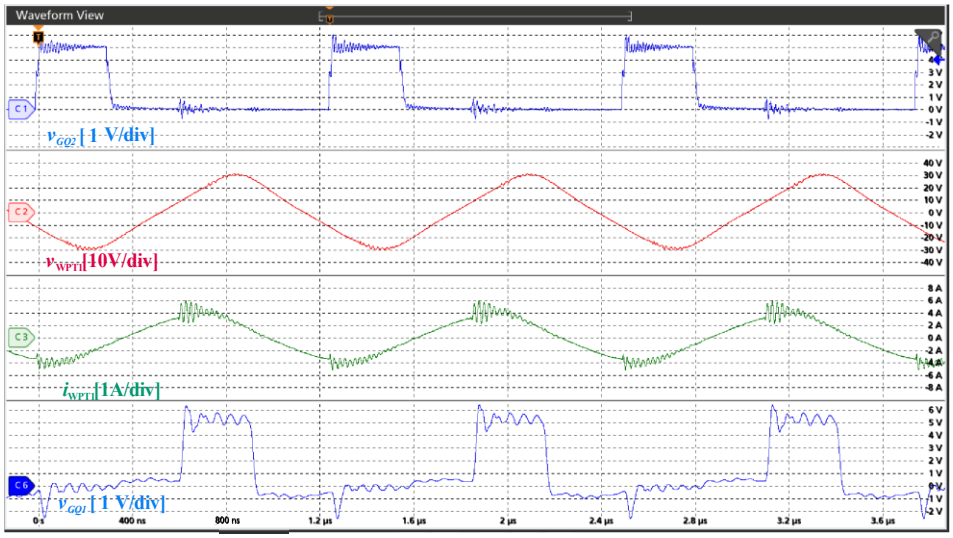

Figure 5.13: Primary WPT voltage and current, Gate-source signal of Q1 and Q2. Under open-loop operation.

Considering the RMS values of the voltage and current across the primary flat inductor, $V_{WPT1,\mathrm{RMS}} = 17.13$ V and $I_{WPT1,\mathrm{RMS}} = 2.64$ A, with their respective odd harmonic components, the vector power values are: apparent power, $S_{1WPT,OL} = 45.22$ VA; reactive power, $Q_{1WPT1,OL} = 31.50$ var; and active power, $P_{1WPT1,OL} = 32.45$ W.

The relatively high reactive power and moderate power factor confirm that the primary coil operates under partially inductive conditions, where energy oscillates between the magnetic field of the coupling coils and the resonant capacitors during each switching period. The system effectively delivers 32.45 W of real power to the load while maintaining a circulating reactive power that supports the resonant energy exchange. The moderate power factor (0.717) indicates

that tuning the ADALINE-based ARX network improves efficiency by reducing reactive power and aligning the current waveform more closely with the voltage.

Figure 5.14 presents a thorough evaluation of the experimental waveforms for the $v_{WPT1}(t)$ and $i_{WPT1}(t)$ in the WPT system, operating at a switching frequency of 800 kHz. The left-hand side displays the time-domain signals, while the right-hand side presents their corresponding frequency spectrum.

The FFT provides further insight into the waveform distortion. Both voltage and current signals show a strong fundamental component at 800 kHz, corresponding to the system's operating frequency. However, a series of higher-order harmonics can be clearly observed, extending beyond 10 MHz. The voltage spectrum exhibits intense harmonic peaks, indicating substantial nonlinearity and transient overshoot due to abrupt switching edges. The current spectrum, although also distorted, has relatively lower harmonic amplitudes due to the partial filtering effect of the resonant elements.

Overall, the spectral behavior and waveform shapes confirm that the system is not achieving ZVS and ZCS, and therefore operates under hard-switching conditions. This operating mode leads to increased power losses and spectral spreading, thereby reducing the converter's electromagnetic compatibility. The results highlight the need to restore the soft-switching regime typical of a Class DE inverter by returning the ADALINE-based ARX network controller.

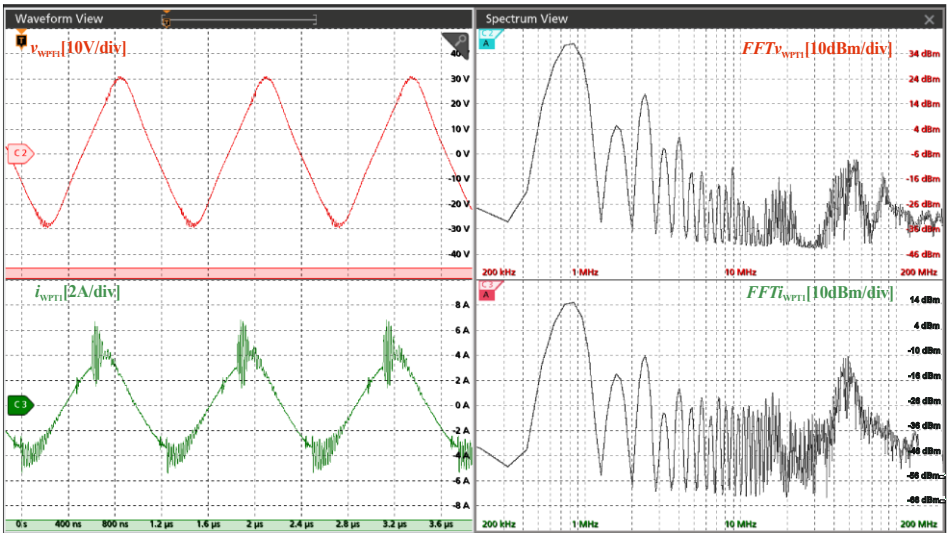

Figure 5.14: Time-domain and Spectrum frequency waveforms of vWPT1(t) and iWPT1(t) under open-loop operation.

Figure 5.15 presents the drain-to-source voltage waveforms, $v_{dsQ1}(t)$ and $v_{dsQ2}(t)$, for both switches of the Class DE inverter operating under open-loop conditions at a switching frequency of 800 kHz. As previously noted, the illustrated waveform reflects a suboptimal switching response in the resonant inverter. The high-frequency oscillations further indicate the generation

of significant high-order harmonics, resulting in additional power losses and increased stress on the semiconductors.

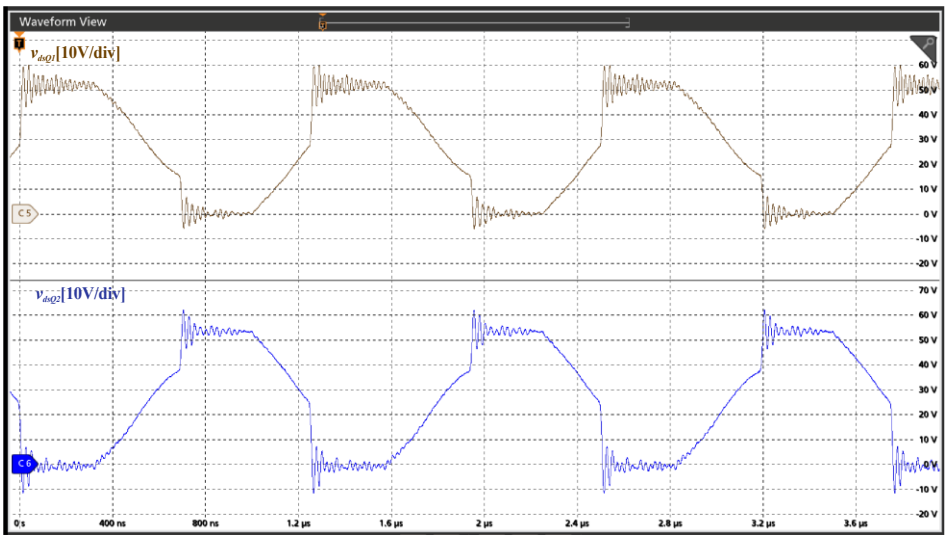

Figure 5.15: $vds_{Q1}(t)$-Drain-Source voltage of switch Q_1. $vds_{Q2}(t)$-Drain-Source voltage of switch Q_2

The transient response that occurs when each switch is turned on generates an oscillation that persists throughout the entire duration when the $v_{dsQ1}(t)$ and $v_{dsQ2}(t)$ waves remain constant, at 50 V or 0 V. During this transient response, an oscillation frequency of 41 MHz and a maximum peak-to-peak voltage of 70.60 V is observed. Given that the decay of the transient regime follows an exponential pattern, the time constant for this phenomenon has been determined to be $\tau = 1.41$ µs, which is significantly longer than the transient period measured at 24.4 ns. As a result, this leads to slow settling time, characteristic of an underdamped system that dissipates more energy before achieving stability.

Due to overshoots and oscillatory transients, the drain-source voltage reaches approximately 60 V, displaying high-frequency ringing superimposed on the fundamental switching pattern. This phenomenon is attributed to the resonance between the MOSFET output capacitance C_{oss} and the parasitic inductances present within the commutation loop. The incomplete discharge of C_{oss} before turn-on leads to an overlap between the drain voltage and current, resulting in additional switching energy losses and increased device stress [113].

A quantitative estimation of the energy stored in the parasitic elements can be expressed in equation (4.3) for capacitive losses and equation (4.4) for inductive losses.

$$E_C = \frac{1}{2} C_{OSS} \times V_{ds}^2 \tag{4.3}$$

$$E_L = \frac{1}{2} L_{OSS} \times I_{d,peak}^2 \tag{4.4}$$

Where E_c is the capacitive losses, E_L is the inductive losses, V_{ds} is the drain-source peak voltage switch, $I_{d,peak}$ is the peak drain current switch, C_{OSS} is the switch parasitic capacitance, and L_{OSS} is the PSB parasitic inductance.

The measured parameters V_{ds} = 60 V, $I_{d,peak}$ = 8 A, C_{oss} = 250 pF, and L_{oss} = 10 nH, the total transient energy per switching event is approximately 680 nJ. This corresponds to a switching power dissipation of nearly 0.54 W per device at 800 kHz.

While a portion of this energy may be recovered through resonant components, a significant amount is dissipated as heat within the semiconductor channel. This is illustrated in Figure 5.16, where the maximum temperature across the switch reaches 80.3ºC. The operating junction temperature range for the GS61008P MOSFET is -55 °C to +150 °C. Furthermore, spectral analysis of the transient response reveals oscillations at approximately 41 MHz, corresponding to the resonance of the over-cited parasitic LC network. This high-frequency energy content not only intensifies EMI emissions but also exacerbates junction stress, thereby accelerating degradation mechanisms such as hot-carrier injection and dielectric fatigue [114]. The combined effects of high dv/dt, ringing, and partial hard switching consequently reduce converter efficiency and may compromise device reliability.

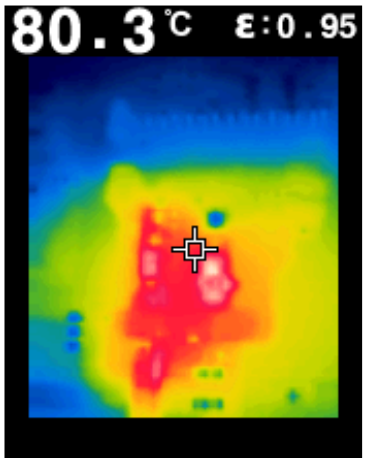

Figure 5.16: Thermal Characteristics for GS61008P MOSFET working in open-loop

As previously analyzed, Figure 5.17 displays the waveforms in both the frequency and time domains for current and voltage in the secondary WPT circuit, which supplies a resistive load of 3.9 ohms. The measurements obtained indicate that the RMS voltage at the secondary, $V_{WPT2,RMS}$, is 11.42 V, and secondary RMS current, $I_{WPT2,RMS}$, is 2.45 A. Therefore, the active power delivered to the secondary is $P_{2WPT,OL}$ = 27.55 W, the apparent power is $S_{2WPT,OL}$ = 27.63 VA, and the reactive power is $Q_{2WPT,OL}$ = 2.05 var. Additionally, it was found that the current phase shift to the voltage is 14.82 ns, corresponding to an angle of 4.26°, or 1.2% of the total period at the switching frequency. In the time domain, both signals exhibit quasi-sinusoidal behavior with noticeable high-frequency oscillations superimposed on the fundamental component. These oscillations,

which were confirmed, are attributed to residual switching interactions and parasitic resonances between the coil inductance and parasitic capacitance, among other factors.

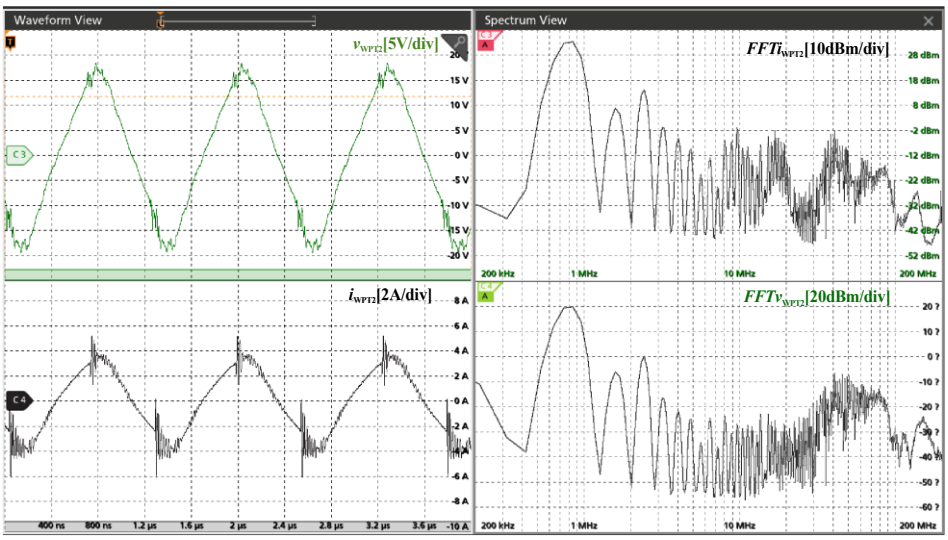

Figure 5.17: Time-domain and Spectrum frequency waveforms of $v_{WPT2}(t)$ and $i_{WPT21}(t)$ under open-loop operation.

The corresponding frequency-domain representation, obtained via fast Fourier transform, reveals the dominant fundamental component at 800 kHz, consistent with the system's designed resonant frequency. However, the presence of multiple harmonic components extending beyond 10 MHz indicates a non-ideal resonance condition and partial distortion in the current waveform. The harmonic distribution suggests that, without feedback control, the system exhibits reduced spectral purity and increased electromagnetic interference emissions.

Overall, the analysis confirms that the absence of a controller allows coupling-dependent variations to perturb the resonance balance, resulting in increased harmonic content and decreased power transfer efficiency for a power supply of P_{SUPPLY} = 38.70 W. The WPT system efficiency without controller operation and without T_x-*to*-R_x separation is equal to 71.39%.

5.7 Primary inductor separated by 5 cm from the secondary inductor in WPT system under ADALINE-based ARX control

In the ongoing validation of the WPT system, the magnetic circuit was modified to achieve a 5 cm separation between the flat coils. This adjustment resulted in the waveforms shown in Figure 5.18, which illustrate the system's behavior under the ADALINE-based ARX control strategy. The duty cycle for the switches was set to 35% of the period, resulting in approximately 450 ns during the high state and 800 ns during the low state, including the necessary protection time to prevent cross-conduction between the two MOSFETs.

The analysis of the voltage and current waveforms in the primary inductor of the WPT system reveals values of $V_{WPT1,RMS}$ = 15.02 V, $I_{WPT1,RMS}$ = 388.60 mA, the reactive power, $S_{1WPT,CL5}$ = 5.83 VA; the active power, $P_{1WPT,CL5}$ = 5.02 W; and the reactive power, $Q_{1WPT,CL5}$= 2.96 var with

an oscillation frequency, f_{sw} = 799.45 Hz. Regarding the phase relationship between voltage and current, a phase shift of 13.35 ns in lead was observed for $i_{WPTI}(t)$. Additionally, the turn-on gate-source signal exhibits delays of 41 ns and 27 ns for the current and voltage in the primary planar inductor, respectively.

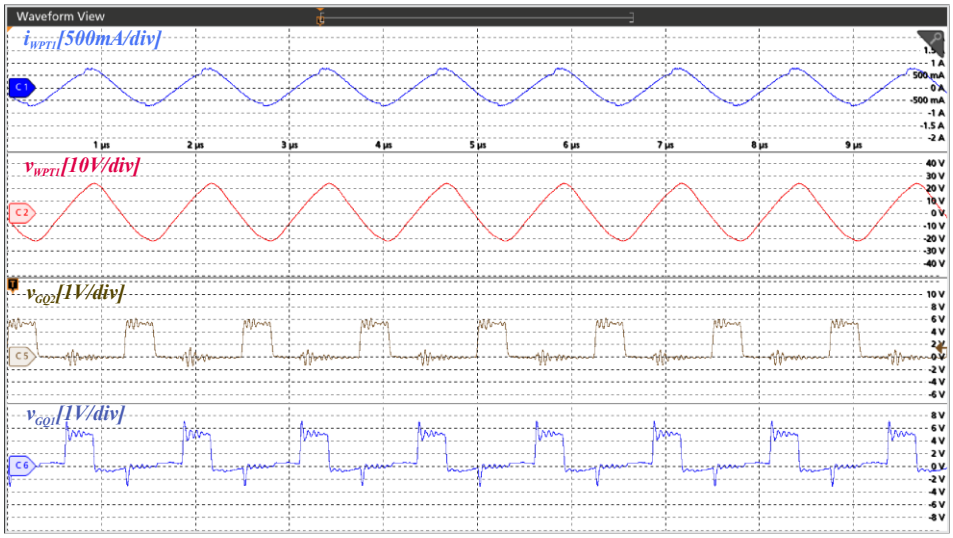

Figure 5.18: $v_{GQ1}(t)$ and $v_{GQ2}(t)$ gate-source waveforms, $v_{WPTI}(t)$ and $i_{WPTI}(t)$ primary WPT voltage and current waveforms.

Figure 5.19 illustrates the voltage $v_{WPTI}(t)$ and current $i_{WPTI}(t)$ waveforms for the primary side of the WPT system when the transmitting and receiving coils are separated by 5 cm. In the time domain, both signals exhibit sinusoidal behavior at approximately 800 kHz, confirming the system's resonant operation. However, a slight phase shift between the voltage and current waveforms is observed, indicating the presence of reactive components that reduce power transfer efficiency at this increased distance.

This behavior highlights the sensitivity of Class DE resonant inverters to variations in the coupling distance in WPT systems. As the separation between coils increases, the degraded magnetic coupling reduces power transfer efficiency. It compromises soft-switching performance, highlighting the sensitivity of Class DE resonant inverters to variations in coupling distance in WPT systems. As the separation between coils increases, the degraded magnetic coupling reduces power transfer efficiency and compromises soft-switching performance.

The frequency domain analysis reveals that the dominant spectral components are concentrated near the fundamental resonance frequency, with secondary harmonics extending beyond 10 MHz. Compared to the smaller coupling distance, the harmonic magnitudes are more pronounced, indicating higher levels of parasitic oscillations and electromagnetic noise resulting from weaker magnetic coupling. The attenuation of the fundamental peak also reflects the reduction in mutual inductance between the coils as the separation distance increases.

Overall, the results demonstrate that increasing the air gap to 5 cm significantly affects the coupling coefficient 0.01, < k < 0.1, and energy transfer capability, leading to a decrease in power efficiency and an increase in spectral distortion.

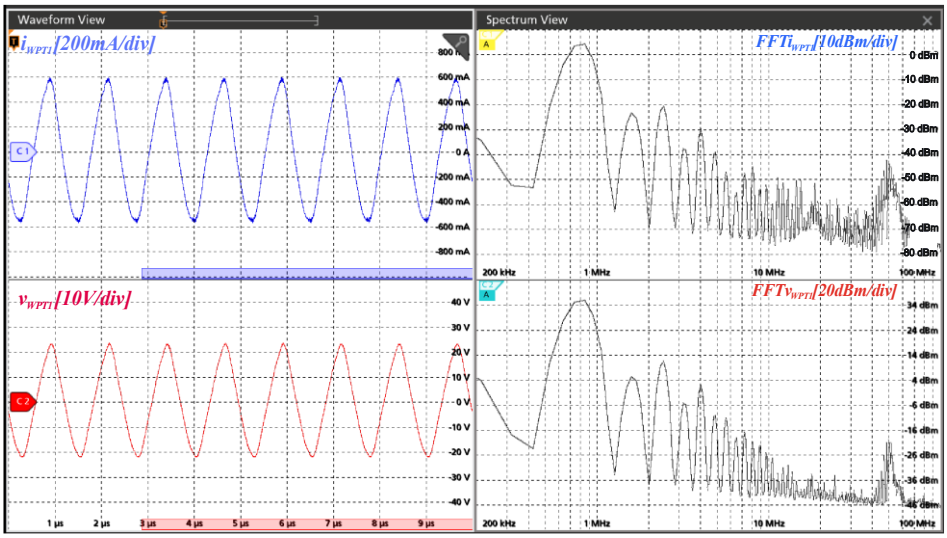

Figure 5.19: Time-domain and spectrum frequency waveforms of vWPT1(t) and iWPT1(t) under ADALINE-based ARX Control.

Figure 5.20 presents the drain-source voltage waveforms for switches Q_1 and Q_2 in the class DE inverter. The maximum peak value observed for V_{dsQ1} is 53.61 V, while V_{dsQ2} reaches 54.65 V. As in the analysis in 5.5, it is evident that the switch is turned-on before the drain-source voltage reaches its peak. However, in this instance, the characteristic is accentuated by the longer duty cycle, indicating that the capacitor connected in parallel with each MOSFET does not fully charge.

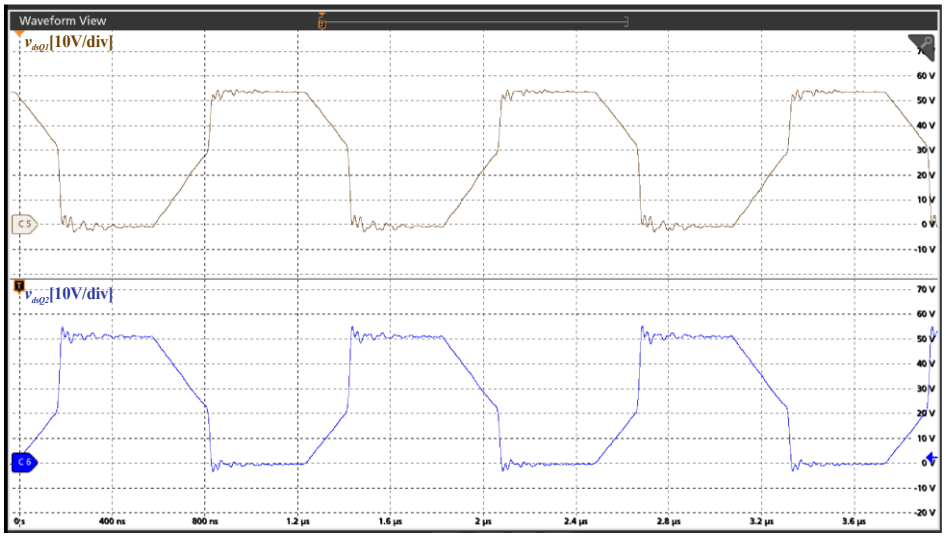

Figure 5.20: $v_{dsQ1}(t)$ and $v_{dsQ2}(t)$ under ADALINE-based ARX control

The signals exhibit a quasi-square waveform with slight voltage overshoot and oscillatory behavior during the switching transitions. These oscillations originate from parasitic inductances and capacitances within the inverter and resonant tank, becoming more evident as the coupling coefficient between the primary and secondary coils decreases. This behavior highlights the

ClassDE resonant inverter's sensitivity to variations in the coupling distance in WPT systems. As the separation between coils increases, the degraded magnetic coupling reduces power transfer efficiency and compromises soft-switching performance.

Figure 5.21 presents the time and frequency domain analysis of the secondary voltage $v_{WPT2}(t)$ and current $i_{WPT2}(t)$ in the WPT system operating at a switching frequency of 800 kHz. The measured RMS values of the voltage and current are $V_{WPT2,RMS}$ = 4.47 V and $I_{WPT2,RMS}$ = 1.05 A, respectively. The angle of advance of the current in relation to the voltage is 12.04º. This indicates a purely resistive load condition at the secondary side, confirming that the reactive energy exchange between the resonant tank and the load is minimal.

In the time domain, both the voltage and current waveforms exhibit well-defined sinusoidal characteristics with minimal distortion, indicating that the resonant compensation network is correctly tuned. This tuning ensures efficient energy transfer between the primary and secondary coils. The frequency-domain plots further support this observation by showing a dominant spectral component at the fundamental operating frequency of 800 kHz, along with significant attenuation of higher-order harmonics. The harmonic components above 10 MHz remain significantly lower than the primary spectral peak.

The power vector values from the energy transferred to the 3.9-ohm load, which is connected in parallel with the WPT secondary flat inductor are: $S_{2WPT,CL5}$ = 4.69 VA, $P_{2WPT,CL5}$ = 4.09 W and $Q_{2WPT,CL5}$ = 2.29 var. Based on this information , the efficiency of the WPT system with a separation of 5 cm between Tx to Rx and under ADALINE-based ARX control is equal to 55.19%.

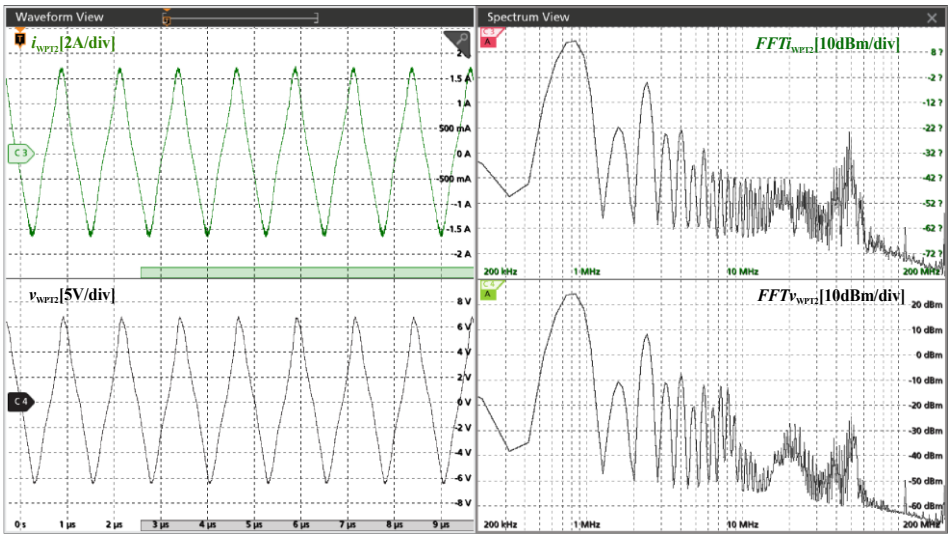

Figure 5.21: Time-domain and spectrum frequency waveforms of vWPT2(t) and iWPT2(t) under ADALINE-based ARX control

5.8 Primary inductor separated by 5 cm from the secondary inductor in WPT system under open-loop operation

Figure 5.22 displays the gate-source voltage waveforms for Q_1 and Q_2, along with the voltage and current in the primary inductor of the WPT system. The RMS values recorded are $V_{WPT1,RMS}$ = 15.84 V, and $I_{WPT1,RMS}$ = 273 mA. The lead time of the current relative to the voltage is measured at 72 ns, corresponding to a phase shift of 20.73º. Additionally, the switch's turn-on time delay relative to the load voltage waveform is set to 177 ns, corresponding to 14.16% of the period. A significant harmonic content is also observed, particularly in the current waveform, because the system is not operating under soft switching conditions. $v_{GQ1}(t)$ and $v_{GQ2}(t)$ exhibit some harmonic interference, indicating that they are turned on under non-soft-switching conditions.

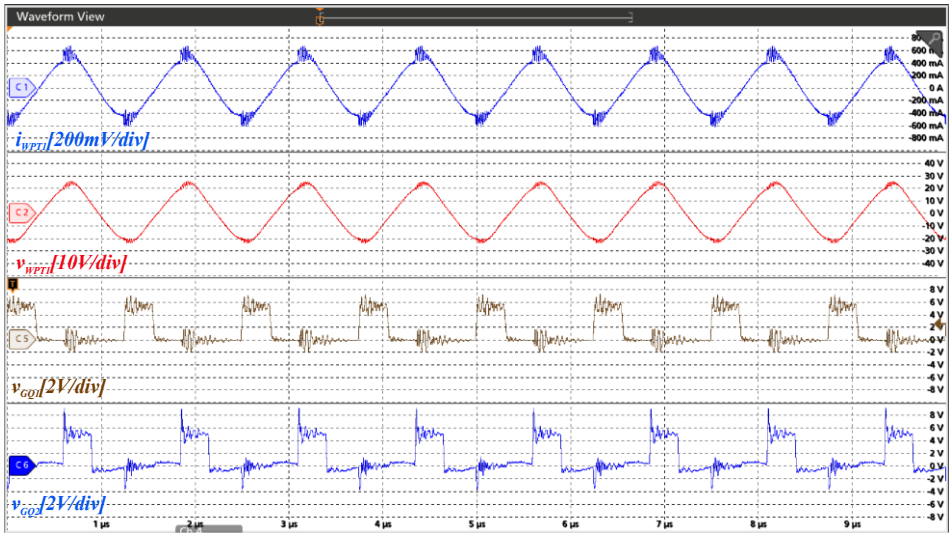

Figure 5.22: $v_{GQ1}(t)$ and $v_{GQ2}(t)$ gate-source waveform, $v_{WPT1}(t)$ and $i_{WPT1}(t)$ over the primary WPT under open-loop operation.

The maximum value for $v_{GQ2}(t)$ exceeds 6 Vdc, the limit specified by the MOSFET datasheet. The power values for the WPT system under open-loop operation with a 5 cm gap between the flat inductors are: active power, $P_{1WPT1,OL5}$ = 3.52 W; apparent power, $S_{1WPT,OL5}$ = 4.32 VA; reactive power, $Q_{1WPT1,OL5}$ = 2.49 var; and power supply, P_{SUPPLY} = 5.89 W.

Figure 5.23 presents the experimental time and frequency domain characteristics of the primary side of the WPT system operating under open-loop conditions with a 5 cm air gap between the transmitting and receiving coils.

In the time domain, the voltage waveform $v_{WPT1}(t)$ exhibits a nearly sinusoidal profile at the fundamental frequency, while the current waveform $i_{WPT1}(t)$ shows slight distortion near the crossing regions. This distortion indicates a deviation from ideal resonant operation, likely due to the moderate magnetic coupling at a 5 cm separation. Reduced coupling impairs energy transfer efficiency and causes a phase shift between voltage and current.

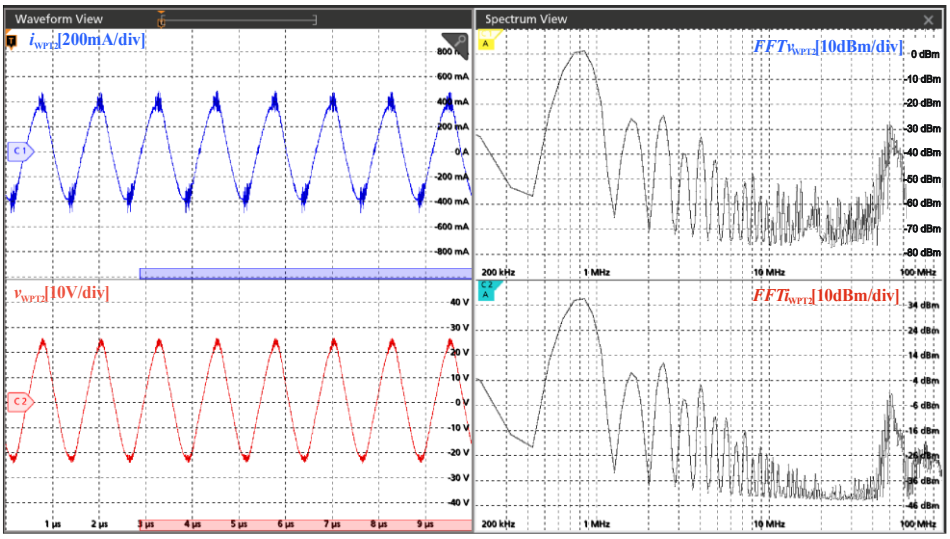

Figure 5.23: Time-domain and Spectrum frequency waveforms of $v_{WPT1}(t)$ and $i_{WPT1}(t)$ under open-loop operation.

The frequency domain analysis reveals that the dominant power component is primarily concentrated at the fundamental frequency of approximately 800 kHz, accompanied by multiple harmonic components extending up to 10 MHz. The amplitude of these harmonics indicates the nonlinear behavior of the class DE inverter operating under open-loop conditions, particularly during switching transitions and in the presence of non-ideal soft-switching. Notably, the voltage level in the primary WPT system remains relatively stable despite the occurrence of magnetic circuit separation. This stability is mainly attributable to the consistent turning on of the switches, even in the absence of the ADALINE-based ARX controller.

Figure 5.24 illustrates the drain-source voltage waveforms of transistors Q_1 and Q_2 during the open-loop operation of the Class DE inverter. Both devices exhibit characteristic high-frequency oscillations immediately after each switching transition, which are attributed to the interaction between the parasitic output capacitances and the stray inductances in the circuit layout.

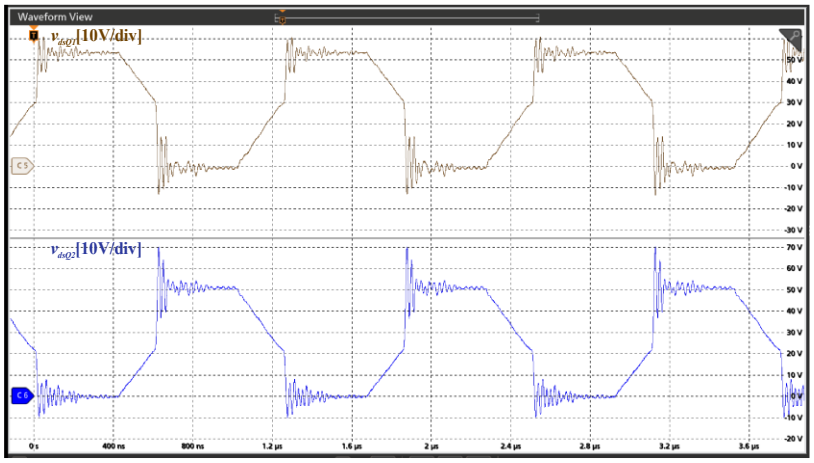

Figure 5.24: $vds_{Q1}(t)$-Drain-Source voltage of switch Q_1. $vds_{Q2}(t)$-Drain-Source voltage of switch Q_2

The measured ringing period of approximately 24 ns corresponds to a transient frequency of around 41.7 MHz, indicating the presence of a high-frequency resonant mode at the switching node. The transient amplitude decreases from 64 V to 54 V over approximately 240 ns, defining the oscillation's accommodation time. By analyzing this decay behavior, the time constant was estimated to be approximately 1.4 µs, yielding a damping ratio of about 0.003, indicating a highly underdamped condition. This behavior confirms that the converter operates under non-ideal soft-switching conditions, where parasitic energy exchange persists after each transition, potentially leading to increased switching losses and electromagnetic interference.

Figure 5.25 illustrates the secondary-side voltage $v_{WPT2}(t)$ and current $i_{WPT2}(t)$ waveforms of the WPT system operating in open loop, with a 3.9 Ω resistive load and a 5 cm air gap between the transmitting and receiving coils. The time-domain signals exhibit nearly sinusoidal behavior, with minor distortions attributed to high-frequency coupling effects and switching harmonics generated by the Class DE inverter. The voltage amplitude reaches approximately 3.5 V peak, while the current amplitude is around 0.9 A peak, reflecting the weak magnetic coupling at this coil separation distance.

The corresponding FFT shows a fundamental component at 800 kHz, consistent with the inverter's switching frequency, along with significant harmonic content extending beyond 10 MHz. These higher-order harmonics result from parasitic capacitances, imperfect resonant tank tuning, and non-ideal switching transitions. The moderate harmonic amplitudes (below –20 dBm) indicate that, while power transfer remains efficient, some energy is dissipated as electromagnetic noise, slightly diminishing the overall transfer efficiency. This behavior underscores the impact of coil separation on coupling strength, harmonic distortion, and the spectral purity of the transferred power.

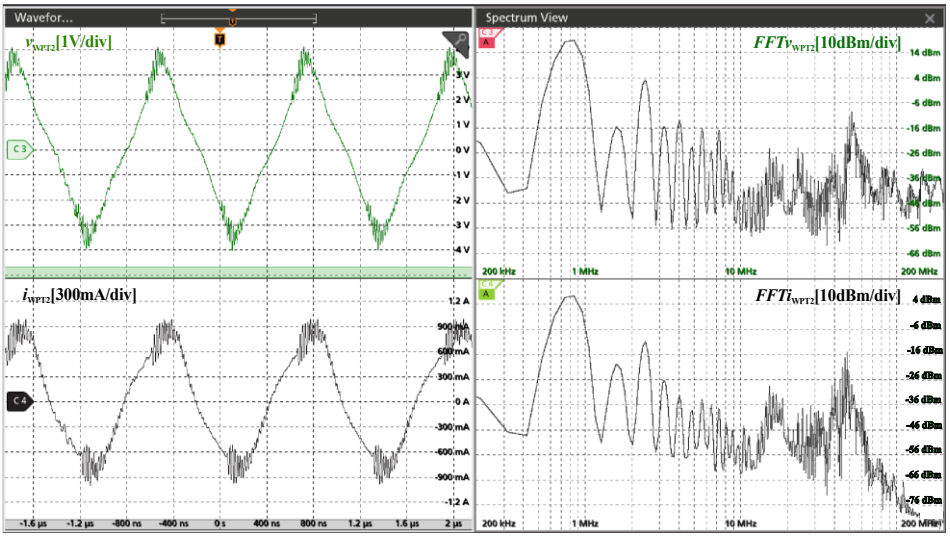

Figure 5.25: Time-domain and Spectrum frequency waveforms of $v_{WPT2}(t)$ and $i_{WPT2}(t)$ under open-loop operation.

Under the stated conditions, the secondary side delivers approximately $S_{2WPT,OL5}$ = 1.62 VA of apparent power, $P_{2WPT,OL5}$ = 1.62 W of active power, and $Q_{2WPT,OL5}$ = *179.72 mvar of reactive power*. The near-unity power factor confirms that most delivered power is real and dissipated in the resistive load.

Based on the analysis of the active P_{SUPPLY}, and the active power delivered in the secondary $P_{2WPT,OL5}$, the efficiency of the WPT system operating without the control stage and 5 cm separation between the flat coils is equal to 27.30%.

Figure 5.26 illustrates the thermal image of the GS61008P GaN MOSFET operating within the Class DE inverter topology under steady-state conditions. The infrared thermograph shows a peak surface temperature of 69.5 °C at the device's active area. This temperature reflects the thermal stress resulting from high-frequency switching at around 800 kHz in this system, along with the conduction and switching losses inherent to GaN-based power devices. The relatively high junction temperature suggests that, although the device efficiently manages fast transitions and high power density, soft-switching conditions were not fully achieved. This has led to partial overlap of voltage and current during switching transitions. The thermal distribution shows a concentrated hot spot in the central region, surrounded by a gradual temperature gradient across the substrate and PCB.

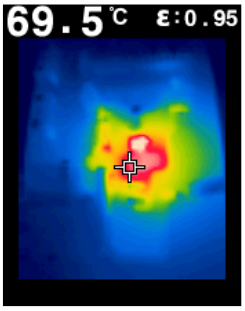

Figure 5.26: Thermal Characteristics for GS61008P MOSFET working in open loop.

5.9 Primary inductor separated by 10 cm from the secondary inductor in WPT system under ADALINE-based ARX control

Figure 5.27 illustrates the behavior of the WPT system in both the time and frequency domains when the transmitting and receiving coils are separated by 10 cm. In the time domain, both the primary voltage, $v_{WPT1}(t)$, and current, $i_{WPT1}(t)$, exhibit quasi-sinusoidal shapes, indicating that the resonant condition is largely maintained despite the increased separation. However, the amplitudes of the secondary voltage, $v_{WPT2}(t)$, and current, $i_{WPT2}(t)$, are significantly lower than at shorter distances, highlighting the weaker magnetic coupling between the coils at this 10 cm distance. The secondary voltage remains below 2 V, and the current falls below 0.8 A, suggesting a decline in power transfer efficiency due to reduced mutual inductance.

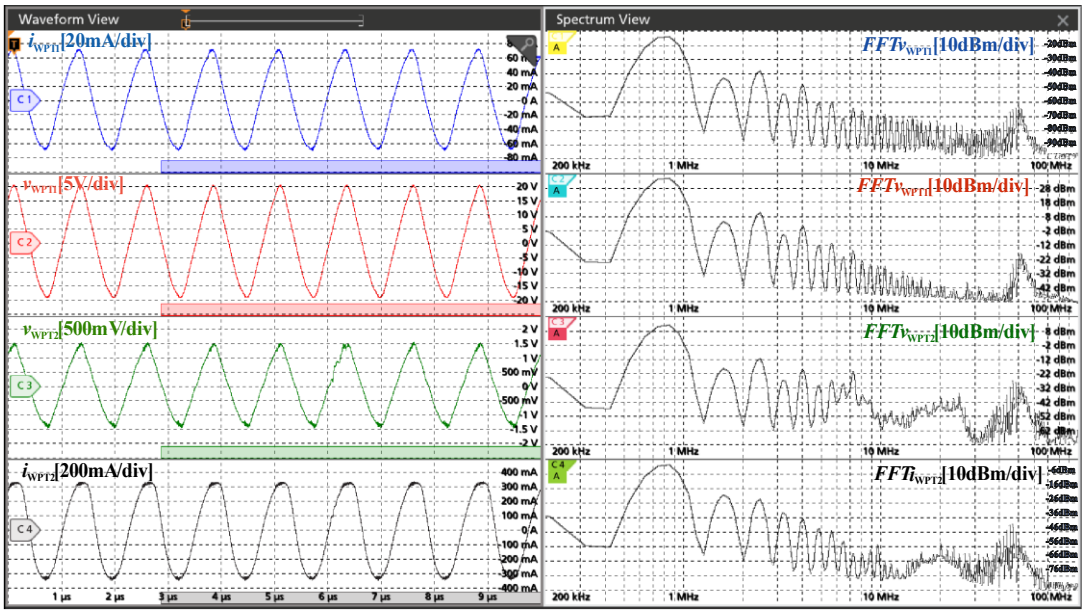

Figure 5.27: Time-domain and spectrum frequency waveforms of primary and secondary voltage and current from WPT system under ADALINE-based ARX Control

In the frequency domain, the FFT spectrum confirms that the system's dominant operational frequency is centered around 800 kHz, aligning with the designed resonant frequency. However, as coupling weakens, the spectral density of higher harmonics increases, particularly beyond 10 MHz. This increase may be attributed to the nonlinear switching behavior of the Class DE inverter and imperfect impedance matching at longer distances.

Analysis of the waveforms from the WPT system, as described previously, reveals the following values: $V_{WPT1,RMS}$ = 14.40 V, $I_{WPT1,RMS}$ = 47.67 mA, $V_{WPT2,RMS}$ = 1.02 V, and $I_{WPT2,RMS}$ = 258 mA. The primary circuit exhibits a current lead of 32 ns, equivalent phase shift of 9.22º , in relation to the voltage. For the secondary circuit, this phase shift angle is equal to 4.32º.

The power parameters for the WPT system operating with a 10 cm separation between the transmitting and receiving coils under ADALINE-based ARX control on the primary side are: apparent power, $S_{1WPT,CL10}$ = 686.88 mVA; the active power, $P_{1WPT,CL10}$ = 661.95 mW; the reactive component, $Q_{1WPT,CL10}$ = 183.51 mvar; and the power supply P_{SUPPLY} = *0.824 W*.

In contrast, the secondary side exhibited an apparent power of $S_{2WPT,CL10}$ = 263.16 mVA, where $P_{2WPT,CL10}$ = 251.44 mW corresponded to the active component and $Q_{WPT,CL10}$ = 77.55 mVAR to the reactive component, yielding a power factor of $cos\phi_2$ = 0.954. Despite the secondary resonant circuit's high-quality power factor, the energy transmitted remained low due to significant reductions in magnetic coupling at this distance.

The transmission efficiency, equal to 30.46%, shows that only a small fraction of the primary supply power reaches the load. This low efficiency is primarily attributed to the weak coupling coefficient between the coils at 10 cm, resulting in reduced mutual inductance and higher leakage flux.

5.10 Primary inductor separated by 10 cm from the secondary inductor in WPT system under open-loop operation

Figure 5.28 illustrates the time-domain and frequency-domain responses of the WPT system operating under open-loop conditions. The measurements comprise the primary current i_{WPT1}, primary voltage v_{WPT1}, secondary voltage v_{WPT2}, and secondary current i_{WPT2}, along with their corresponding frequency spectral graphs.

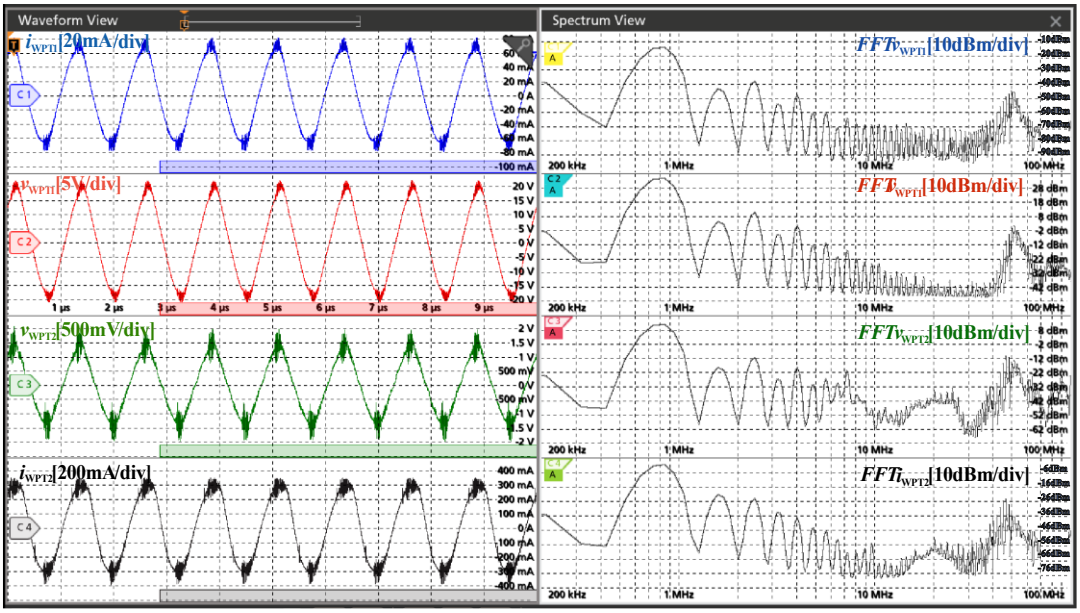

Figure 5.28: Time-domain and spectrum frequency waveforms of primary and secondary voltage and current from WPT system under open-loop conditions

In the time domain, the waveforms of the primary voltage and current keep a quasi-sinusoidal nature with a slight phase displacement. The signals on the secondary side exhibit lower-amplitude oscillations, a consequence of the reduced magnetic coupling due to the spatial separation of the coils. Furthermore, the secondary voltage waveform exhibits increased oscillatory distortions, which can be attributed to leakage inductance and the imperfect energy-transfer efficiency of the resonant link.

The frequency-domain representation reveals a fundamental harmonic at 800 kHz, corresponding to the system's switching frequency, along with noticeable high-frequency harmonics extending up to 10 MHz. The power spectral densities of both voltage and current decrease rapidly beyond the fundamental component, indicating that the resonance network effectively filters out most high-frequency components.

The RMS voltage and current values for both the primary and secondary circuits are as follows: $V_{WPT1,RMS}$ = 13.11 V, and $V_{WPT2,RMS}$ = 955.80 mV, $I_{WPT1,RMS}$ = 47.78 mA and $I_{WPT2,RMS}$ = 224.65 mA. The phase angle between the current and the voltage in the primary circuit is 41.4 ns. In the secondary circuit with a purely resistive load, the phase shift was measured at 22 ns. This shift is primarily since both the voltage and current waveforms are not entirely sinusoidal.

The power parameters of the WPT system operating with a 10 cm separation between the transmitting and receiving coils under open-loop conditions are: P_{SUPPLY} = 715.55 mW; $S_{1WPT,OL10}$ = 626.39 mVA; $P_{1WPT,OL10}$ = 562.07 mW; $Q_{1WPT,OL10}$ = 276.10 mVAR for the primary side; and $S_{2WPT,OL10}$ = 214.72 mVA; $P_{2WPT,OL10}$ = 199.73 mW; $Q_{2WPT,OL10}$ = 78.81 mVAR; for the secondary side. Finally, the efficiency of the WPT system operating in open-loop mode with a 10 cm separation between the transmitter and receiver is equal to 27.91%.

5.11 Class DE resonant inverter performance under ADALINE-based ARX controller operation

The performance of the ADALINE-based ARX controller is evaluated by comparing its output with the reference (validation) data obtained during the neural network training phase. Figure 5.29 illustrates the relationship between the WPT equivalent impedance and the corresponding duty cycle, showing both the validation values and the estimates from the ADALINE-based ARX model.

The results indicate that the controller accurately captures the nonlinear trend observed in the validation dataset across the analyzed range of impedances. Notably, as the WPT impedance increases, the duty cycle decreases smoothly and monotonically, a behavior that the ADALINE-based ARX output consistently reflects. The close alignment between the estimated curve and the validation points demonstrates the model's effectiveness in generalizing the system behavior beyond the training samples.

Minor discrepancies between the ADALINE-based ARX predictions and the validation values are evident at intermediate impedance levels; however, these variations are minimal and do not compromise the overall trend or control objectives. This suggests that the controller retains robustness while achieving a high degree of accuracy in adjusting the duty cycle in response to impedance variations.

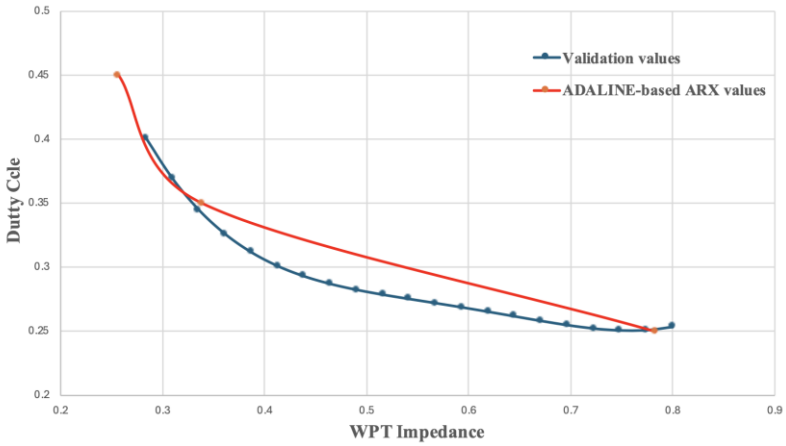

Figure 5.29: ADALINE-based ARX Controller performance

Overall, the strong correlation between the validation data and the ARX-based estimates substantiates the effectiveness of the ADALINE learning process and reinforces the suitability of the proposed controller for real-time impedance adaptation in the WPT system.

Figure 5.30 presents the effects of the WPT circuit gap on power transfer efficiency within the framework of an ADALINE-based ARX control scheme. As the distance between the primary and secondary circuits increases, both efficiencies experience a decline due to weakened magnetic coupling. The primary WPT efficiency (represented by the red curve) begins at a high level of approximately 94% at a gap of 0 cm, then drops significantly to around 67.8% at 5 cm, before stabilizing with a slight improvement at 10 cm, reaching about 68.1%. This trend indicates the effective compensation provided by the adaptive ARX controller. In contrast, the secondary WPT efficiency (depicted by the blue curve) exhibits a more pronounced and steady decrease, falling from approximately 84% at 0 cm to about 30.5% at 10 cm. This decline highlights its greater sensitivity to misalignment and increasing distance. Overall, the figure illustrates the robustness of primary-side efficiency under adaptive control, despite deteriorating coupling conditions.

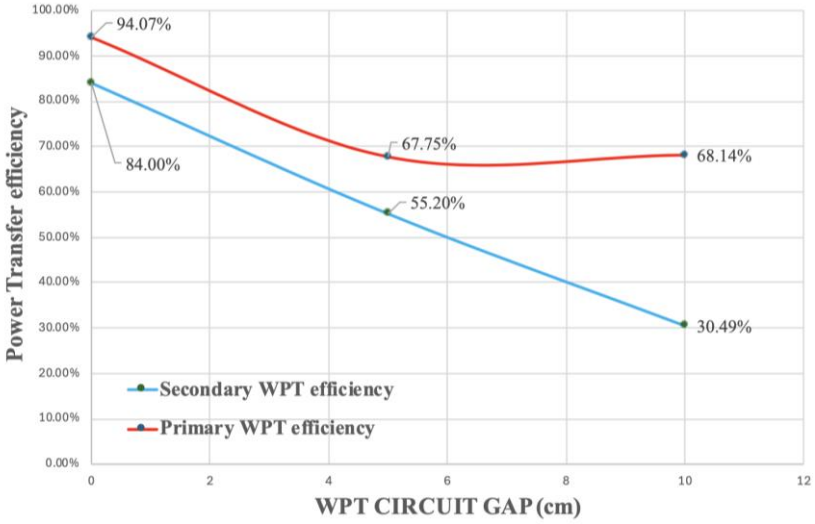

Figure 5.30: WPT system under ADALINE-based ARX operation

Figure 5.31 illustrates the performance of the WPT system operating under open-loop control, highlighting how power transfer efficiency varies with the distance between the primary and secondary coils. As the separation distance increases, there is a noticeable decline in efficiency, primarily due to diminished magnetic coupling and the lack of adaptive compensation. At a zero gap, the system demonstrates relatively high efficiencies, achieving approximately 83.85% on the primary side and 71.19% on the secondary side. However, when the gap widens to 5 cm, both efficiencies drop significantly, reaching 59.76% for the primary circuit and 27.33% for the secondary circuit. This considerable reduction underscores the sensitivity of the open-loop configuration to variations in coupling and load mismatches. At a gap of 10 cm, primary efficiency regains some ground, rising to 78.55%, likely due to resonance conditions, while the secondary efficiency remains low at about 27.91%, indicating inefficient power delivery to the load.

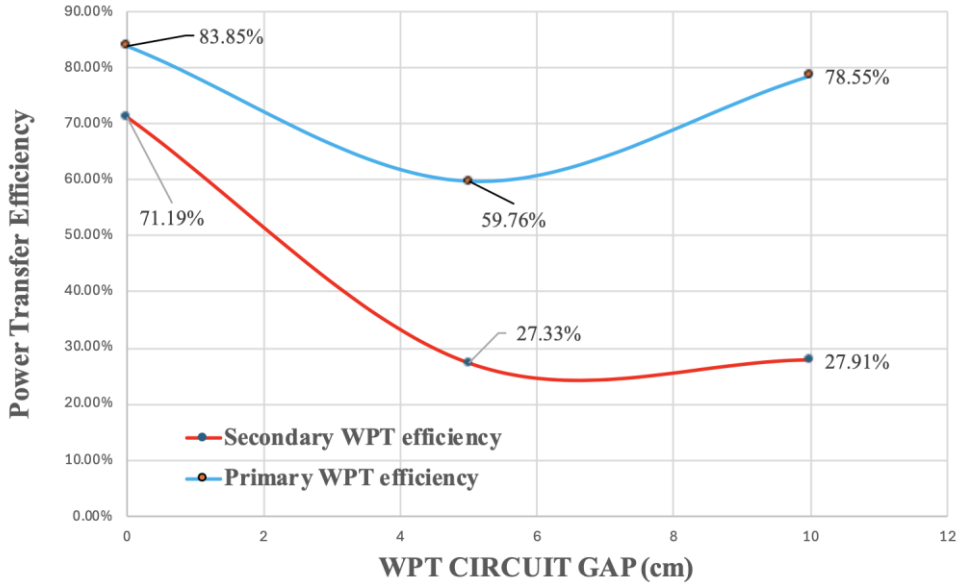

Figure 5.31: WPT system under open-loop operation

Figure 5.32: Secondary WPT system efficiencyillustrates the secondary-side efficiency of the WPT system under both closed-loop and open-loop operating conditions as a function of the circuit gap between the transmitting and receiving coils. The results clearly highlight the impact of the control strategy on the system's capability to maintain efficient power delivery amid varying coupling conditions.

At zero separation, the closed-loop operation attains a secondary efficiency of approximately 84.00%, significantly surpassing the open-loop case, which reaches only 71.19%. This initial disparity suggests that feedback-based control facilitates improved impedance matching and resonance tuning, even under nominal coupling circumstances. As the circuit gap increases to 5 cm, both configurations experience a marked decline in efficiency due to reduced magnetic coupling. However, the drop is considerably less pronounced in the closed-loop system, which retains an efficiency of 55.20%, compared to just 27.33% in open-loop operation. This represents nearly a twofold enhancement, underscoring the robustness of the closed-loop approach.

At a larger gap of 10 cm, the closed-loop efficiency further decreases to 30.49%, while the open-loop efficiency remains relatively unchanged at 27.91%. This indicates that the open-loop system reaches a saturation point, beyond which further increases in gap yield minimal performance variation. Overall, the figure confirms that closed-loop control substantially improves secondary-side efficiency across the entire range of circuit gaps, especially under moderate misalignment. These findings underscore the importance of adaptive feedback mechanisms in WPT systems for addressing coupling variations and ensuring reliable, efficient power transfer.

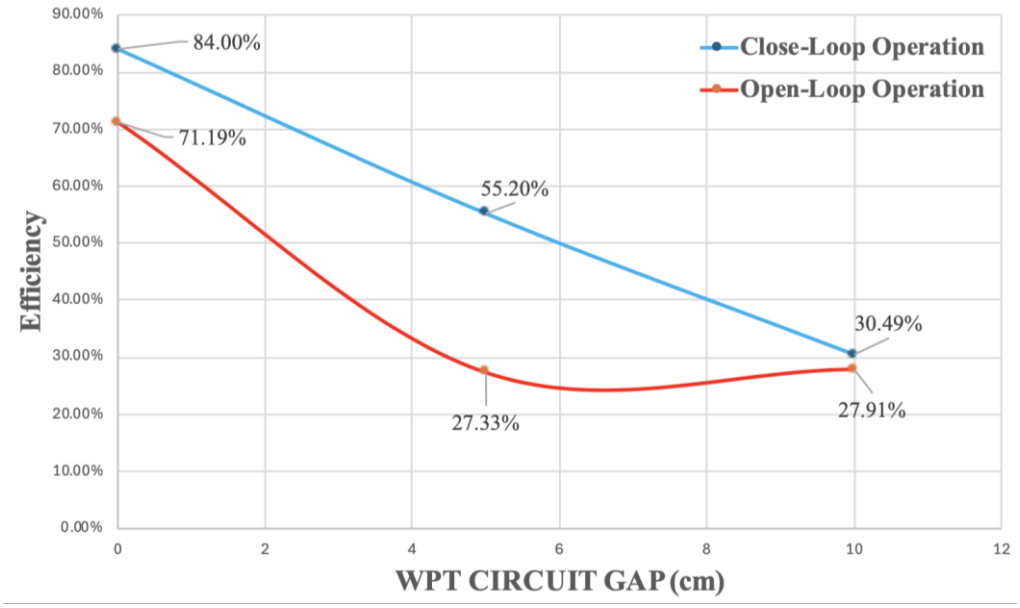

Figure 5.32: Secondary WPT system efficiency

Figure 5.33 illustrates how primary-side efficiency in the WPT system varies as a function of circuit gap under both closed-loop and open-loop operating conditions. The results underscore the significant impact of feedback control on maintaining efficient operation amid coupling variations.

At a zero circuit gap, the closed-loop configuration achieves a high primary efficiency of 94.07%, surpassing the 83.85% obtained in the open-loop scenario. This difference highlights the closed-loop strategy's capability to effectively regulate the operating point, ensuring optimal resonance and minimizing losses at the transmitter side. As the circuit gap increases to 5 cm, efficiency declines in both cases due to weakened magnetic coupling. Nevertheless, the closed-loop system achieves a higher efficiency (67.75%) than the open-loop case (59.76%), demonstrating greater robustness to misalignment.

At a larger separation of 10 cm, divergent trends become evident. The open-loop efficiency rises to 78.55% due to a favorable resonance or impedance condition at the primary side, whereas the closed-loop efficiency remains relatively stable at 68.14%. Despite this partial recovery in the open-loop case, the closed-loop operation consistently exhibits a more uniform efficiency profile across the entire range of circuit gaps, avoiding significant performance fluctuations.

Overall, the analysis indicates that closed-loop control enhances the stability and predictability of primary-side efficiency in WPT systems, especially under conditions of moderate coupling degradation. These findings emphasize the benefits of feedback-based strategies in ensuring reliable transmitter-side performance across varying operating conditions.

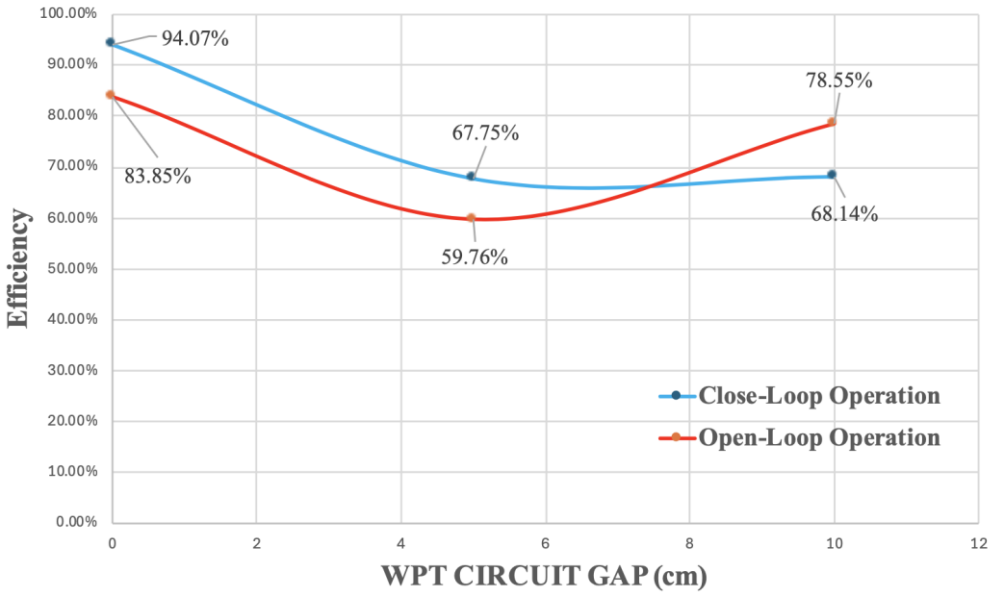

Figure 5.33: Primary WPT system efficiency

5.12 Final Considerations

This chapter outlines the development and implementation of each construction stage of the WPT system, which features a class DE inverter with resonant LLC load. It encompasses various aspects, from selecting semiconductor components to the intricate details of building inductors and designing boards. Special criteria were adopted to ensure compliance with the manufacturer's recommendations for optimal operation at high frequencies.

A detailed overview of the methodology employed to implement the ADALINE-based ARX neural network controller within the ESP32 microcontroller has been provided. This includes a concise discussion of the parameters that influence the data used for decision-making, ultimately determining the duty cycle for the PWM output. This output is crucial, as it provides the controlled output of the proposed system based on current and voltage samples from the inductor in the primary circuit of the WPT.

A brief description of the topology used for the peripheral circuits in the controller is outlined, covering the zero-crossing detector, amplification stages, signal filtering stages, and adaptation to the microcontroller's operating voltage range.

The validation of the Class DE inverter circuit with an LLC series resonant load controlled by an ADALINE-based ARX model is summarized. To achieve this, the previously developed mathematical expressions were verified against data from the constructed prototype, and the voltage and current waveforms were thoroughly validated on both the primary and secondary sides of the WPT system.

The analysis of the results confirms that the proposed control model yields superior power transfer efficiency to the load. Furthermore, it demonstrates that the proposed mathematical

models accurately capture the behavior of the Class DE resonant inverter and its control strategy, driven by an ARX neural network. Consequently, it is reasonable to conclude that this proposed strategy is instrumental in designing control methodologies for resonant inverters that enhance system efficiency without increasing design complexity.

FINAL CONCLUSION

This work presents findings on the performance of a control strategy that uses the ADALINE neural network, applied to an autoregressive prediction model with exogenous inputs. The goal is to ensure the optimal operation of a Class DE half-bridge inverter with an LLC series resonant load within a WPT system. While numerous important aspects have been discussed throughout the study, it remains essential to provide an overview of the main contributions and propose avenues for future exploration.

In the existing literature, various approaches to contactless energy transfer are identified and categorized by converter type and transmission method. These include IPT, which allows for limited transfer distances; RIPT, which strikes a balance between distance and transmitted power; PMPT, which can lead to temperature spikes when foreign objects are present; CWPT, which necessitates a more complex design; OWPT, which is sensitive to environmental conditions; MR-WPT, characterized by low efficiency and high levels of electromagnetic exposure; and UTET, which tends to be inefficient and expensive.

This analysis of resonant circuits is based on a methodology first applied to the series-resonant circuit. This methodology was later extended to parallel and series-parallel topologies, although it required greater mathematical skill for both cases, especially for the series-parallel resonant system. In fact, the use of MATHCAD® software was necessary to obtain the representative equations of the system in this case. This study established that the characteristic of a series circuit is identical to that of a buck converter, which essentially acts as a voltage reducer. On the other hand, the parallel circuit is associated with a boost converter, which increases the voltage. The series-parallel circuit, meanwhile, can be modeled as a Buck-boost converter with a wide range of load resistances. This allows greater immunity to misalignment of the magnetic circuit, which is directly related to the resistor's ohmic value. Overall, this study highlights the importance of understanding the different resonant circuit topologies and their respective characteristics. By doing so, one could better design and optimize these circuits for various applications.

The topology of the Class DE resonant inverter is presented as the optimal choice due to its soft-switching characteristics, high efficiency, and minimal component count. A transfer function relating the load voltage to the duty cycle of the inverter switches has been proposed and validated using simulation tools, subsequently being integrated into an autoregressive neural network with an external input (ADALINE-based ARX Controller). At last, the series LLC, parallel LLC, and series-parallel resonant topologies have been evaluated, with the series topology being selected. However, the challenge of scaling the proposed control for the other resonant topologies remains unaddressed.

Based on the simulation results, a Class DE inverter prototype with LLC series resonant load, controlled by an ADALINE-based ARX, has been built to validate the theoretical principles. Various design considerations were necessary, including soft-switching characteristics, high-frequency board-level plan strategies, microcontroller-based digital control implementation, filtering and amplification stages, and impedance-coupling techniques. These aspects were essential to ensure the proper operation of the constructed prototype.

The features, such as efficiency, transmission distance, harmonic content, and immunity to magnetic-circuit misalignments, have been addressed through physical implementation. The time-domain waveforms provide insights into the system's efficiency and help validate the controller's performance across different transmission distances. Additionally, frequency-domain analysis is employed to determine the required parameters in accordance with the IEEE standards governing WPT systems. Furthermore, thermal performance analysis of semiconductor components has been used to assess the stress on the switches in the resonant inverter.

The efficiency of the WPT system was evaluated, revealing that under optimal conditions, specifically, without any separation in the magnetic circuit geometry, a remarkable energy transmission efficiency of 84.00% was achieved. The ADALINE-based ARX control system further improved the efficiency. In contrast, when the controller was disabled, this performance notably declined to 71.19%. Introducing a 5 cm separation within the magnetic circuit decreased efficiency from 55.20% with the controller active to 27.33% in open-loop mode. Similarly, at a separation of 10 cm, efficiency dropped from 30.49% to 27.91%, respectively. Spectral analysis confirmed the system's operation under resonance conditions, ensuring maximum energy transfer across the scenarios examined. This consistently highlights the significance of analyzing the power vectors for each case under study.

For prospective future endeavors, it is recommended to undertake a thorough analysis of the secondary-side WPT system. This should encompass the creation of a resonant rectifier paired with an advanced battery charge control system. Additionally, exploring both parallel and series-parallel resonant circuit topologies presents a promising avenue for further investigation.

REFERENCES

[1] Y. Zheng, Y. Wang, and Q. Yang, "Two-phase operation for coordinated charging of electric vehicles in a market environment: From electric vehicle aggregators' perspective," *Renewable and Sustainable Energy Reviews,* vol. 171, p. 113006, 2023.

[2] S. Gössling, "Integrating e-scooters in urban transportation: Problems, policies, and the prospect of system change," *Transportation Research Part D: Transport and Environment,* vol. 79, p. 102230, 2020.

[3] T. R. Alsenani, "The participation of electric vehicles in a peer-to-peer energy-backed token market," *International Journal of Electrical Power & Energy Systems,* vol. 148, p. 109005, 2023.

[4] R. T. Yadlapalli, A. Kotapati, R. Kandipati, and C. S. Koritala, "A review on energy efficient technologies for electric vehicle applications," *Journal of Energy Storage,* vol. 50, p. 104212, 2022.

[5] E. M. Bibra *et al.*, "Global EV Outlook 2021: Accelerating ambitions despite the pandemic," 2021.

[6] P. Franzese *et al.*, "Fast DC charging infrastructures for electric vehicles: overview of technologies, standards, and challenges," *IEEE Transactions on Transportation Electrification,* vol. 9, no. 3, pp. 3780-3800, 2023.

[7] H. Tu, H. Feng, S. Srdic, and S. Lukic, "Extreme fast charging of electric vehicles: a technology overview," *IEEE Transactions on Transportation Electrification,* vol. 5, no. 4, pp. 861-878, 2019.

[8] V. B. Vu, J. M. González-González, V. Pickert, M. Dahidah, and A. Triviño, "A hybrid charger of conductive and inductive modes for electric vehicles," *IEEE Transactions on Industrial Electronics,* vol. 68, no. 12, pp. 12021-12033, 2021.

[9] J. Yusuf, A. S. M. J. Hasan, J. Garrido, S. Ula, and M. J. Barth, "A comparative techno-economic assessment of bidirectional heavy duty and light duty plug-in electric vehicles operation: a case study," *Sustainable Cities and Society,* vol. 95, p. 104582, 2023.

[10] S. R. Salkuti, "Advanced technologies for energy storage and electric vehicles," *Energies,* vol. 16, no. 5, p. 2312, 2023.

[11] S. S. G. Acharige, M. E. Haque, M. T. Arif, N. Hosseinzadeh, K. N. Hasan, and A. M. T. Oo, "Review of electric vehicle charging technologies, standards, architectures, and converter configurations," *IEEE Access,* vol. 11, pp. 41218-41255, 2023.

[12] R. P. Narasipuram and S. Mopidevi, "A technological overview & design considerations for developing electric vehicle charging stations," *Journal of Energy Storage,* vol. 43, p. 103225, 2021.

[13] A. Ahmad, S. M. Alam, and R. Chabaan, "A Comprehensive Review of Wireless Charging Technologies for Electric Vehicles," *IEEE Transactions on Transportation Electrification,* vol. 4, no. 1, pp. 38-63, 2018.

[14] K. S. Kapse, "Wireless power transfer (WPT) for electric vehicle (EV) battery charging by magnetic resonance coupling (MRC)," *JournalNX,* vol. 2, no. 5, pp. 1-4.

[15] T. Khemkhaeng, S. Nutwong, E. Mujjalinvimut, S. Maiket, and N. Wiraphonsawan, "Design of a current source half-bridge inverter used in WPT system," in *2022 19th International conference on electrical engineering/electronics, computer, telecommunications and information technology (ECTI-CON)*, 24-27 May 2022 2022, pp. 1-5.

[16] S. Niu, H. Xu, Z. Sun, Z. Y. Shao, and L. Jian, "The state-of-the-arts of wireless electric vehicle charging via magnetic resonance: principles, standards and core technologies," *Renewable and Sustainable Energy Reviews,* vol. 114, p. 109302, 2019.

[17] L. Shi, J. Rodriguez, M. J. Carrizosa, and P. Alou, "ZVS tank optimization for class-D amplifiers in high frequency WPT applications," in *2021 IEEE Applied Power Electronics Conference and Exposition (APEC)*, 2021: IEEE, pp. 1593-1598.

[18] K. Song *et al.*, "A review on interoperability of wireless charging systems for electric vehicles," *Energies,* vol. 16, no. 4, p. 1653, 2023.

[19] M. Abou Houran, X. Yang, and W. Chen, "Magnetically coupled resonance WPT: Review of compensation topologies, resonator structures with misalignment, and EMI diagnostics," *Electronics,* vol. 7, no. 11, p. 296, 2018.

[20] Z. Wang, Y. Sun, R. Yang, and M. Zhang, "Frequency splitting characteristics analysis of capacitive wireless power transfer," *Electrical Engineering,* vol. 105, no. 2, pp. 1299-1305, 2023.

[21] V. Z. Barsari, D. J. Thrimawithana, S. Kim, and G. A. Covic, "Modular coupler with integrated planar transformer for wireless EV charging," *IEEE Transactions on Power Electronics,* vol. 38, no. 7, pp. 9206-9217, 2023.

[22] K. W. Klontz, A. Esser, R. R. Bacon, D. M. Divan, D. W. Novotny, and R. D. Lorenz, "An electric vehicle charging system with'universal'inductive interface," in *Power Conversion Conference*: IEEE, pp. 227-232.

[23] R. Pulletikurthi and D. Ronanki, "Review and comparison of modulation schemes for inductive power transfer systems," in *2024 IEEE International Conference on Power Electronics, Drives and Energy Systems (PEDES)*, 2024, pp. 1-6.

[24] I. G. Sîrbu, L. Mandache, D. G. Stănescu, and M. E. Ardeleanu, "Series-series versus series-parallel in terms of stability issues for inductive power transfer systems," in *2024 IEEE International Conference on Environment and Electrical Engineering and 2024 IEEE Industrial and Commercial Power Systems Europe (EEEIC / I&CPS Europe)*, 2024, pp. 1-6.

[25] D. a. Wang *et al.*, "Modern advances in magnetic materials of wireless power transfer systems: A review and new perspectives," *Nanomaterials,* vol. 12, no. 20, p. 3662, 2022.

[26] D. S. Yeole, A. J. Anil, C. P. Pandit, and G. V. Vinayak, "Analysis of Compensation Network in Resonant Inductive Power Transfer (RIPT) for Electric Vehicle Charging," in *2025 5th International Conference on Trends in Material Science and Inventive Materials (ICTMIM)*, 2025, pp. 134-137.

[27] A. Munsi, S. Pradhan, and K. Aditya, "A simplified primary side control strategy for resonant inductive power transfer systems," in *2024 IEEE International Conference on Power Electronics, Drives and Energy Systems (PEDES)*, 2024, pp. 1-6.

[28] W. Li, "High efficiency wireless power transmission at low frequency using permanent magnet coupling," Text, 2009. [Online].

[29] H. Kim, J. Ahn, S. Woo, S. Huh, and S. Ahn, "Alignment of wireless power transfer system for implantable medical device using permanent magnet," in *2023 IEEE Wireless Power Technology Conference and Expo (WPTCE)*, 2023, pp. 1-4.

[30] C.-K. Chang, G. G. Da Silva, A. Kumar, S. Pervaiz, and K. K. Afridi, "30 W capacitive wireless power transfer system with 5.8 pF coupling capacitance," in *International Conference on Electrical Engineering/Electronics, Computer, Telecommunications and Information Technology (ECTI-CON*, 2015: IEEE, pp. 1-4.

[31] P. S, K. N. G, and S. S. A, "Charging up the future: capacitive and inductive wireless power transfer," in *2024 International Conference on E-mobility, Power Control and Smart Systems (ICEMPS)*, 2024, pp. 1-6.

[32] D. E. Raible, "High intensity laser power beaming for wireless power transmission," Master degree, Cleveland State University, Ohio, 2008. [Online].

[33] R. K. Kottilingal and N. Nambath, "Underwater optical wireless data and power transfer system for internet of underwater things," in *2025 IEEE International Symposium on Circuits and Systems (ISCAS)*, 2025, pp. 1-5.

[34] S. T. Khang, D. J. Lee, I. J. Hwang, T. D. Yeo, and J. W. Yu, "Microwave power transfer with optimal number of rectenna arrays for midrange applications," *IEEE Antennas and Wireless Propagation Letters,* vol. 17, no. 1, pp. 155-159, 2018.

[35] W. Lan, P. Shen, L. Jiang, and H. Chen, "Research on maximum power load of wireless power transfer via magnetic resonance coupling," in *2025 3rd International Conference on Power, Grid and Energy Storage*, 2025, pp. 387-390.

[36] B. Zhan, "Experimental analysis of magnetically coupled resonant wireless energy transfer system," in *2025 26th International Conference on Electronic Packaging Technology (ICEPT)*, 2025, pp. 1-5.

[37] O. Shaul, S. Boaz, and S. Doron, "Non-invasive sensing of the electrical energy harvested by medical implants powered by an ultrasonic transcutaneous energy transfer link," in *2012 IEEE International Symposium on Industrial Electronics*, ed, 2012, pp. 1153-1157.

[38] J. Lu, G. Zhu, and C. C. Mi, "Foreign object detection in wireless power transfer systems," *IEEE Transactions on Industry Applications,* vol. 58, no. 1, pp. 1340-1354, 2022.

[39] X. Zixuan, "A wireless power transfer system based on high quality factor inductor," in *Proc.SPIE*, 2022, vol. 12294, p. 122941E.

[40] J. C. Lin, "Safety of wireless power transfer," *IEEE Access,* vol. 9, pp. 125342-125347, 2021.

[41] I. C. o. N.-I. R. P. (ICNIRP), "Guidelines for limiting exposure to electromagnetic fields (100 kHz to 300 GHz)," *Health Physics,* vol. 118, no. 5, pp. 483-524, 2020.

[42] M. Mohammad, O. C. Onar, J. L. Pries, V. P. Galigekere, G. J. Su, and J. Wilkins, "Thermal analysis of a 50 kW three-phase wireless charging system," in *2021 IEEE Transportation Electrification Conference & Expo (ITEC)*, 2021, pp. 1-6.

[43] B. A. Rayan, U. Subramaniam, and S. Balamurugan, "Wireless power transfer in electric vehicles: a review on compensation topologies, coil structures, and safety aspects," *Energies,* vol. 16, no. 7, p. 3084, 2023.

[44] M. Ghalkhani and S. Habibi, "Review of the Li-ion battery, thermal management, and AI-based battery management system for ev application," *Energies,* vol. 16, no. 1, p. 185, 2023.

[45] Y. Cao *et al.*, "A holistic review on e-mobility service optimization: challenges, recent progress and future directions," *IEEE Transactions on Transportation Electrification,* pp. 1-1, 2023.

[46] J. Ma, Z. Li, Y. Liu, M. Ban, and W. Song, "Thermal analysis and optimization of the magnetic coupler for wireless charging system," *IEEE Transactions on Power Electronics,* vol. 38, no. 12, pp. 16269-16280, 2023.

[47] SAE International. "J2954_202408 - Wireless Power Transfer for Light-Duty Plug-in/Electric Vehicles and Alignment Methodology." accessed: November, 2023, [Online].

Available: https://www.sae.org/standards/j2954_202408-wireless-power-transfer-light-duty-plug-electric-vehicles-alignment-methodology.

[48] Z. Zheng, N. Wang, and S. Ahmed, "Adaptive frequency tracking control with fuzzy PI compound controller for magnetically coupled resonant wireless power transfer," *International Journal of Fuzzy Systems,* vol. 23, pp. 1890-1903, 2021.

[49] R. R. Kumar, C. Bharatiraja, K. Udhayakumar, S. Devakirubakaran, K. S. Sekar, and L. Mihet-Popa, "Advances in Batteries, Battery Modeling, Battery Management System, Battery Thermal Management, SOC, SOH, and Charge/Discharge Characteristics in EV Applications," *IEEE Access,* vol. 11, pp. 105761-105809, 2023.

[50] F. Sun and R. Xiong, "A novel dual-scale cell state-of-charge estimation approach for series-connected battery pack used in electric vehicles," *Journal of Power Sources,* vol. 274, pp. 582-594, 2015/01/15/ 2015.

[51] M. A. Yousuf, T. K. Das, M. E. Khallil, N. A. A. Aziz, M. J. Rana, and S. Hossain, "Comparison study of inductive coupling and magnetic resonant coupling method for wireless power transmission of electric vehicles," in *2021 2nd International Conference on Robotics, Electrical and Signal Processing Techniques (ICREST)*, 5-7 Jan. 2021 2021, pp. 737-741.

[52] S. Wang, X. Sun, W. Feng, X. Ma, Y. Jing, and S. Li, "Optimization of magnetic coupling resonance coils," in *2021 IEEE 16th Conference on Industrial Electronics and Applications (ICIEA)*, 2021: IEEE, pp. 793-796.

[53] S. Nie, W. Han, Z. Luo, C. Perera, and P. W. Lehn, "Sequential mutual-inductance identification method for wireless power transfer systems of electric vehicles," *IEEE Transactions on Transportation Electrification,* pp. 1-1, 2023.

[54] A. Ali *et al.*, "Analysis of symmetric two and four-coil magnetic resonant coupling wireless power transfer," *Applied Computational Electromagnetics Society Journal,* 2022.

[55] Y. Pei, Y. Le Bihan, M. Bensetti, and L. Pichon, "Comparison of coupling coils for static inductive power-transfer systems taking into account sources of uncertainty," *Sustainability,* vol. 13, no. 11, p. 6324, 2021.

[56] G. Sun, Y. Yang, J. Zhang, Y. Cao, X. Tan, and J. Pei, "Modeling and optimization of pavement scale-model for magnetically coupled resonant in wireless power transmission systems," *Construction and Building Materials,* vol. 319, p. 126066, 2022.

[57] C. Wang and J. Wang, "A hybrid lCC-SP compensation network with adjustable impedance angle used for single-stage wireless power transfer," *IEEE Transactions on Transportation Electrification,* vol. 9, no. 2, pp. 3452-3463, 2023.

[58] C. Ma, X. Qu, Y. Li, and J. Liu, "Single-stage active rectifier with wide impedance conversion ratio range for inductive power transfer system delivering constant power," *IEEE Transactions on Power Electronics,* vol. 38, no. 6, pp. 7877-7890, 2023.

[59] A. Razek, "Review of contactless energy transfer concept applied to inductive power transfer systems in electric vehicles," *Applied Sciences,* vol. 11, no. 7, p. 3221, 2021.

[60] M. Kim and J. Choi, "High-frequency, mid-range wireless power transfer system using critical coupling coefficient adjustment," in *2021 IEEE Applied Power Electronics Conference and Exposition (APEC)*, 2021: IEEE, pp. 714-719.

[61] K. Shi, T. Feng, J. Jiang, P. Wang, Z. Meng, and C. Tang, "A highly magnetic integrated method of lcc-compensated ipt system with excellent misalignment tolerance," *IEEE Transactions on Power Electronics,* vol. 38, no. 12, pp. 16256-16268, 2023.

[62] Z. Yuan *et al.*, "A power-enhancing complementary coupling integration strategy for misalignment-tolerant wpt systems," *IEEE Transactions on Power Electronics,* vol. 38, no. 11, pp. 14689-14701, 2023.

[63] H. Li, Z. Liu, B. PanLiu, J. Wang, M. Liu, and Y. Wang, "A wireless power transfer system with high misalignment tolerance and low component count," *IEEE Transactions on Power Electronics,* pp. 1-12, 2023.

[64] T. S. Pham *et al.*, "Optimal frequency for magnetic resonant wireless power transfer in conducting medium," *Scientific Reports,* vol. 11, no. 1, p. 18690, 2021.

[65] E. Shehata, "Design of high efficiency low frequency wireless power transfer system for electric vehicle charging," *Electrical Engineering,* vol. 104, no. 3, pp. 1797-1809, 2022.

[66] X. Wang *et al.*, "Synthesis and analysis of primary high-order compensation topologies for wireless charging system applying sub-harmonic control," *IEEE Transactions on Power Electronics,* vol. 38, no. 7, pp. 9173-9182, 2023.

[67] M. Kiyani, S. E. Abdollahi, S. R. Abdollahi, and B. Baigzadehnoe, "Investigation of resonant tank topologies performance in wireless power transfer applications," *International Journal of Electronics,* no. just-accepted, 2023.

[68] E. Gomaa, A. Shawky, and M. Orabi, "Wireless charging techniques and converter topologies for light EVs, e-bikes, e-chairs and escooters: a review," in *2023 IEEE Conference on power electronics and renewable energy (CPERE)*, 2023: IEEE, pp. 1-8.

[69] K. Thiagarajan and T. Deepa, "A comprehensive review of high-frequency transmission inverters for magnetic resonance inductive wireless charging applications in electric vehicles," *IETE Journal of Research,* pp. 1-11, 2021.

[70] S. R. Meher and R. K. Singh, "Single-phase wireless electric vehicle charger using ef2 inverter," *International Transactions on Electrical Energy Systems,* vol. 2023, p. 6038394, 2023.

[71] M. K. Kazimierczuk, F. Corti, G. M. Lozito, and A. Reatti, "Power quality in class-D high-frequency power inverter: input and resonant tank distortion power, total harmonic distortion, and power factor," *IEEE Transactions on Circuits and Systems I: Regular Papers,* vol. 72, no. 5, pp. 2419-2431, 2025.

[72] T. Kondo and H. Koizumi, "Class DE voltage-source parallel resonant inverter," in *IECON 2015 - 41st Annual Conference of the IEEE Industrial Electronics Society*, 2015, pp. 002968-002973.

[73] Z. Pengyu, L. Junfeng, M. Mingze, F. Zijie, Z. Hao, and Z. Jun, "Review on single-phase high-frequency resonant inverters for current sharing in multiple inverter system," *International Journal of Circuit Theory and Applications,* vol. n/a, no. n/a, 2023.

[74] Y. Zhang, Z. Shen, X. Li, S. Chen, and Y. Tang, "Passive current sharing of a multiphase inverter based on parallel resonance," *IEEE Transactions on Industrial Electronics,* vol. 69, no. 9, pp. 8625-8632, 2022.

[75] M. Yamaguchi, K. Kusaka, and J. i. Itoh, "Mega-hertz High-power WPT system with Parallel-connected inverters using current balance circuit," in *2022 24th European Conference on Power Electronics and Applications (EPE'22 ECCE Europe)*, 2022, pp. 1-9.

[76] X. Liu *et al.*, "A multi-inverter multi-rectifier wireless power transfer system for charging stations with power loss optimized control," *IEEE Transactions on Power Electronics,* vol. 38, no. 8, pp. 9261-9277, 2023.

[77] L. Yang, X. Li, S. Liu, Z. Xu, and C. Cai, "Analysis and Design of an LCCC/S-Compensated WPT System With Constant Output Characteristics for Battery Charging

Applications," *IEEE Journal of Emerging and Selected Topics in Power Electronics,* vol. 9, no. 1, pp. 1169-1180, 2021.

[78] T. Sriprom *et al.*, "Variable frequency control for constant current constant voltage inductive wireless ev charging system," in *2022 International Power Electronics Conference (IPEC-Himeji 2022- ECCE Asia)*, 2022, pp. 1481-1488.

[79] L. Yang, Y. Shi, M. Wang, and L. Ren, "Constant voltage charging and maximum efficiency tracking for WPT systems employing dual-side control scheme," *IEEE Journal of Emerging and Selected Topics in Power Electronics,* vol. 10, no. 1, pp. 945-955, 2022.

[80] Y. Liu *et al.*, "Frequency tracking control of the WPT system based on fuzzy RBF neural network," *International Journal of Intelligent Systems,* vol. 37, no. 7, pp. 3881-3899, 2022.

[81] S. Jaman, S. Chakraborty, M. El Baghdadi, T. Geury, and O. Hegazy, "Small-signal average switch modeling and dual-loop control of bidirectional integrated converter for G2V and V2G applications in battery EVs," in *2021 23rd European Conference on Power Electronics and Applications (EPE'21 ECCE Europe)*, 2021: IEEE, pp. 1-12.

[82] C. Xia, N. Wei, H. Zhang, S. Zhao, Z. Li, and Z. Liao, "Multifrequency and multiload MCR-WPT system using hybrid modulation waves SPWM control method," *IEEE Transactions on Power Electronics,* vol. 36, no. 11, pp. 12400-12412, 2021.

[83] J. Zhao and C. Wu, "Research on control method and variable topology design of wireless power transmission system with coil offset," *IEEJ Transactions on Electrical and Electronic Engineering,* vol. 17, no. 10, pp. 1495-1505, 2022.

[84] Y. Jiang, L. Wang, J. Fang, R. Li, R. Han, and Y. Wang, "A high-efficiency zvs wireless power transfer system for electric vehicle charging withvariable angle phase shift control," *IEEE Journal of Emerging and Selected Topics in Power Electronics,* vol. 9, no. 2, pp. 2356-2372, 2021.

[85] M. Zhou, F. Liu, S. Li, and X. Chen, "A 1-kW and 100-cm distance magnetically coupled resonant WPT system achieving 80% efficiency," *IEEE Transactions on Transportation Electrification,* vol. 8, no. 3, pp. 4001-4013, 2022.

[86] Z. Yuan, P. Fu, G. Lu, and P. Cao, "Wireless power transfer system based on frequency and impedance matching hybrid adjustment against system detuning," *Journal of Physics: Conference Series,* vol. 2108, no. 1, p. 012035, 2021.

[87] W. Lu, J. Zhao, X. Chen, Q. Fan, and C. Zhang, "Bilateral control strategy based on LCL-S compensation network wireless charging system without communication," *International Journal of Automotive Technology,* vol. 24, no. 1, pp. 171-178, 2023.

[88] S.-Y. R. Hui, Y. Yang, and C. Zhang, "Wireless power transfer: a paradigm shift for the next generation," *IEEE Journal of Emerging and Selected Topics in Power Electronics,* 2023.

[89] Z. Tong, Z. Ye, and J. Rivas-Davila, "Class DE switch-mode power amplifier using GaN power HEMTs," *IEEE Microwave Magazine,* vol. 23, no. 3, pp. 72-79, 2022.

[90] H. Koizumi, M. Fujii, T. Suetsugu, and S. Mori, "New resonant dc/dc converter with class DE inverter and class E rectifier," *Journal of Circuits, Systems, and Computers,* vol. 5, no. 04, pp. 559-574, 1995.

[91] C. Jiang, K. T. Chau, C. Liu, and C. H. T. Lee, "An overview of resonant circuits for wireless power transfer," *Energies*, vol. 10, no. 7*,*

[92] K. Seeliger, L. Ambrogioni, Y. Güçlütürk, L. M. van den Bulk, U. Güçlü, and M. A. van Gerven, "End-to-end neural system identification with neural information flow," *PLOS Computational Biology,* vol. 17, no. 2, p. e1008558, 2021.

[93] A. Géron, *Hands-on machine learning with Scikit-Learn, Keras, and TensorFlow*. " O'Reilly Media, Inc.", 2022.

[94] L. Pamungkas, M. Tampubolon, Q. Lin, and H. J. Chiu, "Performance comparison of primary side PFM and secondary side PWM for SS wireless power transfer CC/CV control strategy," in *2018 IEEE International Power Electronics and Application Conference and Exposition (PEAC)*, 2018, pp. 1-5.

[95] U. D. Kavimandan, V. P. Galigekere, O. Onar, B. Ozpineci, and S. M. Mahajan, "Comparison of Dead-Time Effects in a WPT System Inverter for Different Fixed-Frequency Modulation Techniques," in *2020 IEEE Transportation Electrification Conference & Expo (ITEC)*, 2020, pp. 277-283.

[96] J. Li, D. Xu, and D. Wang, "Perturb and observe method of impedance matching for magnetically coupled wireless power transfer system," in *2018 Chinese Automation Congress (CAC)*, 2018, pp. 2513-2517.

[97] M. K. Kazimierczuk and D. Czarkowski, *Resonant power converters*. John Wiley & Sons, 2012.

[98] L. Shi, J. C. Rodriguezt, and P. Alou, "Modeling and analysis of total harmonic distortion in series-series wireless power transfer system for 6.78 MHz," in *2020 IEEE Energy Conversion Congress and Exposition (ECCE)*, 2020, pp. 1016-1020.

[99] J. Millan, P. Godignon, X. Perpiñà, A. Pérez-Tomás, and J. Rebollo, "A survey of wide bandgap power semiconductor devices," *IEEE transactions on Power Electronics,* vol. 29, no. 5, pp. 2155-2163, 2013.

[100] M. R. Razali, J. Jamaludin, A. S. Abu Bakar, F. Ismail, R. Za'im, and Krismadinata, "A Review of Emerging Trends of GaN Power Semiconductor Applications in Onboard Chargers," *Journal of Circuits, Systems and Computers,* 2025.

[101] M. Frivaldsky, J. Morgos, and R. Zelnik, "Evaluation of GaN power transistor switching performance on characteristics of bidirectional DC-DC converter," *Elektronika ir elektrotechnika,* vol. 26, no. 4, pp. 18-24, 2020.

[102] K. e. corporation, "FPL100/100/6-BH1T ferrite plate for wireless power transfer – product specification," KEMET electronics corporation, Fort Lauderdale, FL, USA, 2023.

[103] O. Semiconductor, "High speed half-bridge driver for GaN power switches," *NCP51820,* 2019.

[104] F. James, *Operational amplifiers & linear integrated circuits: theory and application*. dissidents, 2018.

[105] Z. Dzwigalski and Z. Zimek, "Safety cut-out and trigger circuits of the TH2158 klystron modulator," 2008.

[106] I. Texas, "LM118/LM218/LM318 Operational amplifiers datasheet," Texas Instruments Incorporated, Dallas, TX, 2016.

[107] L. T. Corporation, "LT119A/LT319A/LM119/LM319 - Dual comparator," Linear Technology Corporation, Milpitas, CA, 1994.

[108] E. Systems, "ESP32 Technical reference manual," Espressif Systems (Shanghai) Co., Ltd., Shanghai, China, 2022.

[109] H. Akaike, "A new look at the statistical model identification," *IEEE Transactions on Automatic Control,* vol. 19, no. 6, pp. 716-723, 1974.

[110] *IEEE Std 1459-2010: IEEE Standard Definitions for the Measurement of Electric Power Quantities Under Sinusoidal, Nonsinusoidal, Balanced, or Unbalanced Conditions*, 978-0-7381-6058-0, E. Institute of Electrical and Electronics, Piscataway, NJ, USA, 2010.

[111] *IEEE Std 1459-2010: Definitions for the measurement of electric power quantities under sinusoidal, nonsinusoidal, balanced, or unbalanced conditions.*, I. Power and E. Society\, New York, USA\Geneva, Switzerland\, 2010.

[112] *IEC 61000-4-30: Electromagnetic compatibility (EMC) - Part 4-30: Testing and measurement techniques - Power quality measurement methods*, I. E. Commission, Geneva, Switzerland, 2015.

[113] M. K. Kazimierczuk, *RF power amplifiers*. John Wiley & Sons, 2014.

[114] R. W. Erickson and D. Maksimovic, *Fundamentals of power electronics*. Springer Science & Business Media, 2007.